

CONTROLLING LIGHT IN NANOSCALE DIMENSIONS

by

Agampodi Madu Nimali Mendis

B.Sc., University of Colombo, 2009

Submitted to the Graduate Faculty of the
Dietrich School of Arts and Sciences in partial fulfillment
of the requirements for the degree of
Doctor of Philosophy

University of Pittsburgh

2016

UNIVERSITY OF PITTSBURGH
DIETRICH SCHOOL OF ARTS AND SCIENCES

This dissertation was presented

by

Agampodi Madu Nimali Mendis

It was defended on

March 29, 2016

and approved by

Dr. Steve Weber, Professor, Department of Chemistry

Dr. Jill Millstone, Assistant Professor, Department of Chemistry

Dr. Linda A. Peteanu, Professor, Department of Chemistry, Carnegie Mellon University

Dissertation Advisor: Dr. David H. Waldeck, Professor, Department of Chemistry

Copyright © by Agampodi Madu Nimali Mendis

2016

CONTROLLING LIGHT IN NANOSCALE DIMENSIONS

Agampodi Madu Nimali Mendis, PhD

University of Pittsburgh, 2016

The study of materials with nanoscale dimensions has gained wide spread research interest as these exhibit novel properties that can be used to manipulation of light for applications ranging from biosensing to optoelectronics. Metallic nanostructures coupled with light exhibit a collective oscillation of conduction band electrons leading an optical feature known as surface plasmon resonance (SPR). Quantum confinement effects in semiconductor nanoparticles allows the control over optical and electronic properties by changing size and shape of the nanoparticle. In order to fully realize the full potential of these interesting properties in nanoscale materials, this dissertation explores on fundamentals of these light matter interactions in nanoscale. The first work in this dissertation investigates on a novel plasmonic array that can be integrated into microfluidic channels to monitor real time biological interactions. The second work explores on coupling between one dimensional chains of plasmonic nanoparticles which leads delocalized surface plasmon feature which is highly sensitive local dielectric changes. The third study uses SPR to detect and quantify the interaction between the HIV capsid proteins and lipid bilayer films with the goal of establishing a potential drug target for HIV infection. The last study investigates on a general strategy to eliminate Fermi level pinning in semiconductor quantum dots using a thin film of alumina which may enhance the photoconversion efficiency in Schottky junction solar cells. The topics covered here should enable an insight into the fundamentals of light matter interactions in nanostructures which may facilitate their applications in sensing and photovoltaics.

TABLE OF CONTENTS

LIST OF EQUATIONS	XXI
ACKNOWLEDGMENTS	XXIV
1.0 INTRODUCTION	1
1.1 Interaction of light with nanoscale metallic structures	2
1.1.1 Surface Plasmon Polaritons	3
1.1.1.1 Nanoslit arrays	8
1.1.2 Localized Surface Plasmon Resonance	10
1.1.2.1 Nanoparticle chains	12
1.1.3 Refractive index sensing using SPR	14
1.1.4 Finite difference time domain calculations	17
1.2 Interaction of light with nanometer scale semiconductor structures	18
1.2.1 Inorganic Semiconductor Nanoparticles	18
1.2.1.1 Quantum Confinement Effects in Semiconductor Quantum Dots . 20	
1.2.1.2 Quantum Dot Solar Cells	22
1.3 Scope of The dissertatnion	27
1.4 References	29
2.0 AN IN-PLANE NANOFIUDIC NANOPLASMONIC-BASED PLATFORM FOR BIODETECTION	33
2.1 Introduction	34
2.2 Experimental	38
2.2.1 Fabrication of Nano-plasmonic Nano-fluidic Device	38

2.2.1.1	Focused Ion Beam Fabrication of the Nanoledge Structures	38
2.2.1.2	Electron Beam Lithography Fabrication of the Nanoledge Structures	39
2.2.2	Finite Difference Time Domain Calculations.....	41
2.2.3	Modeling of Confined Flow-through Nanoslit	43
2.2.4	Measuring the Refractive Index Sensitivity of the Nanoledge Structure .	45
2.2.5	Albumin Binding and Detection using Nanoledge Devices	45
2.2.6	Prostate Specific Antigen (PSA) Binding and Detection using Nanoledge Devices.....	46
2.3	Results and Discussion	46
2.3.1	Focused Ion Beam Fabricated Nanoledge Structures	47
2.3.1.1	Optical Characterization.....	48
2.3.1.2	Refractive Index Sensitivity	49
2.3.1.3	Confined Flow-through Nanoslit.....	54
2.3.1.4	Detecting Albumin-antiAlbumin Interaction using FIB Fabricated Nanoledge Structures	56
2.3.2	Electron Beam Lithography Fabricated Nanoledge Structure	60
2.3.2.1	Detecting Albumin-antiAlbumin Interaction using EBL Fabricated Nanoledge Structures	63
2.4	Conclusions and Future Work	66
2.5	References.....	67
3.0	ENHANCED SENSITIVITY OF DELOCALIZED PLASMONIC NANOSTRUCTURES.....	67

3.1	Introduction.....	71
3.2	Experimental	73
3.2.1	Fabrication of Square NP chains:	73
3.2.2	Sample Characterization	74
3.2.3	Self-assembled Monolayers Formation	75
3.2.4	Finite-difference time-domain (FDTD) simulations.....	75
3.3	Optical Response of Nanoparticle Chains	76
3.3.1	Dependence on Distance between NPs in Chain:.....	76
3.3.2	Dependence on the Number of NPs in the Chain	78
3.3.3	FDTD Simulations of NP Tetramers	82
3.3.4	Tight-Binding Model for NP Chain	83
3.3.5	Distance Dependence of the NP Coupling	85
3.4	Effect of SAM on NP Chain Optical Response	90
3.5	Conclusion	93
3.6	References.....	94
4.0	QUANTIFYING THE INTERACTION OF HIV CAPSID PROTEIN WITH LIPID RAFTS USING SURFACE PLASMON RESONANCE.....	101
4.1	Introduction.....	102
4.1.1	Role and Structure Human Immunodeficiency Virus Capsid Proteins .	102
4.1.2	Lipid Rafts.....	105
4.1.3	BIAcore Surface Plasmon Resonance Instrument	108
4.2	Experimental Methods	109
4.2.1	Substrate Preparation	109

4.2.2	Lipid Solution Preparation	110
4.2.3	Lipid Bilayer Preparation.....	110
4.2.4	In situ Lipid Bilayer Preparation in BIAcore	111
4.2.5	In Situ Lipid Raft Preparation.....	112
4.2.6	The Interaction of Capsid Proteins to SM-CH Raft.....	112
4.2.7	Atomic Force Microscopy Characterization.....	112
4.2.8	Flourescence Recovery after Photobleaching (FRAP)	113
4.3	Results and Discussions.....	114
4.3.1	Lipid Bilayer Preparation.....	114
4.3.2	Lipid Raft Preparation.....	119
4.3.3	Interaction of Full Length Capsid with Lipid Rafts.....	120
4.3.4	Interaction of Capsid Hexamer with Lipid Rafts	120
4.3.5	Interaction of Glycerol Kinase with Lipid Rafts	122
4.3.6	Quantifying the Binding Affinity of CAH to modified Lipid Membranes...	123
4.4	Conclusions and Future work.....	131
4.5	References.....	131
5.0	ELIMINATING FERMI-LEVEL PINNING IN PBS QUANTUM DOTS USING ALUMINA INTERFACIAL LAYER.....	135
5.1	Introduction.....	136
5.1.1	Ligand effects on PbS QD Energetics	138
5.2	Experimental.....	141

5.2.1	Substrate Preparation	141
5.2.2	PbS QD synthesis and characterization.....	142
5.2.3	PbS Thin Film Preparation and Ligand Exchange	143
5.2.4	Atomic Force Microscopy Characterization.....	144
5.2.5	Electrochemical Characterization.....	144
5.2.6	Photoemission Spectroscopy Characterization.....	145
5.3	Results.....	145
5.4	Discussion	152
5.5	Conclusion	154
5.6	References.....	155
6.0	CONCLUDING REMARKS	160
	APPENDIX A	163
	APPENDIX B	169

LIST OF TABLES

Table 3.1 Coupling constant, A of square nanoparticle array samples with ~ 30 nm inter-particle distance indicating its value before and after SAM preparation. Increment in the coupling constant can be seen after SAM preparation.	93
Table 4.1 Immobilized sphingomyelin and cholesterol as a percentage of bilayer lipid composition	119
Table 4.2 Fitted parameters of the data on the Figure 4.9 to Langmuir model	125
Table 4.3 Fitted parameters of the data on the Figure 4.9 to heterogenous ligand model.	130

LIST OF FIGURES

Figure 1.1 This schematic diagram illustrates the electric field contours for SPP propagation along a metal/dielectric interface (x and y directions). The field decays evanescently in the z direction, reflecting the bound and nonradiative nature of SPP. The decay length of the SPP field amplitude is greater towards the dielectric side, as compared to the metal side. This figure is taken from reference [2].²..... 5

Figure 1.2 (a) Plotting equation 1 shows that the momentum (wavevector) of a surface plasmon polariton (solid line) is always greater than that of free-space light (dashed line). This dispersion curve for the SP mode illustrates the momentum mismatch problem, the SP mode always has greater momentum (k_{sp}) than a free space photon (k_0) of the same frequency ω . This diagram is taken from reference [9].⁹ The most commonly used ways to provide missing momentum is by using (b) prism coupling method and, (c) surface corrugation. 7

Figure 1.3 a) SEM image of a Au nanoslit array which was fabricated by the thesis author using electron beam lithography. The scale bar is 2 μm . b) A schematic of a nanoslit array. 9

Figure 1.4 This figure illustrates the excitation of localized surface plasmon resonances in nanoparticles, showing the restoring force induced and the driving force of the EM radiation which causes the charge displacement. This figure is taken from reference [2].²..... 10

Figure 1.5 Linear chain of equidistantly spaced spherical nanoparticles with diameter a and with the distance d between the centers of the particles. The incident plane electromagnetic wave propagates in the z direction. 13

Figure 1.6 Nanoparticle coupling under a longitudinal restoring force (a) shifts the resonance to lower frequency and nanoparticle coupling under a transverse polarization (b) increases the restoring force through coupling to neighbors shifting the resonance to higher frequency..... 14

Figure 1.7 Effective refractive index of a thin film. On the left hand side, the extension of the SPP field in the z direction is entirely within the bulk of the thin film, in that $\delta_d < t_{\text{film}}$. When $\delta_d > t_{\text{film}}$, the effective index seen by the evanescent SPP field, must be calculated as a weighted average of n_{bulk} and $n_{\text{adsorbate}}$ 16

Figure 1.8 Schematic representation of effects of quantum confinement on the density of states moving from (a) bulk to (b) one dimensional quantum confinement in quantum wells, (c) two dimensional quantum confinement in quantum wires, and (c) three dimensional quantum confinement in quantum dots. It can be noted that three dimensional quantum confinement leads atom like delta function is obtained for density of states. This figure is taken from reference 16.¹⁶ 19

Figure 1.9 The graph shows the predicted CBM (red circles) and VBM (black squares) values for PbS QDs that the author calculated by using EMA. The dash lines indicate the bulk CBM and VBM values. For PbS, $E_g^{\text{Bulk}} = 0.41$ eV, $m_{e^*} = 0.4m_0$, $m_{h^*} = 0.33m_0$, and $m_0 = 9.1 \times 10^{-31}$ kg and $\epsilon_r^{\text{PbS}} = 17$ 21

Figure 1.10 Current voltage characteristics of a solar cell under solar illumination 25

Figure 1.11 Schematic representation and working principles of (a) a Schottky junction solar cell, (b) a p-n junction solar cell with heterojunction architecture, and (c) quantum dot sensitized solar cell. Figure is taken from reference 30.³⁰..... 27

Figure 2.1 Two typical SPR configurations..... 35

Figure 2.2 Schematic of FIB milling routine employed for fabricating the nanoledge structure. a) Cleaning the substrates; b) Thin metal film deposition; and c) FIB milling of the targeted nanoledge structure..... 39

Figure 2.3 Schematic of steps followed in fabricating the nanoledge structures using Electron Beam Lithography. a) Step 1 - Fabrication of alignment markers on the substrate b) Step 2 - Fabrication of 50 nm width slits using negative e-beam resist c) Step 3 – Alignment and fabrication of the 250 nm width slit on top of the bottom 50 nm slit to obtain the intended nanoledge structure. 42

Figure 2.4 The yz view of 2-D simulation setup used for the calculations on nanoledge structures. The orange box is defines the simulation area. The pale white area at the bottom represents the quartz substrate whereas the Au film is represented in yellow. The bottom arrow represents the plane light source injecting light along the y direction whereas light is polarized along x direction. 43

Figure 2.5 Physical model of the simulated device 44

Figure 2.6 a) Schematic and b) SEM image of the nanoledge device. 47

Figure 2.7 a) Transmission spectrum of a nanoledge device of a 600 nm periodicity collected in air. Periodicity dependence of the nanoledge devices studied through b) experimentally obtained c) FDTD calculated transmission spectra of the nanoledge devices..... 50

Figure 2.8 The AFM image of the nanoledge structure with a cross along the white line is depicted in (a). In (b) is the FDTD calculated transmission spectra of 600 nm nanoledge structure, with and without the quartz substrate, performed using the slit dimension obtained from (a). Both the spectra were calculated with a background dielectric constant of one. When the quartz substrate is absent it can be noted that peak D disappears from the transmission spectrum 51

Figure 2.9 a) Transmission spectra of the FIB nanoledge structure, periodicity of 600 nm, with different refractive index standards for normally incident TM polarized light. b) Peak A, B, and dip C wavelengths are plotted against the refractive index of the outside medium. Slope of the fitting curve gives the RIU sensitivity of the device to be 545 nm/RIU from dip C and the figure of merit was calculated to be 20.5 per RIU 52

Figure 2.10 The resonance wavelength is plotted against the refractive index of the surrounding environment for different nanoledge periodicity, a) calculated from FDTD method and b) observed for fabricated structures. Panel c) shows how the RI sensitivity of the nanoledge devices depends on the periodicity of the array..... 53

Figure 2.11 Pressure Distribution with the flow rate 0.5 $\mu\text{L}/\text{min}$ 54

Figure 2.12 Correlation of flow rate and pressure drop..... 55

Figure 2.13 Transmission spectra of the nanoledge device a) in air b) after the preparation of mixed monolayer of alkanethiol (COOH/OH) c) when functionalized with anti-BSA d) upon introduction of 1 pg/cm^3 of BSA. All spectra were collected in air. 58

Figure 2.14 Averaged resonance wavelength shift plotted against Albumin concentration measured a) under PBS b) in air. Error bars indicate the standard deviation between resonance shifts in two different trials. $C_{\text{ref}} = 1 \times 10^{-13}$ 59

Figure 2.15 The averaged resonance wavelength shift between two control experiments that were carried out without anti-BSA immobilized on the device show no significant shift with increasing Albumin concentration. Error bars indicate the standard deviation between the two trials. $C_{\text{ref}} = 1 \times 10^{-13}$ 60

Figure 2.16 SEM images of the final structures in each of the three steps used in fabricating nanoledge structure using EBL. (a) Step 1 - Markers were defined on the substrate. (b) Step 2 -

The bottom nanoslit was defined. (c) Step 3 - The top 250 nm slit was aligned on the top of the bottom slit to complete the nanoledge structure. 61

Figure 2.17 Simulated transmission spectra of the nanoledge structure under different offset values (x)..... 62

Figure 2.18 (a) Transmission spectra of the EBL fabricated nanoledge structure, periodicity of 600 nm, with different refractive index standards for normally incident TM polarized light. (b) Peak A, B, and dip C wavelengths are plotted against the refractive index of the outside medium. Slope of the fitting curve gives the RIU sensitivity of the device to be 315 nm/RIU from peak A and the figure of merit was calculated to be 3.3 per RIU 63

Figure 2.19 (a) Transmission spectra of the EBL fabricated nanolege array before any surafce modification in air and after incubating with SAM (air) and the PSA antibody (air) is is depicted. (b) Peak A position is plotted after each surface modification for clarity. 64

Figure 2.20 Peak spectra after incubation with PSA solutions is illustrated in (a) and in (b) is the correlation of the shift in the peak A position to concentrations of PSA in buffer solutions for three arrays of the nanoledge structure. 65

Figure 2.21 Resonance wavelength shift of the Peak A position after incubation with BSA solutions with different concentrations observed for three different arrays of EBL fabricated nanoledge structures..... 66

Figure 3.1 Sketch of optical set-up used during the optical characterization of the samples. The yellow lines indicate the light pathway..... 74

Figure 3.2 a) The transmission spectra of a square nanoparticle tetramer chain are plotted for different inter-particle separations. b) SEM images are shown for five of the square NP tetramer chains in panel A. The scale bar is 400 nm..... 77

Figure 3.3 Panel a) shows the SEM images for square nanoparticle chains (the scale bar is 1000 nm). Panel b) and c) shows the evolution of transmission spectra of those chains under b) longitudinal and c) transverse polarization, collected in air. d) The wavelength maximums of the DSPR are plotted against the NP chain length (see text for details). The error bars in these peak wavelength positions are smaller than size of the symbol e) The DSPR peak area normalized per NP is plotted versus the NP chain length. The red dashed line is given as a guide to eye. 81

Figure 3.4 a) Electric field intensity enhancement (E^2/E_0^2) profiles are shown for a four NP chain with three different nanoparticle separations (d). The direction of the light polarization is parallel to the major axis of the clusters. The scale bar ranges from an amplitude of 0-700. b) The electric field intensity at the x-y center of the cluster is plotted against the inter-particle distance. The red dashed line is given as a guide to eye. 82

Figure 3.5 The resonance energy maximum of the DSPR is plotted versus the number of NPs in the chain under longitudinal (■) and transverse (□) polarization; the red line shows a fit to the data by Equation 1. This analysis is for a 36 nm fixed inter-particle distance. 84

Figure 3.6 (a) The scaled DSPR wavelength shift ratio is plotted versus the scaled gap ratio for different chain lengths of square NP chains. The slope of the best linear fit for each chain length provides the decay constant and these values are plotted in panel (b). 87

Figure 3.7 (a) The resonance energy maximum of the DSPR is plotted versus the number of NPs in the chain under longitudinal polarization for different inter-particle distances, similar to panel 6(a), to obtain a coupling constant A . A plot of the log of the coupling constants versus the log of the center-to-center distances between nanoparticles is shown in (b), and the natural logarithm of the coupling constant ($-A$) versus the center-to-center distance between NPs in the chain is shown in c). Panel (d) shows a plot and analyses for an exponential function. In panel b, c, and d the solid

red line is the best fit to a line, and in panel c the red dashed line indicates the point dipole model.

..... 89

Figure 3.8 Transmission spectra are shown for (a) NPs with large inter-particle separation ($d = 830$ nm) before (black) and after 1-dodecanethiol modifications and (b) for a six NP chain array ($d = 30$ nm) before (black) and after SAM modification (other colors)..... 91

Figure 3.9 The plot of the DSPR peak shift upon SAM adsorption vs. the number of NPs in the chains ($d = 30$ nm). 92

Figure 4.1 a) A Schematic representation of the mature HIV-1 virion, showing the viral glycoprotein envelope (Env, which is made of glycoprotein 120 (gp120) and gp41 subunits), as well as the Gag polypeptide-derived proteins matrix (MA), capsid (CA) and nucleocapsid (NC). The conical viral capsid core is assembled from CA hexamers and pentamers. The capsid core harbours the viral RNA genome, which is associated with NC. b) The conical capsid core assembles into a fullerene cone, containing hexameric (orange) and pentameric (yellow) CA subunits. c) Top view and side view of the hexameric subunits that form the primary capsid core of HIV-1. Interactions between the CA amino-terminal domain (NTD; blue) and the CA carboxy-terminal domain (CTD; red) of adjacent monomers stabilize the assembled hexamer. d) Structure of two CA monomers of a hexamer, illustrating the NTD–CTD pocket, which mediates interactions between CA and host cell proteins. This figure is taken from Reference 1.¹..... 104

Figure 4.2 (a) Glycerophospholipids, which form the L_d phase of the plasma membrane, are roughly cylindrical; however, cholesterol and sphingolipids have a pyramidal or cone-like shape. In sphingolipids the polar head group occupies a larger area than does the hydrophobic region, whereas the converse is true for cholesterol. (b) Given the remarkable fit between the global shape of cholesterol and sphingolipids any void between associated sphingolipids is thought to be filled

by cholesterol functioning as a molecular spacer. The enrichment of cholesterol in L_o phase domains is consistent with this model. This Figure is adapted from reference 16.¹⁶ 106

Figure 4.3 The schematic diagram illustrates the process used for the assembly of DSPC-DPPE mixed lipid bilayer films on Au substrates. (Not drawn to scale). 114

Figure 4.4 Panel (a) plots the measured ellipsometric thickness obtained for DSPC-DPPE mixed lipid bilayer films against the incubation time while changing the DSPC concentration and pH. The closed and open symbols correspond to bilayer formation at pH 7.5 and 7.0, respectively. In panel (b), an AFM image is shown for a lipid bilayer film, obtained while incubating for 1 hr in 0.5 mg/ml DSPC lipid solution at pH 7.0 is shown. The height difference between the scratched window in the image and the surrounding of the image is 6 ± 2 nm. 116

Figure 4.5 Panel a shows the response change during the immobilization of DPPE on a 4-MBA modified gold chip. The net RU change due to immobilization of DPPE is given in the table in the inset. Panel b shows a plot of the SPR thickness change with time for different concentrations of DSPC. Open and closed symbols represent different pH values of the DSPC lipid solution, pH 7.0 and 7.5, respectively..... 117

Figure 4.6 The normalized absorbance (green) and emission (red) spectra of the Rh-B PE is shown in panel (a). In panel (b) solid black squares illustrates the recovery of emission intensity collected by a 575- 625 nm band pass filter after photobleaching. The solid red line is the fit of the equation 4.4 (a) to the collected data. 119

Figure 4.7 The plots corresponds to the response change after FLCA injection onto lipid bilayer films that are modified with (a) 5:2 and (b) 5:3 ratios of SM:CH. 120

Figure 4.8 The response change of CAH binding on SM-CH rafts at different ratios of 5:2 (a) and 5:3 (b) are shown. 121

Figure 4.9 The sensorgrams of glycerol kinase (GK) to SM-CH rafts are shown for different ratios of 5:2 (A) and 5:3 (B) in 20 mM sodium phosphate (pH 7.0), 150 mM KCl. The concentrations of GK used were 1.2, 3.7, 11.1, 33.3, 100 and 300 nM (0.069, 0.21, 0.62, 1.9, 5.6 and 16.8 mg/mL). 122

Figure 4.10 A fit of the Langmuir 1:1 model (red solid line) to the data collected (black solid symbols) during the interaction between CAH and lipid bilayer modified with 5:2 SM:CH ratio is shown. Table 4.1 at the bottom indicates the fitted parameters. 125

Figure 4.11 Log of affinity constant obtained by Langmuir model is plotted against the log of concentration of the CAH for lipid bilayer films modified with (a) 5:2 and (b) 5:3 SM:CH ratios. Average affinity constant obtained during three trials is given with the error bar indicating the standard deviation between the calculated affinity constants. 127

Figure 4.12 Fit of the heterogeneous ligand 1:2 model (red solid line) to the data collected (black solid symbols) during the interaction between CAH and lipid bilayer modified with 5:2 SM:CH ratio. Table 4.2 at the bottom indicates the fitted parameters. 129

Figure 4.13 Log of affinity constants obtained by heterogeneous ligand model is plotted against the log of concentration of the CAH for lipid bilayer films modified with (a) 5:2 and (b) 5:3 SM:CH ratios. Average affinity constants, K_{D1} (black) and K_{D2} (red), obtained during three trials is given with the error bar indicating the standard deviation between the calculated affinity constants. 130

Figure 5.1 a) Normalized absorbance (solid line) and emission (dashed line) spectra of 2.5, 3.0, and 3.4 nm QDs in octane; b) AFM image of 3.0 nm PbS QDs that are cross-linked with EDT on Au; and c) height profile of the scratched QD film. 146

Figure 5.2 UPS spectra (a) and cyclic voltammogram (b) of 3.0 nm PbS QDs that are cross-linked by EDA to determine the VBM and CBM respectively. UPS of the onset region (a, left) and the

full spectra (a, right) are shown. The red dashed line in both the UPS spectra and voltammogram show the onset potential associated with the corresponding electronic states..... 147

Figure 5.3 Electronic states of PbS monolayers determined by cyclic voltammetry (a) and photoelectron spectroscopy (b) are plotted versus the three different ligands used for cross-linking: EDA (black), EDT (red), and BDT (blue). Stars are representative of the experimentally determined values and a combination of the optical band gap and exciton binding energy was used to calculate the other bandedge. The S, M, and L represent the three different QD diameters 2.5 nm, 3.0 nm, and 3.4 nm, respectively. The dashed black line corresponds to the bulk CBM of PbS and the gray bar illustrates that all of the experimental UPS data fall within the error associated with the UPS measurement 5.6 ± 0.1 eV. The error bars in the UPS measurement are a result of instrument resolution and the error bars in the electrochemistry data are representative of the standard deviation of multiple measurements..... 149

Figure 5.4 Diagram (a) shows a schematic of the substrate configuration used in this part of the study and diagram (b) shows the UPS determined energy band positions of the PbS monolayers. In b) the VBM and CBM are presented as relative shifts from the Au Fermi level ($E_f = 0$ eV) for two different size QDs and three different thicknesses of alumina. The black boxes correspond to the band edge positions and their shift from E_f is provided next to the double headed arrow. .. 150

Figure 5.5 VBM (black symbols) and CBM (red symbols) of PbS monolayers with 2.5 nm (open symbols) and 3 nm (closed symbols) size QDs, as determined by UPS. Diagram (a) is on the bare Au part of the substrate and diagram (b) is for the part of the substrate covered with 3.0 nm of alumina. Three different cross-linkers were studied: BDT, EDT and EDA. Energy level positions are reported with respect to the Au Fermi edge in the UPS spectra. 151

LIST OF EQUATIONS

Equation 1.1	3
Equation 1.2	4
Equation 1.3	5
Equation 1.4	6
Equation 1.5	6
Equation 1.6	8
Equation 1.7	8
Equation 1.8	11
Equation 1.9	11
Equation 1.10	15
Equation 1.11	15
Equation 1.12	15
Equation 1.13	20
Equation 1.14	21
Equation 1.15	21
Equation 1.16	22
Equation 1.17	23
Equation 1.18	23
Equation 1.19	23
Equation 1.20	24
Equation 1.21	24

Equation 1.22	24
Equation 2.1	44
Equation 2.2	44
Equation 3.1	83
Equation 3.2	86
Equation 4.1	115
Equation 4.2	118
Equation 4.3	118
Equation 4.4	123
Equation 4.5	124
Equation 4.6	124
Equation 4.7	124
Equation 4.8	124
Equation 4.9	125
Equation 4.10	126
Equation 4.11	128
Equation 4.12	128
Equation 4.13	128
Equation 4.14	128
Equation 4.15	128
Equation 4.16	128

DEDICATION

In Loving Memory of My Parents

Ammi and Thatthi

ACKNOWLEDGMENTS

Last five-six years have been a time of intense learning for me, both on professional as well as on personal level. I truly feel grateful to many people who have supported and helped me throughout this period.

First, I would like to express my sincere gratitude to my advisor, Prof. David Waldeck for his patience, motivation, and his immense knowledge. He has always been understanding and supportive through many challenging moments I faced through these years. His guidance and support helped me in developing a good skillset as a scientist and greater appreciation for nanotechnology and chemistry.

In past years I was privileged to work with wonderful professors and great scientists who have helped a lot to shape my thinking. I would also like to thank Prof. Steve Weber and Prof. Jill Millstone for serving in both my comprehensive and dissertation committee, and also for insightful comments which prompted me to widen my research from various perspectives. I owe my sincere thanks to Prof. Linda Peteanu for serving in my dissertation committee and for all the support. I would like express my sincere thanks to Prof. Jianjun Wei from University of North Carolina at Greensboro (past CFD Research Corp, AL) with whom I have been privileged to work with from the time I started in graduate school. It has been a great experience to work with Prof. Joanne Yeh group in Structural Biology Department and I would like to thank especially Dr. Haibin Shi with whom I worked for long tedious hours collecting data.

I owe my thanks to all the staff members, especially Mr. Mike McDonald, Mr. Matt France and Dr. Susheng Tan, at Peterson Institute for Nanoscience and Engineering, University of Pittsburgh. I spent a lot of my time in the nanocenter as a graduate researcher and was able to learn

many aspects in nanofabrication and characterization which helped me in developing a good skillset in the area. I would like to thank all the staff members in Nanofabrication Facility in Carnegie Mellon University for their help and technical guidance. Many thanks to Dr. Joel Gillespie from Material Characterization Lab, Department of Chemistry for all his help and technical support. I would like to thank Mr. Tom Harper, at the Microscope and Imaging Facility, Department of Biology for his helpful insight and technical support. The machine shop, especially Mr. Tom Gasmire, have been immensely helpful with the design of specialized devices for my experiments. I thank all staff at Department of Chemistry for all the support and smiles that I received through these years.

The members of the Waldeck group have contributed immensely to my time at Pitt. The group has been a source of friendship as well as good advice and collaboration. I'm especially grateful to Dr. Matt Kofke for helping me to get accustomed to my research project when I was starting my graduate research. I am also grateful to have worked with and learned from Dr. Emil Wierzbinski, Dr. Himadri Mandal, Dr. Yang Wang, Dr. Xing Yin, Dan Lamont, Brian Bloom, Brittney Graff, Ed Beall, Arthur Davis and Simon Wei.

I gratefully acknowledge the funding sources that made my Ph.D. work possible. In the past five years my work was supported by the National Institute of Health and the U.S. Department of Energy. I was also funded by PBC fellowship, Arts & Sciences fellowship and Ashe Summer fellowship from University of Pittsburgh.

My time in Pittsburgh, many thousands of miles away from home, was made enjoyable in large part by many friends and groups that became a part of my life. I'm grateful to Pavithra, Nilini, Lalangi, Kalindi, Munira, and all my friends for the true friendship and all the encouragement that I received, which helped me to keep my perspectives straight through many challenging times. I'm

grateful for all the help and support that I received from the Sri Lankan community in Pittsburgh and for being a second family away from home. My time in Pittsburgh have become an enriching experience on many personal levels thanks to the Pittsburgh Buddhist center and its resident monks, who provided me with spiritual guidance that helped immensely to develop a larger viewpoint on life.

I owe my heartfelt gratitude to many special people in my life for helping me to accomplish this goal in life. Tharaka, thank you for all the unconditional love, support, encouragement and patience. You have been there for me in my good times and bad times. I love you and I cannot wait to start our lives together. Muthu and Menu, thank you for being wonderful and courageous sisters. We three made it together through many challenges and I'm truly feel grateful for all your advice, encouragement and love that made it possible for me to get this far. Sudu Mamma, Seeya, Nono, Mammo and all Mamas, thank you for taking care of me and my sisters through the toughest times and for all the love and support. Chuti Ayya and Ranitha Akka, thank you for everything.

All these accomplishments were made possible by the two courageous people I feel most grateful to, my loving mother and my loving father, who put our education to their top priority and sacrificed a lot to pave a path towards our success. Though they both are no longer here with me today, I'm sure they would have been very proud to see what I have achieved thus far. Ammi and Thatthi, I miss you a lot. May you both attain supreme bliss of Nibbana!

1.0 INTRODUCTION

The interest in nanoscale materials derives from the interesting properties they exhibit which are distinct from those of the bulk materials. Often the nanomaterials properties change as their size and shape changes. In noble metals, when the dimensions are reduced to tens of nanometers, a new absorption peak arises resulting from the collective oscillations of electrons in the conduction band. This phenomena is called surface plasmon absorption. In semiconductors, as the dimensions are reduced to become comparable or smaller than the electron's wavefunction, electrons "feel" the presence of the particle boundaries and respond to changes in the particle size by changing their energy. This phenomena known as quantum confinement, can localize and stabilize the electron-hole pair, creating an exciton. As a result, new absorption features arise in semiconductor nanoparticles because of the confinement of the exciton. The interest on these nanomaterials has experienced enormous growth over the past few decades, often driven by the excitement in understanding the new science and application of it for economic growth.

The studies in this thesis explore the light matter interactions of nanomaterials, with the aim of using them in sensing and photovoltaics applications. The first part of the introductory chapter describes the interaction of electromagnetic radiation with metallic nanostructures, leading to surface plasmon excitations, and how the refractive index sensitivity of surface plasmons stems from the fundamental physics of their excitation. The second section of this chapter describes the quantum confinement effects that arise in semiconductor nanoparticles and how it affects their

electronic state energetics. The third section describes photonic band gap materials which arise in periodic dielectric media. The chapter ends with a discussion of how these properties are used in third generation photovoltaics for efficiency enhancement.

1.1 INTERACTION OF LIGHT WITH NANOSCALE METALLIC STRUCTURES

This section describes how the interaction of light with metallic nanostructures gives rise to resonant plasmonic excitations and their refractive index sensitivity. A discussion about the performance characteristics of surface plasmon resonance (SPR) based sensors, as well as an introduction to the computational electromagnetic calculations method, finite difference time domain (FDTD), is included in the latter part of this section.

Plasmonics is a subfield of nanophotonics that is concerned with how electromagnetic fields can be confined on nanometer scale lengths. This field is concerned primarily with the interaction between electromagnetic radiation (EM) and conduction electrons at metallic interfaces or in small nanostructures of subwavelength dimensions, which leads to enhancement of the optical near field. Since the discovery of extraordinary optical transmission by Ebbeson¹, this field has attracted the attention of physicists, chemists, biologists, and material scientists for widespread use in areas such as electronics, optical sensing, biomedicine, data storage, and light generation.^{2,3}

Surface plasmons are very sensitive to the near surface dielectric constant and are well suited for the detection of surface binding events. Hence, surface plasmonic effects have been widely used in sensors, particularly for sensing biological interactions. When contrasted with other traditional methodologies like Enzyme-Linked Immuno Sorbent assay (ELISA), biosensing with surface plasmon resonance (SPR) provides advantages of real time, label free detection for a

variety of analytes.³⁻⁶ Two types of surface plasmon resonances are used in surface based sensing applications, propagating surface plasmon polaritons (SPP) and localized surface plasmon resonance (LSPR).

1.1.1 Surface Plasmon Polaritons

The optical properties of subwavelength apertures in metallic films have been the focus of much research. In their original work, Ebbensen and coworkers¹ discovered that subwavelength holes in optically thick metallic films could transmit certain wavelengths with efficiencies greater than unity, when normalized to the open area of the aperture. As for the underlying mechanism for this extraordinary property, it is now widely accepted that surface plasmons (SP) excited in these nanostructures play a key role. An SP arises from the collective motion of the electron charge density at a frequency corresponding to the quantized harmonic oscillation of that charge density at the surface of a metal (Figure 1.1).² When these electron charge density oscillations couple with the electromagnetic field, it results in a quasi-particle known as a surface plasmon polariton (SPP). The interaction between an SP and electromagnetic radiation occurs under the conditions where both the frequency and the momentum of the SP and the incoming electromagnetic radiation are matched.⁷ Under the above conditions for SP excitation, Maxwell's equations yield the dispersion relationship for a surface plasmon polariton (SPP), given by the Equation (1.1).⁸

$$k_{sp} = k_0 \sqrt{\frac{\epsilon_m \epsilon_d}{\epsilon_m + \epsilon_d}} \quad \text{Equation 1.1}$$

In the above equation k_{sp} is the wavevector of the SPP excitation, k_0 is the wavevector of the photons in free space, and ϵ_m and ϵ_d are the dielectric constants of the metal and the surrounding dielectric, respectively.

Over a wide range of frequencies, the optical properties of a metal can be explained by a plasma model, in which the metal is considered to be a gas of free electrons. The dielectric response of a free electron gas is approximated by the Drude model⁸ as given by the Equation (1.2).

$$\epsilon(\omega) = 1 - \frac{\omega_p^2}{\omega^2 + i\gamma\omega} \quad \text{Equation 1.2}$$

1.2

As Equation 1.2 shows the real part of the dielectric constant (ϵ) of the metal will be a negative value for frequencies $\omega < \omega_p$. For frequencies ω larger than ω_p (plasma frequency), the metal is transparent to incoming radiation, leading it to lose its ‘metallic character’. The parameter γ is the characteristic collision frequency, which relates to the damping of the electron oscillations. Because the real part of the dielectric constant of the metal is negative for the typical light frequencies under consideration, Equation (1.1) has a meaningful solution when the real part of the permittivity of the metal and dielectric material have opposite signs and also the numerical value of the real part of ϵ_m is greater than that of the dielectric. These conditions must be fulfilled by both the metal and the dielectric in order to support SPP excitation at the interface.

Once the light has been converted into an SPP mode, it propagates on the metal dielectric interface until it gradually attenuates due to absorption losses coming from the metal and radiative losses by coupling into electromagnetic radiation. Writing k_{sp} as a complex quantity, $k_{sp} = k'_{sp} + ik''_{sp}$, the decay length (l) can be approximated by the following Equation (1.3),

$$l = \frac{1}{2k_{sp}''}$$

Equation

1.3

where k_{sp}'' is the imaginary part of the complex wave vector of SPP propagation. This value is in the range of $\sim 10 \mu\text{m}$ for Au and Ag in the visible range.⁷

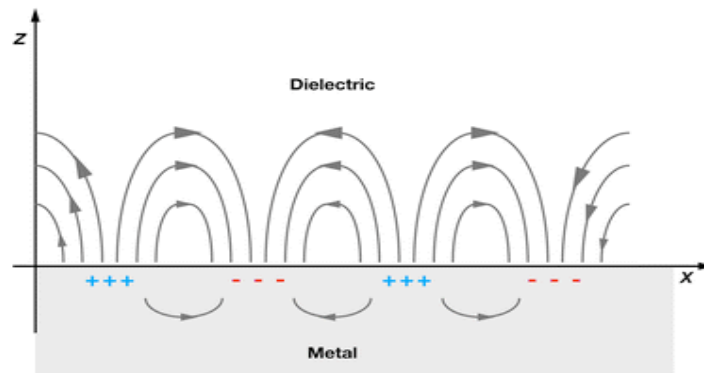


Figure 1.1 This schematic diagram illustrates the electric field contours for SPP propagation along a metal/dielectric interface (x and y directions). The field decays evanescently in the z direction, reflecting the bound and nonradiative nature of SPP. The decay length of the SPP field amplitude is greater towards the dielectric side, as compared to the metal side. This figure is taken from reference [2].²

Due to their transverse magnetic character and surface nature, the SPP has its electric field normal to the surface. The electric field is a maximum on the interface and decays both into the metal δ_m and into the dielectric δ_d with a characteristic decay length; ie. the length at which the

electric field amplitude decreases by $1/e$.⁹ These decay lengths or skin depths are expressed by the following Equations (4 and 5).

$$\delta_d = \frac{1}{k} \left[\frac{\varepsilon_d + \varepsilon_m}{-\varepsilon_d^2} \right]^{\frac{1}{2}} \quad \text{Equation 1.4}$$

$$\delta_m = \frac{1}{k} \left[\frac{\varepsilon_d + \varepsilon_m}{-\varepsilon_m^2} \right]^{\frac{1}{2}} \quad \text{Equation 1.5}$$

For a free space wavelength of 600 nm, $\delta_d \approx 390$ nm and $\delta_m \approx 24$ nm for silver in contact with air, whereas $\delta_d \approx 257$ nm and $\delta_m \approx 31$ nm for gold in contact with air. When excited at a quartz-gold interface $\delta_d \approx 100$ nm and $\delta_m \approx 28$ nm at a wavelength of 600 nm. For a gold-air interface, $\delta_d \approx 444$ nm and $\delta_m \approx 19$ nm at a free space wavelength of 800 nm. These solutions show that the penetration depth in the dielectric is larger than that in the metal, and the difference in the penetration depths becomes quite distinct for long wavelengths.^{4,9} It is this evanescent field in the dielectric that is exploited for sensing, via a change in the optical properties of the dielectric near the surface of the metal film.

As Figure 1.2 (a) illustrates, a SP has a greater momentum ($\hbar k_{sp}$) than a free space photon ($\hbar k_0$) of a given frequency, giving rise to a momentum mismatch. Therefore, an SPP on a flat metal surface cannot be excited by an incoming plane wave. There are three main ways through which the missing momentum can be provided. As illustrated in Figure 1.2 (b), the first makes use of prism coupling to increase the momentum of the incident EM radiation.^{7,8} The second uses surface defects to scatter the incoming radiation and excite SP locally. The third technique is to corrugate the surface periodically (Figure 1.2 (c)).

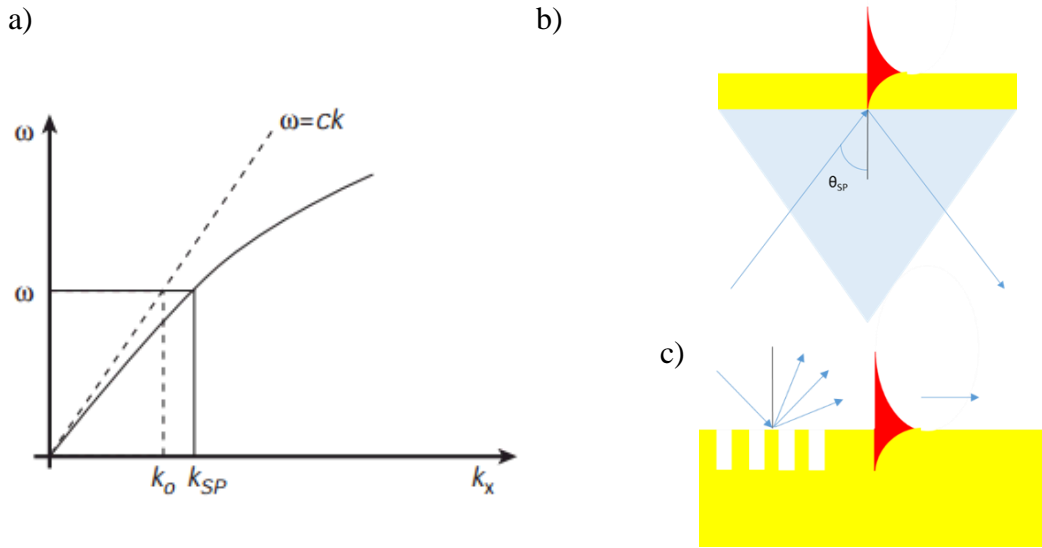


Figure 1.2 (a) Plotting equation 1 shows that the momentum (wavevector) of a surface plasmon polariton (solid line) is always greater than that of free-space light (dashed line). This dispersion curve for the SP mode illustrates the momentum mismatch problem, the SP mode always has greater momentum (k_{sp}) than a free space photon (k_0) of the same frequency ω . This diagram is taken from reference [9].⁹ The most commonly used ways to provide missing momentum is by using (b) prism coupling method and, (c) surface corrugation.

Sensing based on SPRs can be achieved in a variety of ways. Most of the commercial instruments for refractive index sensing based on this phenomenon utilize thin metal film based chips. Attenuated total internal reflection of a light beam through a prism is used to excite the SPP in the thin metal film (Figure 1.2 (b)). In this configuration, a beam of light with momentum k is reflected at an interface between an insulator with higher dielectric constant ϵ , usually in the form of a prism and a metal film. The projection of the momentum along the interface will have a value $k_x = k\sqrt{\epsilon} \sin \theta$, in which θ is the angle of the incident light normal to the surface. Binding of molecules to a functionalized film is monitored as a change in the incident angle required for

SP excitation. Though these thin metal film based sensors are known to be very sensitive to surface environmental changes, the difficulty for miniaturization due to bulkiness of the instrumentation and requirement of large sample volumes, limits the ability for it to be deployed in high throughput chip based detection schemes especially in biosensing studies.

1.1.1.1 Nanoslit arrays

When the metal surface is corrugated in the form of a one dimensional grating with a periodicity p , as illustrated in Figure 1.3, the incident light diffracts and obtains an increased in-plane momentum. The phase matching condition is obtained when the momentum of the surface plasmon on the metal nanoslit surface (k_x) is matched by the incoming photons incident at an angle θ fulfill following relationship.

$$k_x = k \sin \theta \pm j \frac{2\pi}{p}$$

Equation 1.6

In equation 1.6, $j = 1, 2, 3, 4 \dots$ and k is the wavevector of the incoming photon. In these types of arrays, at normal incidence of light ($\theta = 0$), the dispersion relationship is modified and gives rise to Equation 1.7, which approximates the resonance wavelength SP excitation (λ_{spp}).

$$\lambda_{spp} = \frac{p}{j} \sqrt{\frac{\epsilon_m \epsilon_d}{\epsilon_m + \epsilon_d}} \quad j = 1, 2, 3 \dots$$

Equation 1.7

A slit array that has been supported on a substrate, is expected to have transmission peaks associated with SPP modes of both the metal-dielectric and the metal-substrate interfaces. As can be noted from the equation these resonances depend on the periodicity p of the slit array. At the same time, modes arise from cavity resonances located inside the slits. These resonances, unlike periodicity dependent SPP modes, are localized in nature and therefore have a strong dependence on the width and the length of the slit (film thickness). It is evident from the above relationship that as the refractive index (RI) of the metal surrounding environment changes, the phase matching conditions for SP excitation changes, giving the ability for nanoslit arrays to be used in refractive index sensing studies.

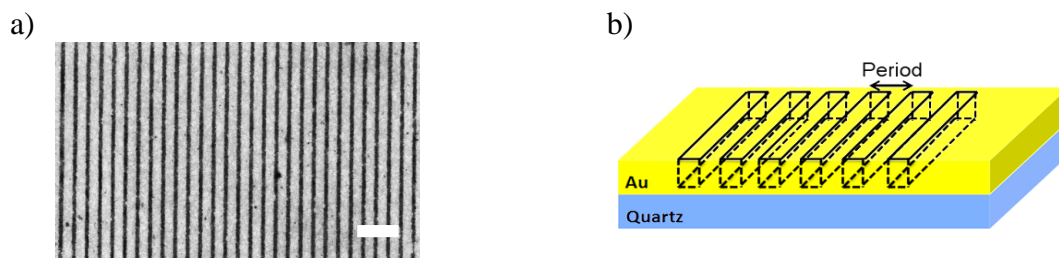


Figure 1.3 a) SEM image of a Au nanoslit array which was fabricated by the thesis author using electron beam lithography. The scale bar is 2 μm . b) A schematic of a nanoslit array.

1.1.2 Localized Surface Plasmon Resonance

For many hundreds of years noble metal nanoparticles (NPs) have been used for staining glass, because of the striking bright colors they exhibit under both transmitted and reflected light. This phenomenon arises because these NPs interact strongly with visible light when excited at their dipole surface plasmon frequency.

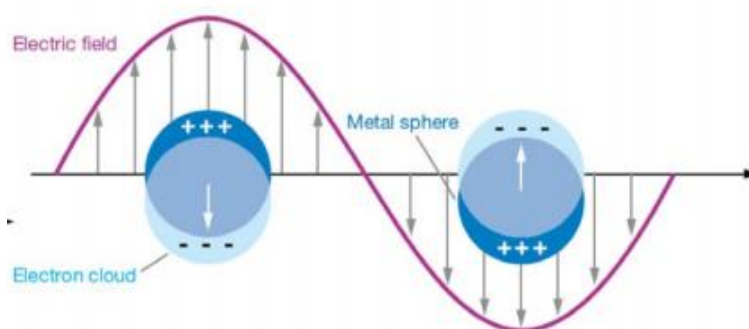


Figure 1.4 This figure illustrates the excitation of localized surface plasmon resonances in nanoparticles, showing the restoring force induced and the driving force of the EM radiation which causes the charge displacement. This figure is taken from reference [2].²

When a NP is exposed to an oscillating electromagnetic field it drives a charge displacement of the electron cloud, and the metal ion core of the particle exerts an effective restoring force on the driven electrons. A resonance excitation (Figure 1.4) of these electron charge density oscillation by electromagnetic fields results in a strong light scattering, in the appearance of intense absorption bands, and an enhancement of the local electromagnetic fields.¹⁰ This resonance is called the localized surface plasmon resonance (LSPR). Because of the surface potential the momentum condition is satisfied and the LSPR of a nanoparticle can be excited from direct light illumination, in contrast to propagating SPPs, which require phase matching. At LSPR

wavelengths, the plasmon oscillations in the nanoparticles reach their maximum amplitude. The increased scattering and absorption that results lead to transmission minima, which can be observed as dips in the transmission spectra.

For a nanoparticle with a size much smaller than the wavelength of the incident light, the phase of the harmonically oscillating EM field can be approximated as constant over the total volume of the NP. Under this approximation the polarizability (α) of a small spherical particle can be expressed as

$$\alpha = 4\pi\epsilon_0 R^3 \frac{\epsilon_m - \epsilon_d}{\epsilon_m + 2\epsilon_d} \quad \text{Equation 1.8}$$

with radius R and dielectric function ϵ_m surrounded by a host medium with dielectric constant ϵ_d . It is apparent from the above equation that the polarizability experiences a resonant enhancement under the condition where the denominator becomes a minimum, namely when,

$$\epsilon_m = -2\epsilon_d \quad \text{Equation 1.9}$$

The relationship in Equation 1.9 is known as the Fröhlich condition. For a sphere consisting of a Drude metal located in air, the condition is met at the frequency $\omega_0 = \omega_p/\sqrt{3}$, meaning that the LSPR occurs at a frequency below the plasma frequency of the metal. The Fröhlich condition also expresses the strong dependence of the resonance wavelength on the dielectric constant of the surrounding medium of the metal NP. The position of the resonance red shifts as ϵ_d increases, which is the basis of refractive index (RI) sensing using metal nanoparticles. During the resonance

process a dipolar field is produced outside the NP, leading to enhancement of the near field in the immediate vicinity of the particle³. The decay length of the dipolar near field defines the sensing volume of a LSPR based sensor. Comparing the decay lengths of the plasmonic fields produced by the SPP excitation, the decay lengths produced by the LSPR are an order of magnitude shorter. Due to such tight confinement of the optical energy, LSPR active nanostructures are highly sensitive to surface properties.

Additionally, the size and the shape of an NP can influence the resonance wavelength of the nanoparticles. The distance between charges at opposite interfaces of the particle increase with the size of the NP leading to a smaller restoring force, thereby shifting the resonance to longer wavelengths. Another consequence of being larger sized particles is that a finite phase delay between the front and back of the particle can occur, leading to excitation of multipolar modes.^{3,8} For nonspherical metallic NPs, an uneven distribution of the surface plasmons around them becomes manifest as a shape dependence for the LSPR extinction spectra.³

1.1.2.1 Nanoparticle chains

When metallic NPs are arranged in an ordered array, they interact, leading to new interesting optical resonances in the extinction spectrum. Depending on the polarization of the incident light, the plasmonic resonance splits and shifts relative to those of non-interacting NPs. When a NP of size a is arranged in an ordered one-dimensional array with inter-particle spacing d , such that a is much smaller than d , the particles can be treated as point dipoles (Figure 1.5). Depending on the spacing between adjacent NPs, two regimes of interactions can be distinguished. For closely spaced particles, where the inter-particle spacing (d) is smaller than the incident

wavelength (λ), near field interactions with a distance dependence d^{-3} dominates and for widely separated NPs where d is larger than λ , far field interactions with a distance dependence d^{-1} dominate.^{11,12} When the spacing between two NPs approaches the wavelength of LSPR excitation in a single NP, a resonant far field interference becomes especially important and leads to pronounced changes in the extinction spectra of the system.¹³ Near field coupling dominates in systems where the NP is separated by a few particle diameters a , due to its d^{-3} dependence coupling rapidly decreases.

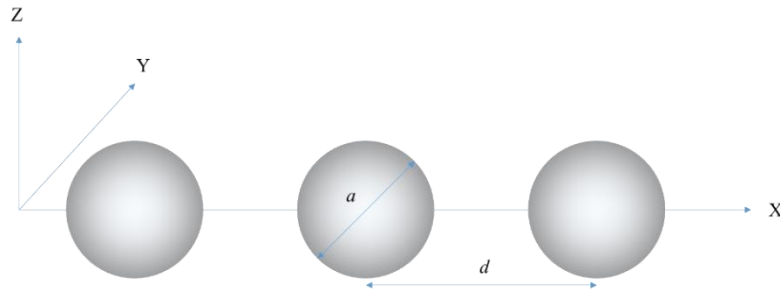


Figure 1.5 Linear chain of equidistantly spaced spherical nanoparticles with diameter a and with the distance d between the centers of the particles. The incident plane electromagnetic wave propagates in the z direction.

When nanoparticles interact with their near fields, the resonance shifts because of the Coulombic interaction. Depending on the direction of light polarization, modes of a nanoparticle chain fall into two categories. As illustrated in Figure 1.6, when light is polarized along the long axis of the chain, the dipoles are arranged along the chain, giving rise to a longitudinal mode. For a longitudinal mode, coupling to the neighboring NP decreases the restoring force and a red shift is observed for the plasmon resonance wavelength. In contrast, the resonance of a transverse polarized mode, light polarized perpendicular to the chain, displays a blue shift. As Figure 1.6

shows, dipoles arranged in this way couple to neighboring particles to increase the restoring force, hence a blue shift is observed.



Figure 1.6 Nanoparticle coupling under a longitudinal restoring force (a) shifts the resonance to lower frequency and nanoparticle coupling under a transverse polarization (b) increases the restoring force through coupling to neighbors shifting the resonance to higher frequency.

1.1.3 Refractive index sensing using SPR

The SPR response of nanostructured films is also highly sensitive to refractive index changes in their surrounding environment. These nanostructured films can consist of either nanoaperture or nanoparticle arrays and the dielectric constant of the surrounding medium causes changes in the response of the SPP, the LSPR, or their combination. Because these structures are tens to hundreds of nanometers in size, an entire array of apertures can be fabricated in an area of a hundred square microns. With recent advances in nanofabrication methodologies precise control of size, shape, and/or spacing can be realized, giving the capability to modulate the optical response of these nanostructures, and thus their sensitivity. The ability for miniaturization and ease of transmission measurements, as opposed to reflection methods in thin film based SPR, makes these devices very promising in future sensing applications.

The sensing performance of an SPR based sensor is characterized by the resonance wavelength shift ($\delta\lambda$) which arise from changes to the bulk RI (δn) in the surrounding medium, defined by the equation 1.10.

$$S_{bulk} = \frac{\partial\lambda}{\partial n} \quad \text{Equation 1.10}$$

To compare the sensors in a way that accounts for the condition of the resonances, a figure of merit (FoM) is defined by the equation,

$$FoM = \frac{S_{bulk}}{\Delta f} \quad \text{Equation 1.11}$$

where Δf is the full width of the resonance at its half maximum. To understand the wavelength shift response of an SPR based sensor ($\Delta\lambda$) upon molecular adsorption, the following equation is often used.^{5,14}

$$\Delta\lambda = m(n_{adsorbate} - n_{bulk})[1 - e^{-\frac{2d}{\delta_d}}] \quad \text{Equation 1.12}$$

where m is the refractive-index sensitivity, $n_{adsorbate}$ and n_{bulk} are the refractive index of the adsorbate and surrounding medium, d is the effective adsorbate layer thickness, and δ_d is the characteristic electromagnetic field decay length. This model assumes a single exponential decay of the electromagnetic field normal to the planar surface, which is accurate for a propagating

surface plasmon but is undoubtedly an oversimplification for the electromagnetic fields associated with noble metal nanoparticles.

As illustrated by Figure 1.7, if molecular binding on the metal surface creates a thin film (e.g - formation of a self-assembled monolayer of thiols), the molecules will proportionally modulate the effective refractive index seen by the SP, causing a shift in the resonant wavelength as predicted by the Equation (1.12). If the thickness (t_{film}) of an adsorbed film is much larger than δ_d , then the SP wave senses the “bulk” refractive index of any adsorbed molecules. If t_{film} is less than δ_d , then the effective refractive index n_{eff} seen by the SP wave is calculated by a weighted average of the dielectric function above the metal surface as given by the Equation (1.12).

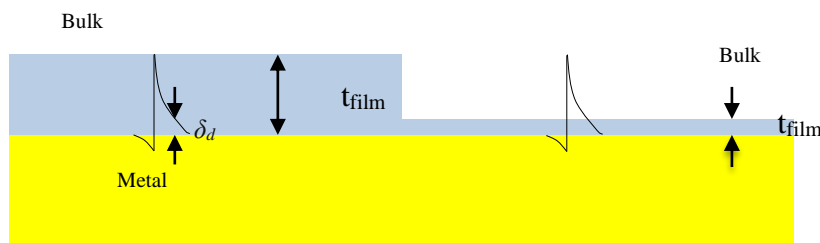


Figure 1.7 Effective refractive index of a thin film. On the left hand side, the extension of the SPP field in the z direction is entirely within the bulk of the thin film, in that $\delta_d < t_{\text{film}}$. When $\delta_d > t_{\text{film}}$, the effective index seen by the evanescent SPP field, must be calculated as a weighted average of n_{bulk} and $n_{\text{adsorbate}}$.

In general the performance of an SP sensor increases with the amount of field confinement on the dielectric side. Inherent from the localized nature, the δ_d is known to be shorter in a LSPR based sensor as compared to an SPP based sensor. This fact makes the LSPR based nanoparticle sensors more sensitive in detecting surface binding events; SPP based sensors are more sensitive to bulk refractive index changes, given their long δ_d as well as propagation along the metal-

dielectric interface. Thus the sensitivity of SPP based sensors to molecular adsorbents on the surface is dependent on the amount of field confinement and on the magnitude of the attenuation length on the interface.

1.1.4 **Finite difference time domain calculations**

Classically, all electromagnetic phenomena can be described by using Maxwell's equations. These foundational equations describe electromagnetic fields and how they evolve over time. Maxwell's equations can only be solved analytically for a small set of simple geometries, such as spherical metallic nanoparticles, planar metallic films, or simple SPP waveguide structures. For any other geometry, they must be solved numerically. The finite-difference time-domain (FDTD) algorithm is one of the most widely used methods for performing such numerical experiments, calculating the propagation of electromagnetic fields through complex materials with arbitrary geometries.

In this method the structure of interest is discretized onto a grid and each grid cube has a specified index of refraction. To obtain accurate results, the spatial grid must also be small enough to resolve the wavelength of the light or the smallest structural feature. Since Maxwell's equations dictate that a temporal change in electric field is related to a spatial change in magnetic field, and vice versa, a time step is also defined for fields to travel from one cell to the next. Even though the FDTD method provides a convenient, systematic and general approach for calculating the optical response of nanostructures of arbitrary symmetry and geometry, there are, several important limitations to the FDTD algorithm, the most severe being the intensive computational resources required for a full three-dimensional calculation.

1.2 INTERACTION OF LIGHT WITH NANOMETER SCALE SEMICONDUCTOR STRUCTURES

This section describes how interaction of light with semiconductor nanostructures leads to interesting properties, which arise from quantum confinement of the electron and holes.

1.2.1 Inorganic Semiconductor Nanoparticles

Semiconductor nanoparticles are a class of nanomaterials that are the subject of diverse fundamental and applied research efforts. These materials exhibit novel size dependent optical and electronic properties that are uniquely linked to the nanoparticle size. These properties emerge from quantization effects, namely charge carriers (electrons and holes) are confined by potential energy barriers to a dimension that is smaller than the de Broglie wavelength of the carriers. The length scale at which these effects become manifest is less than 10 nm – 20 nm for most semiconductors (e.g – CdSe, CdTe), but can be as high as 30 -50 nm for semiconductors with higher electron effective mass (e.g. – PbSe, PbS).¹⁵ When charge carriers are confined in one dimension, it produces quantum wells (carrier is confined in one dimension and delocalized in the other two) while two dimensional confinement give rise to quantum wires and rods (delocalized in one dimension). Three dimensional confinement leads to quantum dots. The density of electron states for bulk and size-quantized semiconductor are depicted in Figure 1.8.

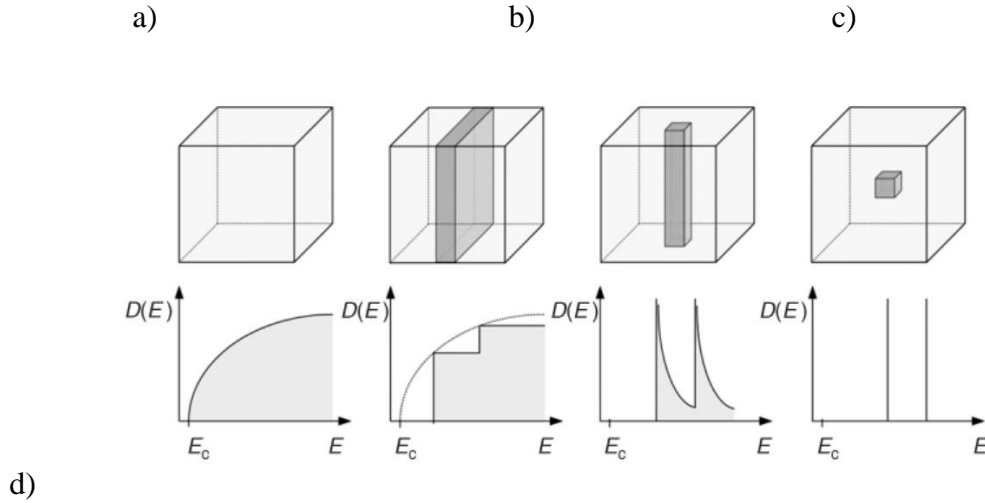


Figure 1.8 Schematic representation of effects of quantum confinement on the density of states moving from (a) bulk to (b) one dimensional quantum confinement in quantum wells, (c) two dimensional quantum confinement in quantum wires, and (d) three dimensional quantum confinement in quantum dots. It can be noted that three dimensional quantum confinement leads atom like delta function is obtained for density of states. This figure is taken from reference 16.¹⁶

Reducing the quantum dot (QD) size increases the carrier confinement, widens the electronic bandgap, and shifts the absorption and emission spectra to higher energy (shorter wavelength). Therefore the band gap of the colloidal quantum dots can be tuned by changing their size. The size of the quantum dots also determines their extinction coefficient, as the number of constituent atoms and bonds which determines the oscillator strength also changes with the nanoparticle size. The extinction coefficient for quantum dots ranges from 10^5 to $10^6 \text{ M}^{-1} \text{ cm}^{-1}$ at their first excitonic absorption peak, increasing toward UV wavelengths.¹⁷ These extinction coefficient values are about 100 times larger than that of organic dyes used in most dye-sensitized solar cells which have molar extinction coefficients usually around $2.5 \times 10^4 - 2.5 \times 10^5 \text{ M}^{-1} \text{ cm}^{-1}$ at the absorption maximum.¹⁷ Quantum dots are also largely photostable, as compared to organic

dye molecules which bleach when exposed to high fluxes of light. In quantum dots the limited number of electrons results in discrete quantized energies.

1.2.1.1 Quantum Confinement Effects in Semiconductor Quantum Dots

The first approximation for quantum effects in semiconductor QDs was presented by Brus and is called the “effective mass approximation” (EMA).^{18,19} In this approximation an exciton is considered to be confined in a sphere with a radius R , and the masses of the electron and hole are replaced by effective masses, as used for carriers in bulk semiconductors. The expression for the bandgap energy is

$$E_g = E_{bulk} + \frac{h^2}{8R^2} \left(\frac{1}{m_e^*} + \frac{1}{m_h^*} \right) - \frac{1.786e^2}{4\pi\epsilon_0\epsilon_r R} \quad \text{Equation 1.13}$$

In Equation 1.13, E_g is the band gap of the QD, h is the Planck constant, m_e^* and m_h^* are the effective mass of the electron and hole (respectively), e is the electron charge, and ϵ_0 and ϵ_r are dielectric constant of the vacuum and the semiconductor. The first term, E_{bulk} , in Equation 1.13 represents the band gap energy of the bulk semiconductor. The second additive term represents the energy gained by quantum confinement. This term has a R^{-2} dependence, which gives rise to the size dependence of the band gap energy. The third subtractive term corresponds to the Coulombic attraction energy of the exciton, having a R^{-1} dependence.

Because the band edge values are well known for the bulk, the valence band maximum (VBM) and the conduction band minimum (CBM) of the QDs can be estimated using the following relationships.

$$E_{VBM} = E_{VBM}^{Bulk} + E_g \left[\frac{m_e^*}{m_h^* + m_e^*} \right] \quad \text{Equation 1.14}$$

$$E_{CBM} = E_{CBM}^{Bulk} + E_g \left[\frac{m_h^*}{m_h^* + m_e^*} \right] \quad \text{Equation 1.15}$$

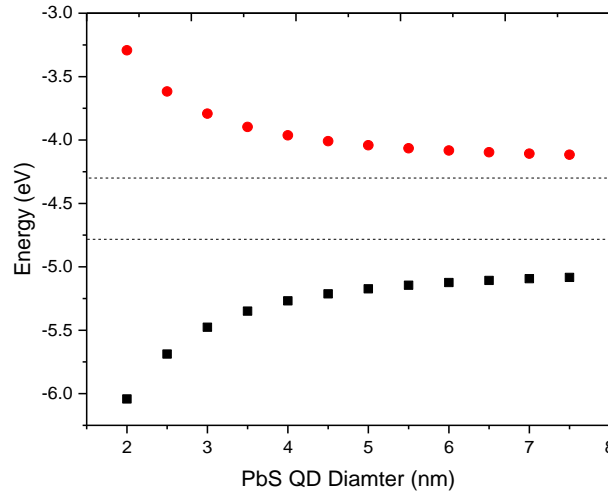


Figure 1.9 The graph shows the predicted CBM (red circles) and VBM (black squares) values for PbS QDs that the author calculated by using EMA. The dash lines indicate the bulk CBM and VBM values. For PbS, $E_g^{Bulk} = 0.41$ eV, $m_e^* = 0.4m_0$, $m_h^* = 0.33m_0$, and $m_0 = 9.1 \times 10^{-31}$ kg and $\epsilon_r^{PbS} = 17$.

Figure 1.9 shows the CBM and the VBM calculated for PbS QDs as a function of its diameter. It can be noted that the band gap, the difference between the VBM and CBM, gradually increases for smaller size QDs exhibiting quantum confinement effects. The conduction and valence band edges are also size dependent and slowly approach the bulk values and the degree of shift is dependent on the effective mass of the hole and electron for each semiconductor according

the EMA model. However, studies on many different types of QDs have shown that the most EMA, consistently overestimates the valence and conduction band size-dependent shifts because it unrealistically assumes an infinite potential barrier at the dot surface.^{20,21} Recent studies on nanocrystal energy level structures have shown that the electronic state energies of QDs are inherently coupled to their surface chemistry and surface ligands have been used to tune the absolute position of the electronic band energies of QDs.²²

1.2.1.2 Quantum Dot Solar Cells

Owing to its unique properties of ready tunability and high oscillator strength many workers are exploiting light harvesting using QDs. Recent work on multiexciton generation in QDs, in which two or more excitons can be generated with a single photon of energy greater than the bandgap, has raised the possibility of boosting the photoconversion efficiency beyond the traditional Shockley Queiseer limit.²³⁻²⁵ In addition, QDs allow solution based processing that can drastically reduce the fabrication cost. Thus QDs are promising candidates for next generation solar cells which aim to reduce the fabrication cost while increasing efficiency beyond what is available from second generation thin film based devices.^{26,27}

The efficiency (η) of a solar cell is measured by the ratio of the electrical output from the solar cell to the incident energy from the sunlight. This power conversion efficiency (PCE) is calculated according to the relationship as follow.²⁸

$$\eta = \frac{P_m}{P_{in}}$$

Equation

1.16

In Equation 1.16, P_{in} is the incident power and P_m is the maximum power output from the solar cell. The maximum output power of a solar cell can be derived by assuming that the solar cell operates as an ideal diode with excess carriers originating from solar irradiation. The current-voltage (I - V) characteristics of such a device are given by

$$I = I_s \left(e^{\frac{qV}{kT}} - 1 \right) - I_L \quad \text{Equation 1.17}$$

where I is the current output from the cell and I_s is the diode saturation current. The current produced by the excess carriers generated by solar irradiance is given by I_L . The voltage in which the cell is under is given by V , T is the temperature of the cell and k is the Boltzmann constant. This equation can be plotted to obtain the I - V characteristics of a cell as illustrated in Figure 1.10. When the applied voltage is zero ($V=0$), the equation predicts that $I = I_L$. This point on the I - V curve is known as the short circuit current (I_{SC}). The voltage at which the current produced by the cell zero ($I = 0$), is known as the open circuit voltage (V_{OC}):

$$V_{OC} = \frac{kT}{q} \ln\left(\frac{I_L}{I_s} + 1\right) \approx \frac{kT}{q} \ln\left(\frac{I_L}{I_s}\right) \quad \text{Equation 1.18}$$

It can be noted from Equation 1.18 that the open circuit voltage increases logarithmically with decreasing saturation current. The output power (P) of the cell is given by,

$$P = IV \quad \text{Equation 1.19}$$

The maximum power (P_m) produced by the cell can be obtained when $\frac{dP}{dV} = 0$ and is given by the shaded rectangle in Figure 1.10, which corresponds to the maximum area under the curve.

$$P_{max} = I_{max}V_{max} \quad \text{Equation 1.20}$$

Another defining term in the overall behavior of a solar cell is the fill factor (FF) which is defined in Equation 1.21.

$$FF = \frac{I_{max}V_{max}}{I_{sc}V_{oc}} \quad \text{Equation 1.21}$$

The FF is a measure of the "squareness" of the IV curve, a solar cell with a higher voltage has a larger possible FF since the "rounded" portion of the IV curve takes up less area. The maximum value for FF is one and lower values will result from parasitic resistive losses.²⁸ Increasing the shunt resistance and decreasing the series resistance lead to a higher fill factor, thus resulting in greater efficiency, and bringing the cell's output power closer to its theoretical maximum. With all the parameters defined above, the efficiency (η) of a solar cell can be rewritten as follow.

$$\eta = \frac{FFV_{oc}I_{sc}}{P_{in}} \quad \text{Equation}$$

1.22

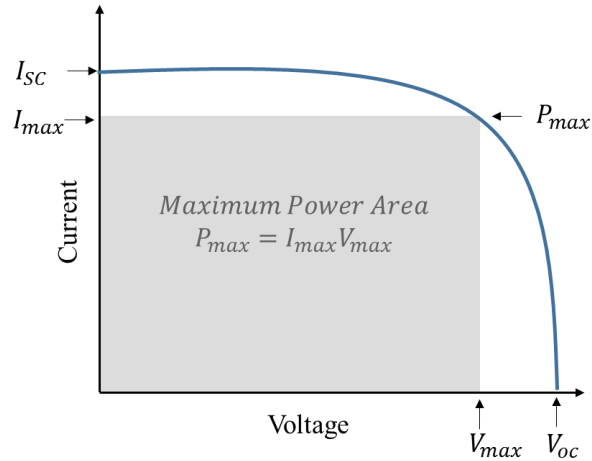


Figure 1.10 Current voltage characteristics of a solar cell under solar illumination

In photovoltaic devices, semiconductor QD films are usually combined with charge extracting electrodes and another metal (Schottky junction cells) or semiconductor (QD–QD or QD–titanium dioxide p–n junctions, or QD–QD–zinc oxide p–i–n junctions) electrode to form a complete functional device. For a functioning solar cell, the photoactive material absorbs light and generates an exciton which is then separated to produce a current.

A p–n junction solar cell (heterojunction solar cell, panel b, Figure 1.11) uses a wide band gap semiconductor, which is usually a n-type metal oxide film (TiO_2 , ZnO), with a p-type QD film.²⁹ The typical substrate consists of a glass transparent base followed by a thin transparent conductive oxide layer (Indium tin oxide (ITO) or fluorine-doped tin oxide (FTO)). The functional device is finished with a deep work function metal such as gold or a highly doped oxide (MoO_3) followed by silver or aluminum. With this design, the device is illuminated through the transparent substrate and the wide-band-gap semiconductor. A depletion zone is created when the p and n-type materials are brought together in a p–n junction device, the width of these depletion regions depend on the relative free carrier densities in the materials on either side of the junction. Drift

currents created by the electric field across the depleted region act to drive carriers in the QD film. The bulk heterojunction architecture is one strategy for overcoming the short carrier transport lengths experienced by planar p - n junction device structures. In these devices, the n -type wide-band-gap semiconductor and the QD film form an interpenetrating layer. The structured interface allows for the extension of the depletion region and the addition of more absorbing QD material. Another strategy is to use a thin layer of QD as a sensitizer on a nanoporous, high surface area wide-band-gap semiconductor layer giving rise to QD-sensitized solar cells (panel c, Figure 1.11).³⁰ Since a thin layer of absorber is used, this design has a low light absorbing capacity while it provides a good open circuit voltage and a fill factor.

In Schottky junction solar cells (panel a, Figure 1.11) the QD film acts both as the light absorber and also as the charge transport medium.²⁹ These cells are based on illumination through a transparent Ohmic contact to a QD film which forms a rectifying Schottky junction with a shallow work function metal (eg. Al). The Schottky junction is formed by Fermi level equilibration between the metal surface and the semiconductor QD. The Schottky architecture has several advantages, including ease of fabrication and a limited number of interfaces. The Schottky architecture has been limited in absolute device performance, however, mainly because of Fermi level pinning at the metal–QD interface. Fermi-level pinning imposes an upper bound on the open-circuit voltage that is well below the voltage predicted from consideration of the QD band gap alone.

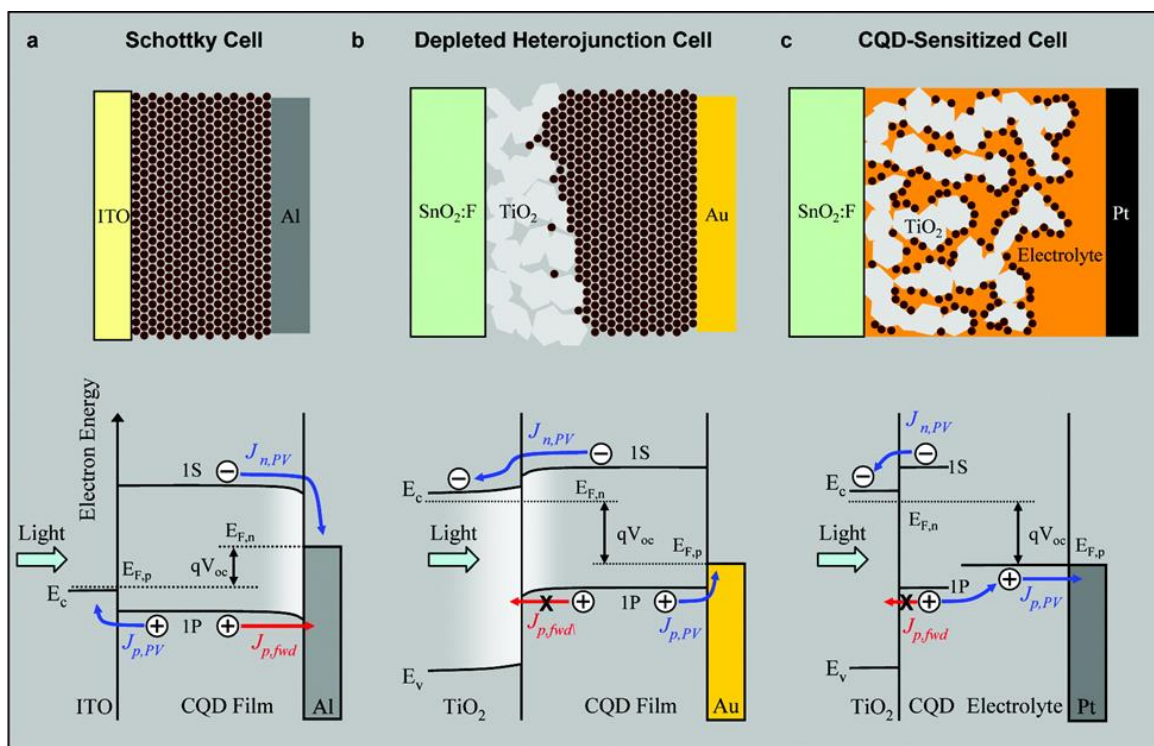


Figure 1.11 Schematic representation and working principles of (a) a Schottky junction solar cell, (b) a p-n junction solar cell with heterojunction architecture, and (c) quantum dot sensitized solar cell. Figure is taken from reference 30.³⁰

1.3 SCOPE OF THE DISSERTATION

To further the fundamental understanding and application of metallic and semiconductor nanostructures, the studies described in this thesis have investigated 1) coupling plasmonic structures with microfluidic channels for nanofluidic-plasmonic biosensing; 2) the plasmonic coupling between nanoparticles for enhancing refractive index sensing using coupled nanostructures; 3) modelling binding events using plasmonic sensing; and 4) eliminating Fermi

level pinning in semiconductor nanoparticle films. The ultimate goal of the studies in this thesis have been to explore new strategies that enhance the performance of nanomaterials in sensing and photovoltaic applications.

Chapter 2 discusses our work on a novel plasmonic structure which is integrated into microfluidic systems in order to allow in plane plasmonic biosensing. This new nanofluidic plasmonics-based sensing platform will be able to readily integrate with microfluidics devices, and potentially enable an in-parallel transmission surface plasmon resonance (SPR), lab-on-chip sensing technology. The work presented in this chapter includes an integrated device with nanofluidic nanoplasmonic arrays interfacing with microfluidic channels, and preliminary findings, from both theoretical and experimental fronts, of the device for bio-sensing.

Chapter 3 reports our studies on the observation of a delocalized surface plasmon resonance (DSPR) phenomenon in linear chains of square-shaped silver nanoparticles (NP). Transmission spectra of the silver nanoparticle chains reveal the emergence of new, red-shifted extinction peaks that depend strongly on the spacing between the nanoparticles and the polarization of the exciting light with respect to the chain axis. As the spacing between the nanoparticles in the linear chain decreases and the number of nanoparticles in the linear chain increases, the strength of the new extinction features increase strongly. These changes can be described by a tight-binding model for the coupled chain, which indicates that the origin of the phenomenon is consistent with an increased coupling between the nanoparticles. FDTD calculations reveal that the electric field is strongly enhanced between the nanoparticles in the chain. The DSPR response is found to be much more sensitive to dielectric changes than the localized surface plasmon resonance (LSPR).

Chapter 4 shows our work on the use of surface plasmon resonance (SPR) to model the binding of HIV capsid proteins to a plasma membrane. Model plasma membranes containing lipid

rafts were made on a gold film and SPR was used to detect the binding of the capsid proteins onto the raft modified plasma membrane. Binding of the HIV capsid proteins were monitored and binding constants for the interaction were calculated. This work reveals a specific interaction between the capsid proteins onto raft modified membranes.

Chapter 5 studies the effects of Fermi level pinning on the band edge positioning of PbS QDs on Au films and the use of a thin alumina layer in between a PbS QD and a Au substrate to eliminate Fermi level pinning. In this study, the band edge energies of different sized PbS QD monolayers with different cross-linkers on Au substrates were measured using ultraviolet photoelectron spectroscopy and electrochemistry. On Au films, the measured VBM was found to be insensitive to changes in the QD size or cross-linker. After insertion of a thin film of alumina in between the PbS quantum dot monolayer film and the Au substrate, the measured valence band position revealed a shift as a function of ligand and QD size. These results identify a general method to eliminate Fermi level pinning in QDs and an approach to predictably control the energetics at the QD- metal interfaces beneficial for improving the performance of QD based solar cells.

1.4 REFERENCES

- (1)Ebbesen, T. W.; Lezec, H. J.; Ghaemi, H. F.; Thio, T.; Wolff, P. A. Extraordinary optical transmission through sub-wavelength hole arrays. *Nature* **1998**, *391*, 667-669.
- (2)Willetts, K. A.; Van Duyne, R. P. Localized Surface Plasmon Resonance Spectroscopy and Sensing. *Annual Review of Physical Chemistry* **2007**, *58*, 267-297.

- (3) Stewart, M. E.; Anderton, C. R.; Thompson, L. B.; Maria, J.; Gray, S. K.; Rogers, J. A.; Nuzzo, R. G. Nanostructured Plasmonic Sensors. *Chemical Reviews* **2008**, *108*, 494-521.
- (4) Homola, J. Surface Plasmon Resonance Sensors for Detection of Chemical and Biological Species. *Chemical Reviews* **2008**, *108*, 462-493.
- (5) Anker, J. N.; Hall, W. P.; Lyandres, O.; Shah, N. C.; Zhao, J.; Van Duyne, R. P. Biosensing with plasmonic nanosensors. *Nat Mater* **2008**, *7*, 442-453.
- (6) Yanik, A. A.; Huang, M.; Kamohara, O.; Artar, A.; Geisbert, T. W.; Connor, J. H.; Altug, H. An Optofluidic Nanoplasmonic Biosensor for Direct Detection of Live Viruses from Biological Media. *Nano Lett* **2010**.
- (7) Barnes, W. L.; Dereux, A.; Ebbesen, T. W. Surface plasmon subwavelength optics. *Nature* **2003**, *424*, 824-830.
- (8) Maier, S. A.: *Plasmonics : fundamentals and applications*; Springer: New York, 2007.
- (9) Zhang, J.; Zhang, L.; Xu, W. Surface plasmon polaritons: physics and applications. *Journal of Physics D: Applied Physics* **2012**, *45*, 113001-113019.
- (10) Hutter, E.; Fendler, J. H. Exploitation of Localized Surface Plasmon Resonance. *Advanced Materials* **2004**, *16*, 1685-1706.
- (11) Brongersma, M. L.; Hartman, J. W.; Atwater, H. A. Electromagnetic energy transfer and switching in nanoparticle chain arrays below the diffraction limit. *Physical Review B* **2000**, *62*, 16356-16359.
- (12) Lamprecht, B.; Schider, G.; Lechner, R. T.; Ditlbacher, H.; Krenn, J. R.; Leitner, A.; Aussenegg, F. R. Metal nanoparticle gratings: influence of dipolar particle interaction on the plasmon resonance. *Phys Rev Lett* **2000**, *84*, 4721-4724.
- (13) Pinchuk, A. O.; Schatz, G. C. Nanoparticle optical properties: Far- and near-field electrodynamic coupling in a chain of silver spherical nanoparticles. *Materials Science and Engineering: B* **2008**, *149*, 251-258.
- (14) Haes, A.; Duyne, R. A unified view of propagating and localized surface plasmon resonance biosensors. *Anal Bioanal Chem* **2004**, *379*, 920-930.
- (15) Wise, F. W. Lead Salt Quantum Dots: the Limit of Strong Quantum Confinement. *Accounts of Chemical Research* **2000**, *33*, 773-780.
- (16) Hogg, R. A.; Zhang, Z.: Quantum Dot Technologies. In *The Physics and Engineering of Compact Quantum Dot-based Lasers for Biophotonics*; Wiley-VCH Verlag GmbH & Co. KGaA, 2014; pp 7-42.

- (17) Resch-Genger, U.; Grabolle, M.; Cavaliere-Jaricot, S.; Nitschke, R.; Nann, T. Quantum dots versus organic dyes as fluorescent labels. *Nat Meth* **2008**, *5*, 763-775.
- (18) Brus, L. E. Electron–electron and electron-hole interactions in small semiconductor crystallites: The size dependence of the lowest excited electronic state. *The Journal of Chemical Physics* **1984**, *80*, 4403-4409.
- (19) M G Bawendi; M L Steigerwald, a.; Brus, L. E. The Quantum Mechanics of Larger Semiconductor Clusters ("Quantum Dots"). *Annual Review of Physical Chemistry* **1990**, *41*, 477-496.
- (20) Jasieniak, J.; Califano, M.; Watkins, S. E. Size-Dependent Valence and Conduction Band-Edge Energies of Semiconductor Nanocrystals. *ACS Nano* **2011**, *5*, 5888-5902.
- (21) Hyun, B.-R.; Zhong, Y.-W.; Bartnik, A. C.; Sun, L.; Abruña, H. D.; Wise, F. W.; Goodreau, J. D.; Matthews, J. R.; Leslie, T. M.; Borrelli, N. F. Electron Injection from Colloidal PbS Quantum Dots into Titanium Dioxide Nanoparticles. *ACS Nano* **2008**, *2*, 2206-2212.
- (22) Brown, P. R.; Kim, D.; Lunt, R. R.; Zhao, N.; Bawendi, M. G.; Grossman, J. C.; Bulović, V. Energy Level Modification in Lead Sulfide Quantum Dot Thin Films through Ligand Exchange. *ACS Nano* **2014**, *8*, 5863-5872.
- (23) Ellingson, R. J.; Beard, M. C.; Johnson, J. C.; Yu, P.; Micic, O. I.; Nozik, A. J.; Shabaev, A.; Efros, A. L. Highly Efficient Multiple Exciton Generation in Colloidal PbSe and PbS Quantum Dots. *Nano Letters* **2005**, *5*, 865-871.
- (24) Zohar, G.; Baer, R.; Rabani, E. Multiexciton Generation in IV–VI Nanocrystals: The Role of Carrier Effective Mass, Band Mixing, and Phonon Emission. *The Journal of Physical Chemistry Letters* **2013**, *4*, 317-322.
- (25) Yang, Y.; Rodríguez-Córdoba, W.; Lian, T. Multiple Exciton Generation and Dissociation in PbS Quantum Dot-Electron Acceptor Complexes. *Nano Letters* **2012**, *12*, 4235-4241.
- (26) Brown, G. F.; Wu, J. Third generation photovoltaics. *Laser & Photonics Reviews* **2009**, *3*, 394-405.
- (27) Nozik, A. J.; Beard, M. C.; Luther, J. M.; Law, M.; Ellingson, R. J.; Johnson, J. C. Semiconductor Quantum Dots and Quantum Dot Arrays and Applications of Multiple Exciton Generation to Third-Generation Photovoltaic Solar Cells. *Chemical Reviews* **2010**, *110*, 6873-6890.
- (28) Sze, S. M.; Ng, K. K.: *Physics of semiconductor devices*; Wiley-Interscience: Hoboken, N.J., 2007.
- (29) Carey, G. H.; Abdelhady, A. L.; Ning, Z.; Thon, S. M.; Bakr, O. M.; Sargent, E. H. Colloidal Quantum Dot Solar Cells. *Chemical Reviews* **2015**, *115*, 12732-12763.

(30) Pattantyus-Abraham, A. G.; Kramer, I. J.; Barkhouse, A. R.; Wang, X.; Konstantatos, G.; Debnath, R.; Levina, L.; Raabe, I.; Nazeeruddin, M. K.; Grätzel, M.; Sargent, E. H. Depleted-Heterojunction Colloidal Quantum Dot Solar Cells. *ACS Nano* **2010**, *4*, 3374-3380.

2.0 AN IN-PLANE NANOFLUIDIC NANOPLASMONIC-BASED PLATFORM FOR BIODETECTION

This chapter has been partially published in “Zeng, Z.; Mendis, M. N.; Waldeck, D. H.; Wei, J. A semi-analytical decomposition analysis of surface plasmon generation and the optimal nanoledge plasmonic device. *RSC Advances* 2016, 6, 17196-17203.” and “Jianjun Wei, Matthew Kofke, Madu Mendis, Honjun Song, Sameer Singhal and David Waldeck, “An In-Plane Nanofluidic Nanoplasmonic-Based Platform for Biodetection”, Proceedings for the ASME 2012 3rd Micro/Nanoscale Heat & Mass Transfer International Conference, MNHMT2012, March 3-6, 2012, Atlanta, Georgia, USA.”. The thesis author conducted the fabrication, optical characterization, theoretical calculations and biosensing studies of the nanoplasmonic-nanofluidic device which is discussed.

This work reports a new nanofluidic plasmonics-based sensing platform which can be readily integrated with microfluidics devices, and potentially enable an in-parallel transmission surface plasmon resonance (SPR), lab-on-chip sensing technology. The technology overcomes the current SPR size limitations through a combination of nanofluidics and nanoplasmonics in a rationally designed in-plane nanoslit array capable of concurrent plasmonic sensing and confined-flow for analyte delivery. The work presented here includes an integrated device with nanofluidic nanoplasmonic arrays interfacing with microfluidic channels, and preliminary findings, from both theoretical and experimental fronts, of the device for bio-sensing.

2.1 INTRODUCTION

Microfluidics is an emerging technology and continues to dramatically enhance healthcare by providing effective and convenient lab-on-chip tools for a wide spectrum of biomedical applications, in particular the areas of medical diagnostics and therapeutics. Microfluidic chip-based devices provide various unique advantages, including small sample volumes (nano- to micro-liters), fast reaction times (seconds to minutes), high throughput (parallel arrangements, manifolded), salient portability, and automated handling (sample processing, mixing, reaction and detection stages). In addition, microfluidic structures can be mass-produced at low unit cost, making them truly disposable. These features render microfluidic devices an excellent candidate for the routine monitoring of public health.

While microfluidics has experienced tremendous growth and strongly impacted biomedical research over the past two decades, it remains limited by compatible analysis/detection platforms. In parallel surface plasmon resonance (SPR) methods have shown great flexibility and robustness for detection. Specifically, nanostructured metal films that act as plasmonic sensing elements provide the fundamental technology for a new generation of SPR based assays that are emerging and are compatible with microfluidic platforms and/or highly parallel throughput studies.

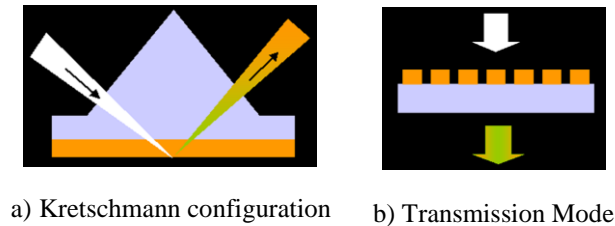


Figure 2.1 Two typical SPR configurations

Surface plasmons (SPs) are very sensitive to the near surface dielectric constant (index of refraction) and are well-suited to the detection of surface binding events. Hence they have been exploited extensively in a variety of SPR-based sensors, particularly biosensors.¹ The most common methodology of SPR sensing is based on the Kretschmann configuration (Figure 2.1 (a)) where a prism is used for the light-SP coupling at the surface of a thin metal film. The probe light undergoes total internal reflection on the inner surface of the prism. At a defined SPR angle, an evanescent light field travels through the thin gold film and excites SPs at the metal-dielectric interface, reducing the intensity of the reflected light. The intensities of scattered and transmitted light fields are used to determine the thickness and/or dielectric constant of the coating.² The control variables for SPR sensor applications, i.e., the wavelength of incident light, the thickness of the metal film, the physical and optical properties of the prism, and the index of refraction of the medium near the metallic interface, have been well studied.³ However, the advantages of averaging over a large surface area and challenges of miniaturizing the optics limit the integration of SPR-based sensing with microfluidics.⁴

Nanoplasmonics, nano-optical phenomena that are caused by resonant surface plasmons localized in nanosystems, has current and prospective applications in near-field

scanning microscopy with chemical resolution, detection of chemical and biological agents with single molecule sensitivity, nano-modification, nanolithography etc. Since Ebbesen et al.⁵ demonstrated that an array of subwavelength holes transmits more light than predicted by classical diffraction theory⁶ and correlated the extraordinary optical transmission (EOT) to the resonant excitation of surface plasmons that arise from the periodic nature of the arrays,⁷ nanoscale metal structures have generated considerable interest. On a fundamental level this discovery has sparked interest in the basic process underlying the ability of a nanoaperture to tunnel light with high efficiency and the physics of surface plasmons. On an applied level this work has encouraged researchers to explore the potential for creating nanoscale sensors,⁸ and other devices from such arrays. Transmission mode SPR (Figure 2.1 (b)) that is tailored via nanometer scale structures⁹ could enable new plasmonic lab-on-chip technologies in bio/chemical sensing. The plasmonic interaction in bio/chemically functionalized nanostructure arrays offers a new strategy for massively parallel detection of chemical and biological agents that bind to functionalized surfaces. Modulation of the nanoaperture array's optical response by adsorbed analytes is expected to offer improved sensitivity and selectivity over conventional SPR methods. In addition, by avoiding use of bulky optics and high-precision mechanics for angular or wavelength interrogation of metal films in contact with analytes,¹⁰ it should be possible to implement and automate the transmission SPR based sensor in compact instrumentation

The unique optical properties of nanostructured arrays in transmission surface plasmon resonance (T-SPR) motivates further their application to surface based chemical and biological detection. Basically, the adsorption of the analyte will cause a change in the dielectric ambient near the metal surface, which causes a shift of the SPR peak in the transmission spectrum of

normal incidence light. The grating based SPR system has a reduced sensitivity compared to the conventional Kretschmann configuration, however, the sensitivity of the transmission spectrum's peak shift was found to be 400 nm per refractive index unit (400 nm/RIU).¹¹ Gordon et.al. demonstrated nanohole arrays as sensing elements capable of both chemical sensing and biomolecule adsorption monitoring.¹² Recently, an integrated microfluidics based nanohole array chip device was developed for biomolecule adsorption detection in transmission SPR with 500 nm/RIU.¹³ Recently, Brolo et. al. showed that nanohole arrays, in which only the walls of the hole are accessible to analyte is sensitive to attomole quantities of protein.¹⁴ Nevertheless, enhancement of the sensitivity and the design of structures that integrate well with microfluidics remains a significant challenge.

In this study, by using micro-channels etched into the substrate as opposed to PDMS microfluidic channels the alignment of the microfluidics to the nanofluidics is simplified and the pressure tolerance is greatly increased. The metal nanoslit array acts as a bundle of nanochannels connecting the two microchannels and liquid can flow-through from one end to the other of the two microchannels, interfacing two microchannels through the nanoslit array. Computational fluidic dynamics (CFD) modeling of the nanoslit array have verified the nano-confined flow through. Meanwhile, the metal film nanoslit array is used as a transmission mode SPR biosensor due to its extraordinary optical transmission. Finite-difference time-domain (FDTD) simulation studies have shown that a nanoledged array device could provide a well-defined transmission resonance and a large red shift of the primary transmission peak was observed by changing the refractive index, suggesting the promise of using this nanofluidic nanoplasmonics-based platform for biodetection.

2.2 EXPERIMENTAL

2.2.1 Fabrication of Nano-plasmonic Nano-fluidic Device

2.2.1.1 Focused Ion Beam Fabrication of the Nanoledge Structures

Quartz slides ($25 \times 25 \text{ mm}^2$) were used as the substrate for sample preparation. These were rinsed first with acetone in an ultrasonic bath for 10 min, and then rinsed with deionized water and dried under a nitrogen stream. Then the slides were placed on a hot plate with the temperature set at $180 \text{ }^\circ\text{C}$ to remove any traces of water remaining. These slides were exposed to an oxygen plasma for 300 s at a pressure of 200 mTorr to remove organic contaminants on the surface. A 250 nm thin layer of gold (99.95%, Alfa Aesar, USA) was evaporated onto the cleaned quartz slides at around 2.0×10^{-6} Torr, at a deposition rate of 0.2 nm s^{-1} in an electron beam evaporator. A 2.5 nm layer of titanium was deposited before the gold to promote adhesion to the substrate. These gold films were stored under nitrogen in sealed vials prior to FIB milling. The fabrication of the nanoledge structure was done using a dual-beam focused ion beam system (Seiko Instruments SMI3050SE). The focused ion beam column was equipped with a Ga^+ source and operated at 30 keV under a 5 pA beam current. The nanoledge structure measured $\sim 50 \text{ nm}$ wide in the Au-Quartz interface and $\sim 250 \text{ nm}$ wide in the Au-air interface, with a slit length of $20 \text{ }\mu\text{m}$. A vector scan with different line densities were used to introduce different etching depths into the Au film to obtain different widths in the two interfaces. The total area of the array was maintained to be $20 \times 20 \text{ }\mu\text{m}^2$.



Figure 2.2 Schematic of FIB milling routine employed for fabricating the nanoledge structure. a) Cleaning the substrates; b) Thin metal film deposition; and c) FIB milling of the targeted nanoledge structure.

2.2.1.2 Electron Beam Lithography Fabrication of the Nanoledge Structures

Electron beam lithography (EBL, Raith e-Line) was used for the fabrication of Au nanoledge structures in arrays ($30 \times 30 \mu\text{m}^2$). Three consecutive EBL steps were followed to achieve the final structure as described below. The fabrication scheme is illustrated in Figure 2.3.

Conductive indium tin oxide coated glass slides (ITO) (Delta's Technologies) were used as the substrates to minimize charging during the fabrication. ITO substrates were rinsed using three solvents: acetone, methanol and iso-propanol; ultrasonication was done in each solvent for 5 min. The ITO substrates were rinsed with DI water and dried with a Nitrogen stream. These substrates were baked at 180°C for 2 min to remove any moisture from the surface. In step one, as illustrated by Fig 2.3 (a), poly-methyl-methacrylate (950 A4 PMMA, Microchem) was spun on the substrate at a speed of 1500 rpm for 40 s using a spin processor (Laurell *WS-400-6NPP-LITE*) and baked on a hot plate at 180°C for 5 min. EBL was performed at an acceleration voltage of 20 keV and with an exposure dose of $300 \mu\text{C}/\text{cm}^3$ using a $7.5 \mu\text{m}$ aperture to write the markers on PMMA, in order to define the coordination system on the substrate which will act as the reference on the subsequent steps. The sample was then developed for 90 s in a developing solvent consisting of methyl isobutyl ketone and isopropanol in a 3:1 ratio to dissolve the exposed PMMA. The silver

(Ag) was evaporated onto this sample to a thickness of 50 nm, with an undercoat of 5 nm of titanium to help the Ag better adhere to the substrate. The rate of evaporation was maintained at 0.3 \AA s^{-1} to allow smooth deposition of the metal. After the metal deposition, the samples were kept overnight in acetone to remove the remaining PMMA resist.

In the step 2 (Fig 2.3 (b)), the substrates with the coordinates obtained from step one were taken and rinsed with acetone, methanol, iso-propanol: 3 minutes in each solvent, in order to remove any dirt particles on the substrate. The substrates were then dried with a Nitrogen stream and baked at $90 \text{ }^{\circ}\text{C}$ for 4 min to remove any moisture from the surface. Negative e-beam resist (maN 2403, Micro Resist Technologies) was spun on the substrates at a speed of 3000 rpm for 30 s using the spin processor to obtain a final film thickness of 300 nm. The resist-coated substrates were baked for 60 s on a hot plate at $90 \text{ }^{\circ}\text{C}$. Next the resist –coated substrates were placed under the EBL system to make the 80 nm width nano-slits. Electron beam exposure was performed at an acceleration voltage of 20 keV using the $7.5 \text{ }\mu\text{m}$ with an exposure dose of $100 \text{ }\mu\text{C}/\text{cm}^2$. The samples were developed using an alkaline developing solution (CD-26, MicroChem) for 90 s to dissolve the unexposed resist. Gold (Au) was evaporated onto the sample at a thickness of 50 nm, with a 5 nm Ti underlayer to promote adhesion. After the metal deposition, the remaining resist was removed by soaking in Remover PG 1165 at $90 \text{ }^{\circ}\text{C}$ for about 60 min followed by 5 min of sonication.

In step three (Fig 2.3 (c)), the samples prepared in step 2 were taken and cleaned as previously described. The negative e-beam resist was spin coated as before with the same conditions and baked for 1 min on a hot plate at $90 \text{ }^{\circ}\text{C}$. The samples were again placed under the EBL system and exposure parameters like those in step two were used. With the help of the pre-defined coordinates the second nanoslit were overlaid right on the 80 nm nanoslit array. After the

exposure, the sample was developed using CD-26 developer (MicroChem). Gold was deposited to a thickness of 150 nm. Lift-off of the remaining resist was performed as in step 2, in order to obtain the final nanoledge structure.

2.2.2 Finite Difference Time Domain Calculations

Theoretical modeling and design of the SPP based nanoledge sensor was performed using a commercial software implementation (Lumerical Solutions Inc.) of the finite differential time domain method (FDTD). The geometry of the nanoledge slit structure was modeled in the software in a two-dimensional (2D) environment as illustrated in Figure 2.4. A 2D simulation was chosen to be an adequate approximation since the length of the uniform 20 μm slits in the x -direction is much larger than the light wavelengths of interest. The dielectric function of Au used in the simulations was extracted from Johnson and Christy data¹⁵, which were available in the FDTD software. The substrate was simulated as an infinite block with a dielectric constant of silicon dioxide taken from Palik¹⁶. The simulations were conducted using a single aperture as the unit cell with periodic boundary conditions in the y -direction to describe an infinite rectangular array and perfectly matched layers on the boundary along the z -direction. As with the experiments, a TM-polarized broadband plane wave source was placed inside the glass substrate and incident on the back surface of the gold layer at normal incidence as shown in Figure 2.4.

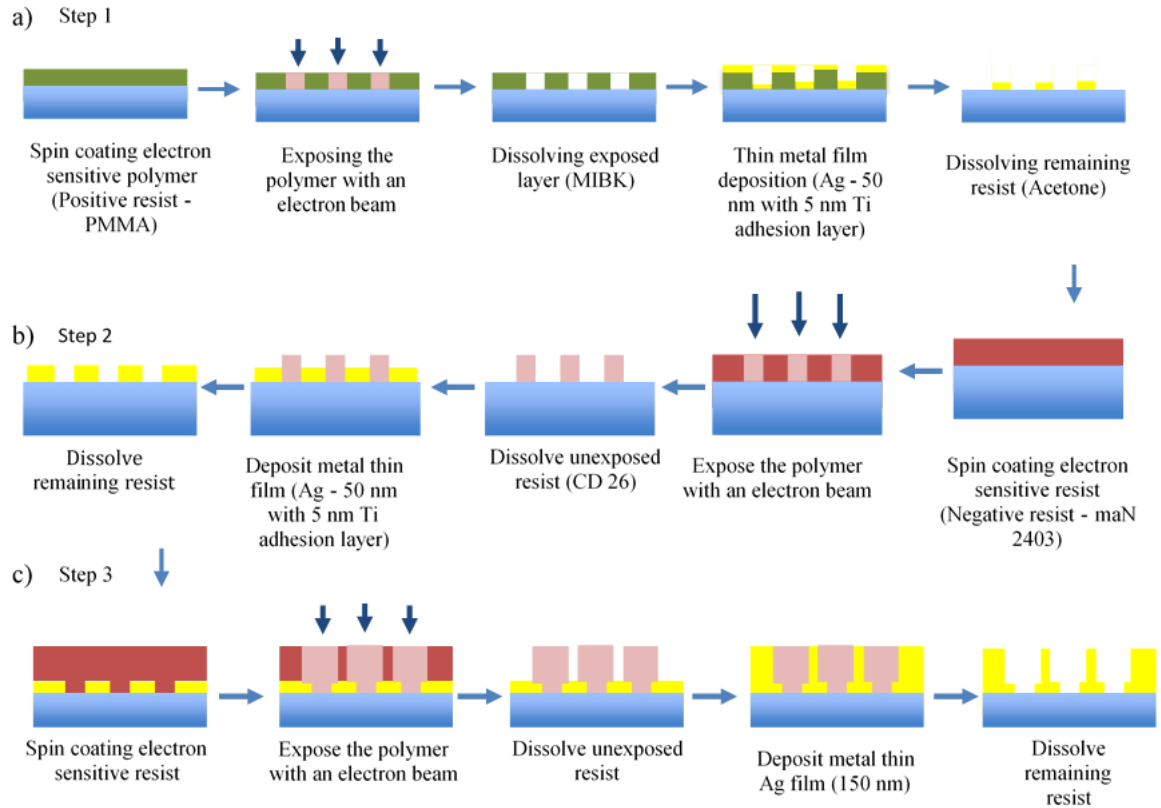


Figure 2.3 Schematic of steps followed in fabricating the nanoledge structures using Electron Beam Lithography. a) Step 1 - Fabrication of alignment markers on the substrate b) Step 2 - Fabrication of 50 nm width slits using negative e-beam resist c) Step 3 – Alignment and fabrication of the 250 nm width slit on top of the bottom 50 nm slit to obtain the intended nanoledge structure.

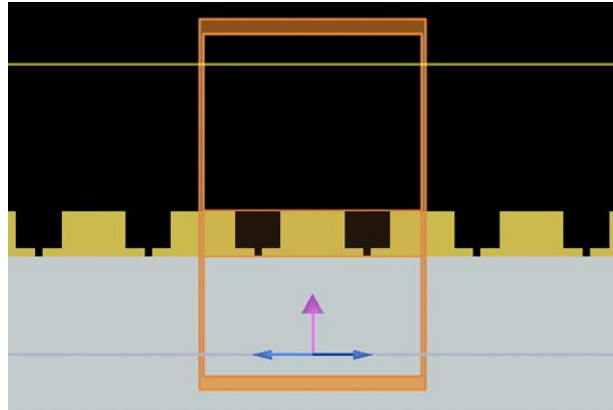


Figure 2.4 The yz view of 2-D simulation setup used for the calculations on nanoedge structures. The orange box defines the simulation area. The pale white area at the bottom represents the quartz substrate whereas the Au film is represented in yellow. The bottom arrow represents the plane light source injecting light along the y direction whereas light is polarized along the x direction.

2.2.3 Modeling of Confined Flow-through Nanoslit

Figure 2.5 shows the physical model of the simulated device, which consists of two microchannels with a width of $600\ \mu\text{m}$ and a height of $20\ \mu\text{m}$. These two microchannels are connected through an array of nanochannel structures. The length and the width of the nanochannel structure array is $30\ \mu\text{m}$ and $20\ \mu\text{m}$ respectively (see the enlarged graph at the left bottom of Figure 2.5). The nanochannel array contains 33 single nanochannels, the width and height of the nanochannel is $250\ \text{nm}$ and $200\ \text{nm}$ respectively. The gap between the nanochannels is $350\ \text{nm}$. In the center of the nanochannel, an additional nano-groove with both width and height of $50\ \text{nm}$ was etched (see the enlarged graph at the right bottom of Figure 4.6). Fluid is injected from the inlet

and follow to the outlet where it exits. The laminar flow in the micro- and nano- channel is governed by the continuity equation and the steady state Navier-Stokes equation:

$$\text{Continuity equation} \quad \nabla \cdot \mathbf{v} = 0$$

Equation 2.1

$$\text{Navier-Stokes equation} \quad \rho \mathbf{v} \cdot \nabla \mathbf{v} = -\nabla p + \mu \nabla^2 \mathbf{v}$$

Equation 2.2

Here v , ρ , p and μ is the fluid velocity, density, pressure and viscosity respectively. The governing equations were solved using the commercial finite volume-based simulation software CFD-ACE+ (ESI-CFD, Inc.). The computational domain is meshed by a block-structured grid using the preprocessor available within CFD-ACE+. The CFD-ACE+ solver uses the SIMPLEC algorithm for pressure-velocity coupling.

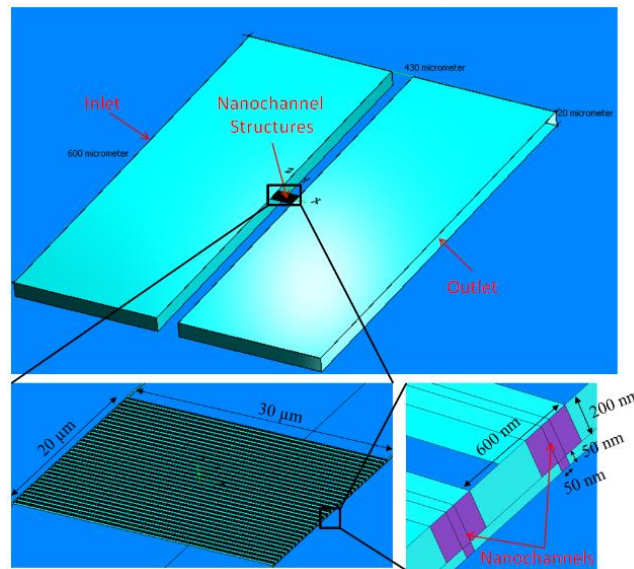


Figure 2.5 Physical model of the simulated device

2.2.4 Measuring the Refractive Index Sensitivity of the Nanoledge Structure

This study was performed using refractive index standards, purchased from Cargills Inc., with indices ranging from 1.300 ± 0.0002 to 1.390 ± 0.0002 . While changing the refractive index of the outside environment of the nanoslit array, the transmission spectrum of the nanoledge device was collected using a Microspectrometer (Craic QDI 2010) equipped with a Xenon light source. A linear polarizer (Glan-Taylor) was used to polarize the light perpendicular to the slits.

2.2.5 Albumin Binding and Detection using Nanoledge Devices

The chip containing the nanoledge devices was cleaned with oxygen plasma for 15 min under 200 mTorr pressures. A 1 to 10 molar ratio solution of hydroxy-terminated tri(ethylene glycol) undecane thiol (Nanoscience Instruments, Inc.) to carboxyl-terminated tri(ethylene glycol) undecane thiol (Nanoscience Instruments, Inc.) was prepared in absolute ethanol. The gold substrate was incubated in this solution overnight with stirring to form the mixed self-assembled monolayer. Then the gold substrate was removed from the thiol solution and rinsed with ethanol for 10 s to stop further self-assembly. After drying it under a Nitrogen stream, the substrate was incubated in a solution of 0.5 mM N-Hydroxysuccinimide (NHS, Sigma Aldrich)/1-ethyl-3-(3-dimethylaminopropyl) carbodiimide (EDC, Sigma Aldrich) in 10 mM, pH 7 phosphate buffer (PBS) with stirring for 2 hours. A $10 \mu\text{g}/\text{cm}^{-3}$ solution of anti-bovine serum albumin (Monoclonal, Sigma Aldrich) was prepared in PBS. The activated substrate was taken and rinsed with PBS buffer. Then it was immediately incubated in an anti-Albumin antibody solution for 4 hours with stirring. To deactivate the ester group formed during EDC/NHS activation, the substrate was incubated in 0.2 M glycine (Sigma Aldrich,) in PBS. After the substrate was rinsed with PBS and

deionized (DI) water, it was dried under Nitrogen. Antibody modified slides were incubated with different Albumin concentrations ranging from 1 pg/ml to 1 mg/ml. After each incubation step, the transmission spectra of the nanoledge device were collected in PBS buffer or in air after drying the slides under a Nitrogen stream.

2.2.6 Prostate Specific Antigen (PSA) Binding and Detection using Nanoledge Devices

The gold coated chips were first cleaned with O₂ plasma for 15 minutes, followed by a self-assembled monolayer (SAM) process by incubation of the chips in a mixture of 1 mM HSC₁₀COOH (Sigma Aldrich) and HSC₈OH (Sigma Aldrich) with a mole ratio of 1:2 in absolute ethanol solution for overnight. The SAM then was activated by incubation in a pH 7.0, 10 mM phosphate buffer solution containing 0.5 mM of EDC/NHS, respectively for 2 hours. The activated SAM was rinsed with the 10 mM PBS and immediately moved to a freshly prepared 10 mM PBS containing 10 µg/mL of the detector Prostate Specific Antibody (anti-PSA) for 4 hours incubation. The chip was rinsed with PBS and this was followed by dipping it into a 0.2 M glycine PBS solution for 10 minutes in order to deactivate the remaining active sites at the SAM. The nanoplasmonic chips were incubated in 0 -100 pg/ml of PSA for 30 min for analyte binding.

2.3 RESULTS AND DISCUSSION

The basic philosophy of the design of the nanoledge device design is to allow the same sensitivity as a nanoslit device as well as allow better mass transport inside the slit and facilitate its integration into microfluidic (nanofluidic) systems. Microfluidic systems allow the use of small

sample volumes, which is essential when working with biological samples. Even though the sensitivity of the nanoslit arrays increase with decreasing width¹⁷, mass transport inside the slit is inhibited by decreasing slit widths, or cross sections. The nanoledge device contains two slits overlaid on each other to allow better mass transport and to retain larger refractive index sensitivity.

2.3.1 Focused Ion Beam Fabricated Nanoledge Structures

A schematic cross section of single nanoledge slit is illustrated in Figure 2.6 (a) giving all the physical dimensions. Figure 2.6 (b) shows an SEM image of a FIB fabricated nanoledge array of 1000 nm periodicity taken at a 55° angle. The width of the top slit was estimated to be 246 nm and width of the bottom slit was estimated to be around 54 nm.

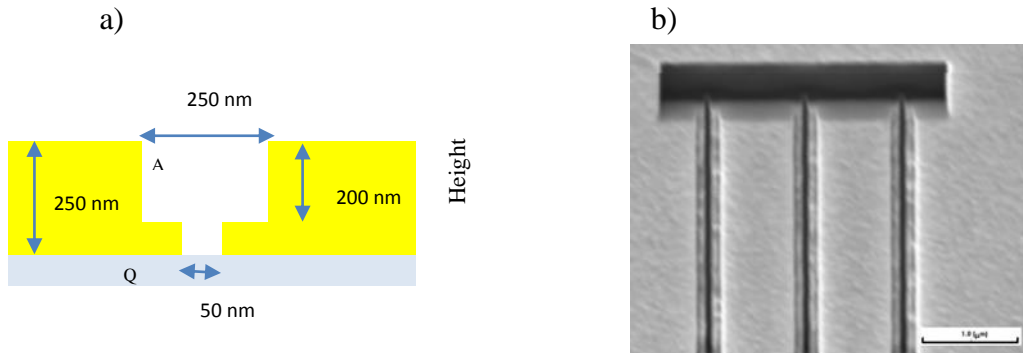


Figure 2.6 a) Schematic and b) SEM image of the nanoledge device.

2.3.1.1 Optical Characterization

The transmission spectrum collected in air for a FIB fabricated nanoledge array with a periodicity of 600 nm is shown in Figure 2.7. Several transmission peaks can be observed in the spectrum with different intensities. To distinguish the periodicity dependent peaks, which correspond to resonant excitation of SPPs on the two interfaces, from resonances that originate from excitation inside the slit, we carried out experiments in which the periodicity of the slits was changed from 500 nm to 850 nm in 50 nm intervals. The effect of periodicity on the SPPs excited on two dimensional nanohole arrays have been studied previously where they have observed the red shifting of these peaks as the periodicity increases.¹⁸ It could be observed from Figure 2.7 (b) that the ‘peak A’ does not change its position much with the increasing periodicity whereas peaks B, C and D shift to higher wavelengths as the period of the array increases. The same trend is also observed in FDTD calculations, as illustrated in Figure 2.7 (c). It can be noted that FDTD calculations predict sharper features in the transmission spectrum as compared to what is experimentally achieved. Broadening of the peaks in the experimental transmission spectrum may arise from the merging of sharp features, which can be observed in the calculated spectrum, and could arise from imperfections. In order to further account for these imperfections, FDTD calculations were performed with realistic dimensions taken from the AFM study (Figure 2.8 (a)) which resulted in a spectral profile which better resembled that obtained in experiment (Figure 2.8 (b)).

Using Equation 1.7 and taking the dielectric constant of air to be 1 and the dielectric constant of quartz to be 2.32, the SPP excited at the Au-air and Au-quartz interfaces is predicted to occur at around 639 nm and 950 nm, respectively for a nanoledge array of 600 nm. Peaks B and

D are near these values, so we assign these two peaks to resonance excitation of an SPP on the metal-air interface and one on the metal-substrate interface. As illustrated in Figure 2.8(b), the FDTD calculations with and without the quartz substrate shows that the peak around 900 nm disappears when the quartz substrate is removed which agrees with the peak assignment.

2.3.1.2 Refractive Index Sensitivity

The refractive index sensitivity of the nanoledge device with a 600 nm periodicity was found to be 545 nm per RIU and a figure of merit was calculated to be 20 RIU⁻¹. As depicted in Figure 2.9, the position and width of dip C was used for the above calculations. The smaller FWHM of the dip C gives a very high figure of merit compared to other nanoslit type devices.¹⁹ The refractive index sensitivity of nanoledge arrays are in the same range when compared with nanoslit arrays with the same periodicity.¹⁷ Given the wavelength resolution of the spectrometer, which is 0.782 nm in the visible range and 6.684 nm in the near IR range, the detection limit of the nanoledge device with 600 nm periodicity is $\sim 1.44 \times 10^{-3}$ RIU in the visible range and 1.22×10^{-2} RIU in the near infra-red (IR) region of the electromagnetic spectrum. By way of comparison, the sensitivity of traditional SPR, has been reported to lie in the range of 10^{-6} - 10^{-7} RIU. Improving the wavelength resolution on the spectrometer may enhance the detection limit of the nanoledge structures. The change in the wavelength of peak A and B as the refractive index of the medium changes are plotted in Figure 2.9 (b). The refractive index sensitivity of the peak maxima were calculated to be 398 nm/RIU for peak A and 522 nm/RIU for peak B respectively.

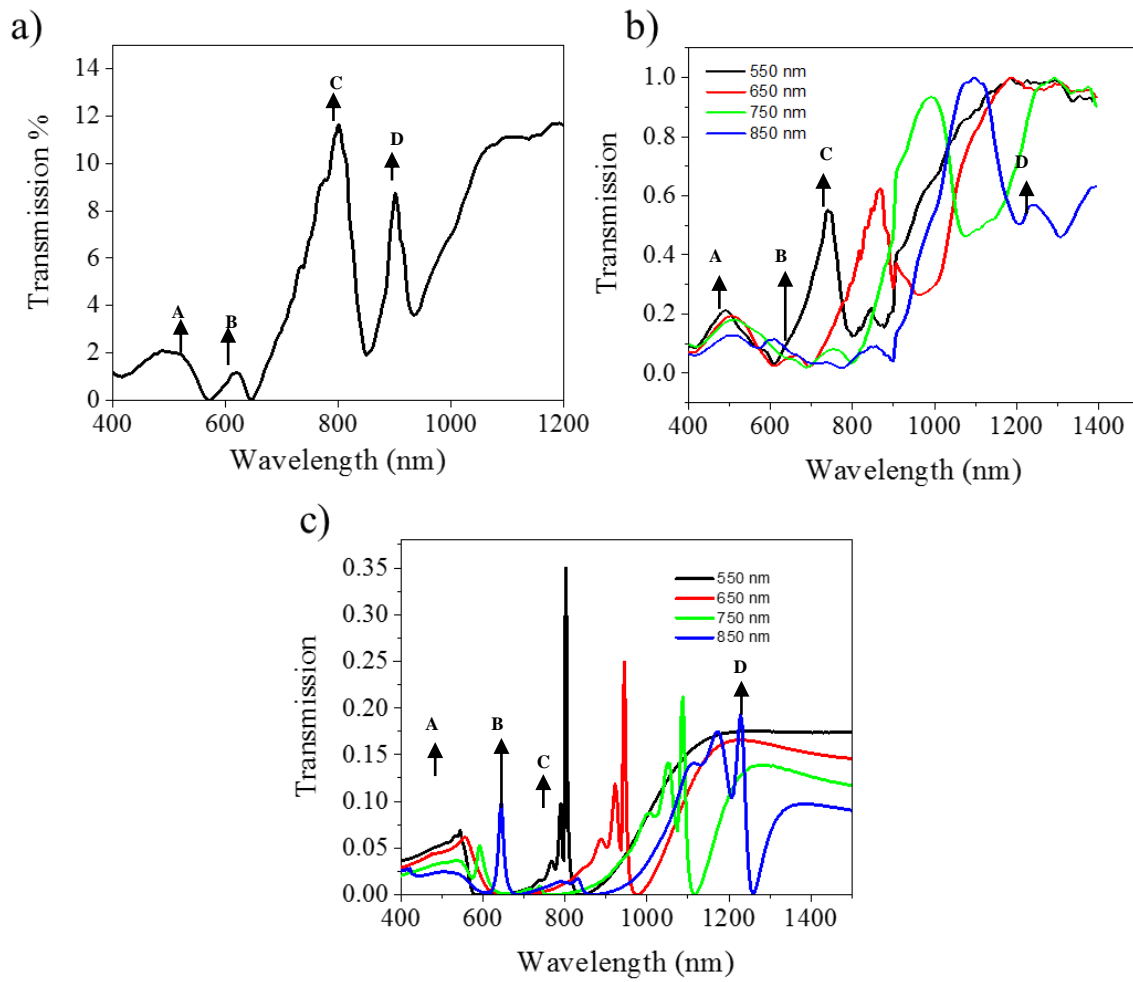


Figure 2.7 a) Transmission spectrum of a nanoledge device of a 600 nm periodicity collected in air. Periodicity dependence of the nanoledge devices studied through b) experimentally obtained c) FDTD calculated transmission spectra of the nanoledge devices

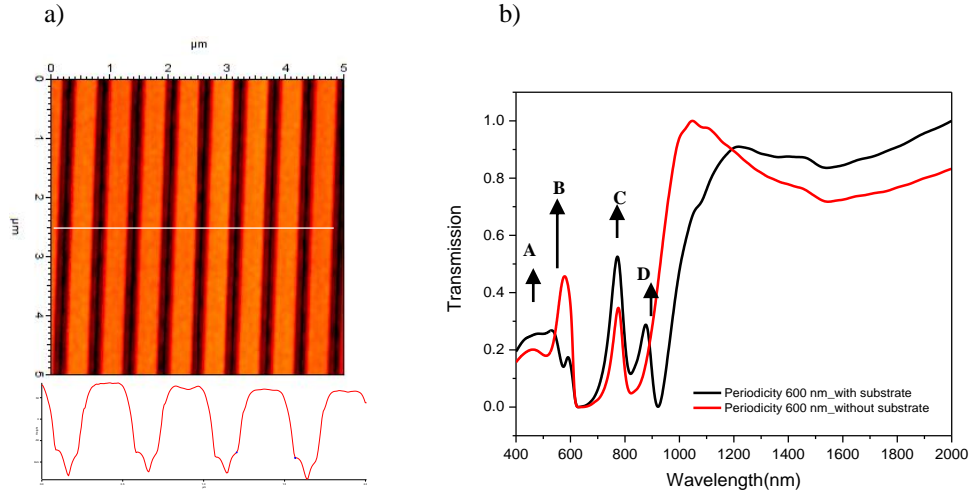


Figure 2.8 The AFM image of the nanoledge structure with a cross along the white line is depicted in (a). In (b) is the FDTD calculated transmission spectra of 600 nm nanoledge structure, with and without the quartz substrate, performed using the slit dimension obtained from (a). Both the spectra were calculated with a background dielectric constant of one. When the quartz substrate is absent it can be noted that peak D disappears from the transmission spectrum

The periodicity of the nanoledge arrays also affects the refractive index sensitivity of the device. In Figure 2.10 we analyze how the refractive index response depends on the period of these arrays. Figure 2.10 (a) plots the resonance wavelength of the dip C of FDTD calculated spectra of these devices while changing the refractive index of the surroundings under different periodicities. In panel 2.10 (b) we plot the resonance wavelength of dip C of the FIB fabricated arrays with different periodicities while changing the refractive index of the outside medium. The slope of each line in this plot gives a refractive index sensitivity of the nanoledge arrays at the specified periodicity and the values seem to match what is predicted by calculations, which can be obtained from Figure 2.10 (a). The refractive index sensitivity of the FIB fabricated devices as a function of periodicity is plotted in part 2.10 (c). The linear fit of this plot exhibits the direct dependence of

RI sensitivity of this nanoledge array on its periodicity where the refractive index sensitivity of these devices increases with increasing periodicity.

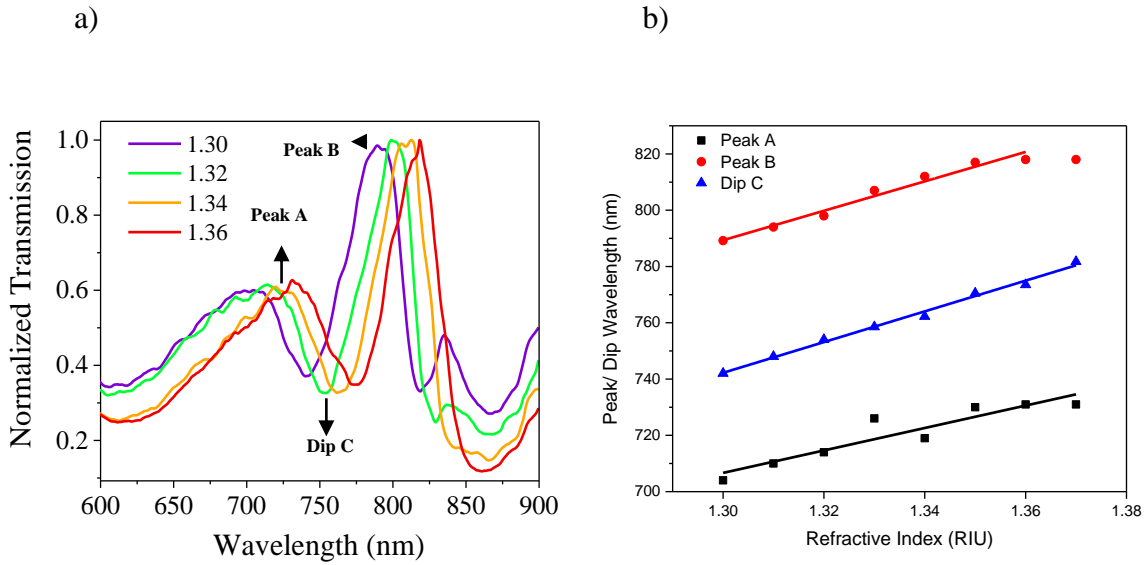


Figure 2.9 a) Transmission spectra of the FIB nanoledge structure, periodicity of 600 nm, with different refractive index standards for normally incident TM polarized light. b) Peak A, B, and dip C wavelengths are plotted against the refractive index of the outside medium. Slope of the fitting curve gives the RIU sensitivity of the device to be 545 nm/RIU from dip C and the figure of merit was calculated to be 20.5 per RIU

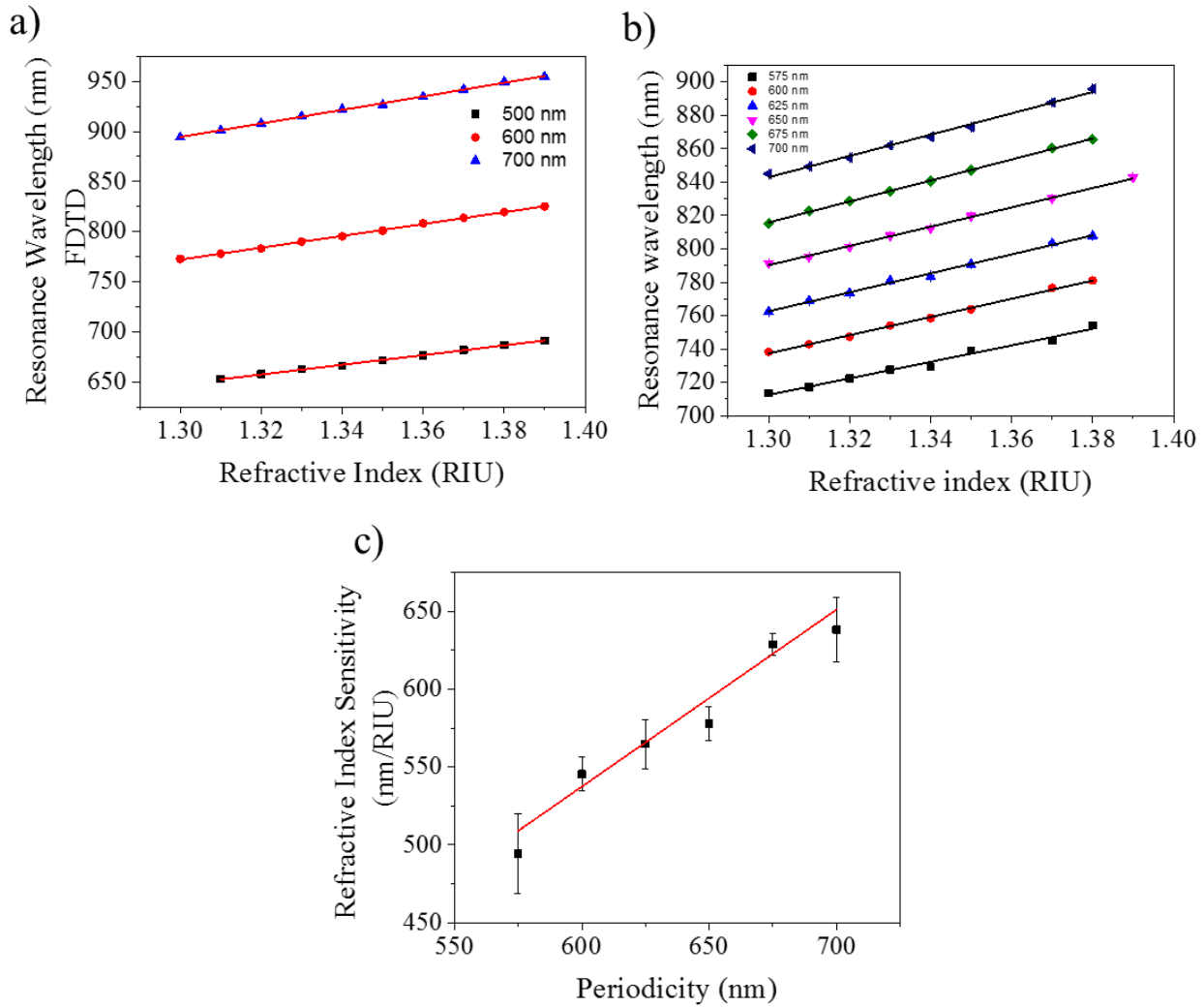


Figure 2.10 The resonance wavelength is plotted against the refractive index of the surrounding environment for different nanoledge periodicity, a) calculated from FDTD method and b) observed for fabricated structures. Panel c) shows how the RI sensitivity of the nanoledge devices depends on the periodicity of the array.

2.3.1.3 Confined Flow-through Nanoslits

Figure 2.11 shows the pressure distribution along the channel for a flow rate of $0.5 \mu\text{L}/\text{min}$ modelled using the CFD-ACE+ (ESI-CFD, Inc.) solver for a 600 nm nanoledge device. We find that most of the pressure is dropped along the nanochannel array (Figure 2.11 (a) and 2.11 (b)). To quantitatively calculate the pressure drop along the nanochannel array, we plotted the pressure distribution along the center (dash line shown in Figure 2.11 (a) in Figure 2.11 (c)). We found that the pressure is nearly the same at all the distances less than the nanochannel inlet (around $7.7 \times 10^7 \text{ N}/\text{m}^2$) and for all distances greater than the positions of the nanochannel outlet (around $0 \text{ N}/\text{m}^2$). The pressure drop along the nanochannel is approximately linear with the length of the nanochannel, yielding a total pressure drop $\Delta P = 7.7 \times 10^7 \text{ N}/\text{m}^2$. Thus very low flow rates are required to maintain fluidic control by pressure driven flow across nanochannels because of these larger pressure drops, a common occurrence in nanofluidic devices.²⁰

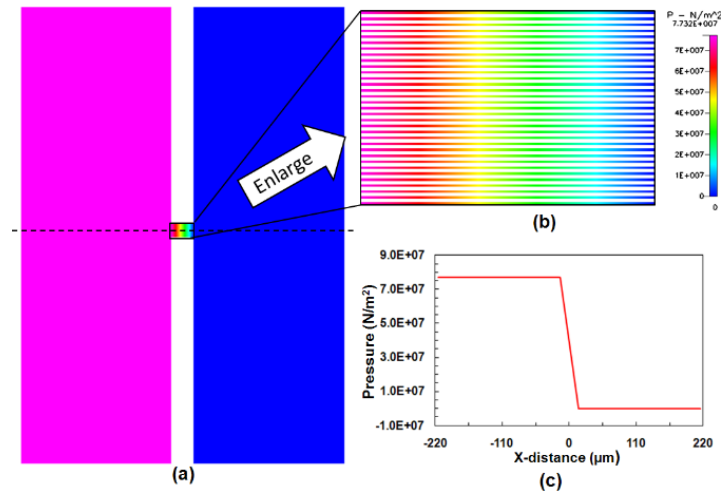


Figure 2.11 Pressure Distribution with the flow rate $0.5 \mu\text{L}/\text{min}$

Since the pressure drop ΔP is directly determined by the injected flow rate Q , the effect of the flow rate Q was also investigated. We ran a series of simulations (Q ranges from $0.1 \mu\text{L}/\text{min}$ to $0.9 \mu\text{L}/\text{min}$) and the relationship between the pressure drop ΔP and the flow rate was plotted in Figure 2.12. We can see the pressure drop increases linearly with the injected flow rate, which can be explained by an analogy to electric circuit theory. Here ΔP and Q is similar to the electric potential and current in the electric circuit respectively, yielding a relationship $R = \Delta P / Q$, where R is the fluidic resistance (analogous to electric resistance). By calculating the slope of the curve, we obtained a fluidic resistance of about $1.55 \times 10^8 \text{ N min}/(\text{m}^2 \mu\text{L})$. For a straight channel with a square cross section the hydraulic resistance can be approximated to $3 \times 10^9 \text{ N min}/(\text{m}^2 \mu\text{L})$ if the width is 250 nm , which is in the same range as the fluidic resistance calculated for the nanoledge array.²¹ This value for hydraulic resistance in a nanoledge array is greater than what is known for microfluidic channels, as the fluidic resistance is known to exponentially increase as the width of the channel decreases.²²

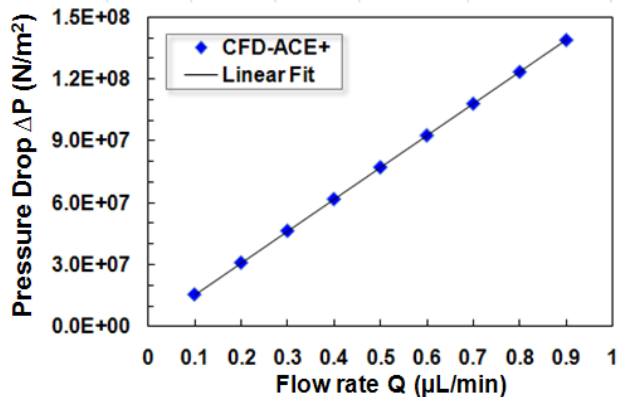


Figure 2.12 Correlation of flow rate and pressure drop

The nanoslit array (30×30 μm) is functioning as a nanofluidic channel that can manipulate sample delivery and enhance efficacy for the detection of analytes to the plasmonic sensing area. The nanochannel area of the device is bi-functional, i.e. nanofluidic control and nanoplasmonic sensing. Hence, the nanochannel and nanoledge technology may potentially be integrated with microfluidic lab-on-chip systems to facilitate a new generation SPR technology for biological detection.

2.3.1.4 Detecting Albumin-antiAlbumin Interaction using FIB Fabricated Nanoledge Structures

Biodetection using nanoledge devices was demonstrated using the albumin binding interaction to the immobilized anti-albumin antibody nanoledge surfaces. Nanoledge devices with a 600 nm periodicity were used for all biosensing experiments. Because of the high affinity of sulfur to Au, the self-assembly of thiols is often used to attach biological molecules onto Au films. Polyethylene glycol (PEG) thiols contain glycol groups in their backbone, which supply a hydrophilic environment when self- assembled.²³ The PEG molecules help to prevent nonspecific adsorption of the proteins and other biological molecules onto the SAM. A mixed SAM helps to control the density of COOH terminal groups on the surface and hence controls the density of the ligand on the surface.²³ The fraction of each thiol on the surface is related to the molar fraction of thiols from which the mixed SAM was formed. This dilution of the protein against the inert background is intended to let it bind in a structurally well-defined manner on the surface and prevent any lateral steric effects, which could block its binding sites. This design is intended to allow better mass transport of analyte proteins onto the binding sites.

Figure 2.13 (a) shows the transmission spectra of the nanoledge devices before and after SAM preparation. As can be observed, a resonance dip occurs around 630 nm and it red shifts about 3 nm when modified with the SAM. A shift of 5 nm was predicted by an FDTD calculation where the SAM was represented by a 5 nm dielectric with a 1.45 RIU over gold. When the same refractive index and characteristic decay length of 288 nm is substituted into Equation 1.12, it predicts a 6 nm shift for the peak A. It can be noted that at this particular wavelength the decay length of SPP is very large compared to the thickness of the SAM, therefore refractive index changes arising from the SAM formation cause only a small change in the effective index felt by the SPP bringing only a small resonance wavelength shift. All predicted shifts are larger than what was experimentally obtained. An ellipsometric study conducted on a 250 nm thick Au film confirmed that a well-packed SAM is obtained under these incubation and self-assembly conditions. A small spectral shift after SAM assembly on the nanoledge devices therefore may arise from Ga implantation²⁴ during fabrication of these devices leading to a substantial increase in the optical loss of the metal as well as poor SAM formation on the device.²⁵

When the anti-Albumin is immobilized onto the SAM, the resonance dip A shifts to shorter wavelengths as illustrated in Figure 2.13 (b). This observation is contrary to what was generally expected to occur when binding occurs, namely, an increase in the dielectric constant should red shift the plasmonic response. Because of the concerns about Ga contamination of the Au surface introduced during the fabrication process, poor adhesion of a SAM on the surface and also high optical loss of the metal could be responsible for the observed anomalous behavior.

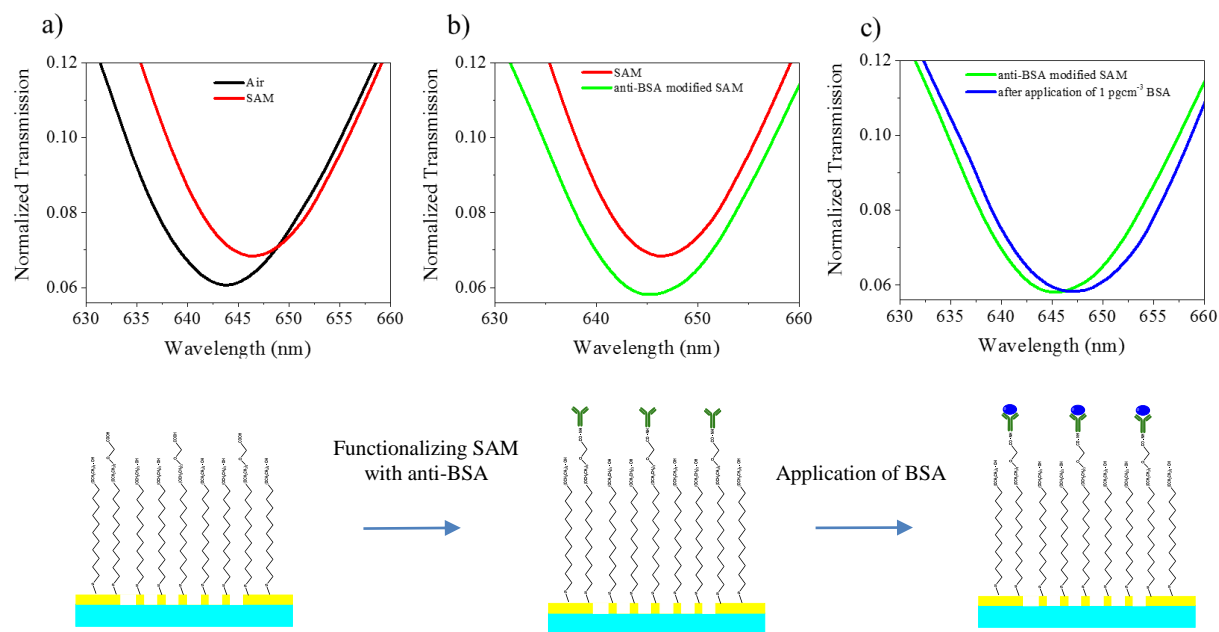


Figure 2.13 Transmission spectra of the nanoledge device a) in air b) after the preparation of mixed monolayer of alkanethiol (COOH/OH) c) when functionalized with anti-BSA d) upon introduction of 1 pg/cm^3 of BSA. All spectra were collected in air.

The resonance wavelength of the device, after exposure to an increasing concentration of BSA collected in buffer and air, is given in Figure 2.14 (a) and Figure 2.14 (b) respectively. As can be observed from the Figures 2.14, the resonant shift is slight and saturates with the increasing BSA concentration. A control experiment was carried out without immobilizing the binding protein anti-BSA, and as Figure 2.15 illustrates no significant shift in the resonance dip with increasing BSA concentration is observed, indicating that there is very little nonspecific binding of BSA. If a well packed SAM was formed on the nanoledge device with an expected ratio of –COOH groups on the surface, using the packing density of PEG thiols on Au surface²⁶, one expects that a maximum of around $7.7 \times 10^{-16} \text{ mol cm}^{-2}$ of anti-BSA can be immobilized on the surface. Using the average length of anti-Albumin (12 nm)²⁷ and the Equation 1.12, we predict a maximum

13 nm red shift for anti-Albumin immobilization on the sensor surface. The smaller observed spectral shift might be caused by the high optical loss of gold and poor SAM preparation from Ga implantation on the device surface during FIB fabrication.²⁵ In order to avoid this problem, a different method of fabrication of the nanoledge structure using EBL was performed. Taking advantage of contaminant-free surfaces produced by this method a better performance of the nanoledge sensor can be expected.

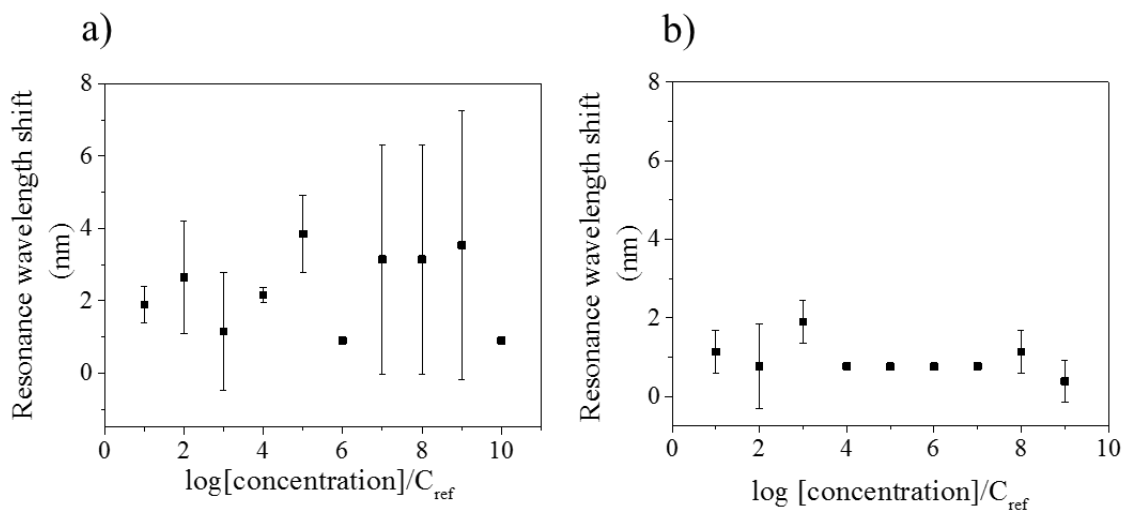


Figure 2.14 Averaged resonance wavelength shift plotted against Albumin concentration measured a) under PBS b) in air. Error bars indicate the standard deviation between resonance shifts in two different trials. $C_{\text{ref}} = 1 \times 10^{-13}$.

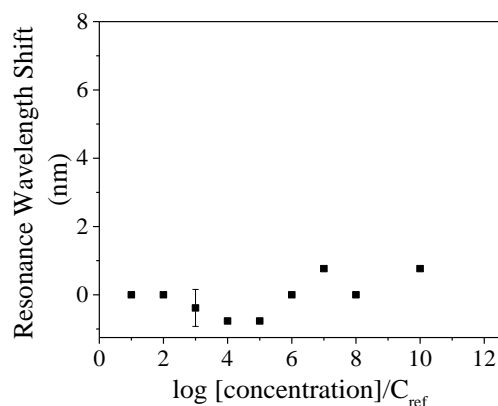


Figure 2.15 The averaged resonance wavelength shift between two control experiments that were carried out without anti-BSA immobilized on the device show no significant shift with increasing Albumin concentration. Error bars indicate the standard deviation between the two trials. $C_{\text{ref}} = 1 \times 10^{-13}$.

2.3.2 Electron Beam Lithography Fabricated Nanoledge Structure

Figure 2.16 illustrates the step wise processes taken to fabricate the nanoledge structure of 600 nm periodicity using electron beam lithography. An SEM image of the alignment markers on the ITO substrate used for the process is illustrated in Figure 2.16 (a) and an SEM image of the bottom nanoslit array before fabrication of the top slit is depicted in Figure 2.16 (b). The alignment markers were then used to align the top wider slit on top of the bottom narrow slit to form the final nanoledge structure shown in Figure 2.16 (c). The width of the bottom slit was measured to be 85 nm and width of the top slit was measured to be 254 nm.

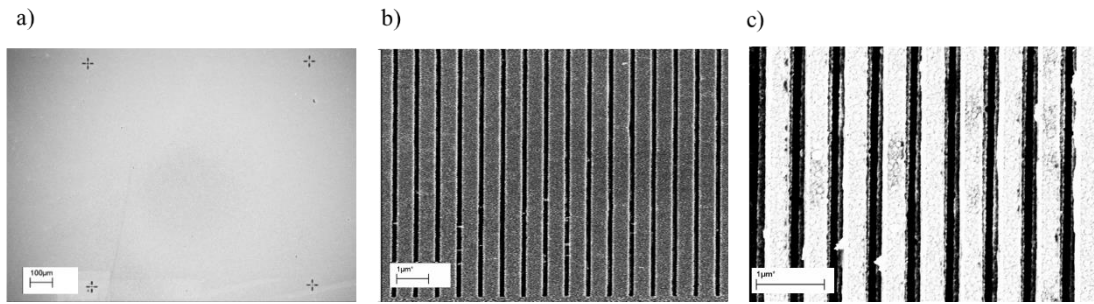


Figure 2.16 SEM images of the final structures in each of the three steps used in fabricating nanoledge structure using EBL. (a) Step 1 - Markers were defined on the substrate. (b) Step 2 - The bottom nanoslit was defined. (c) Step 3 - The top 250 nm slit was aligned on the top of the bottom slit to complete the nanoledge structure.

To obtain a better understanding of the effect of fabrication defects such as positioning of the bottom 80 nm width slit with respect to top 250 nm width slit, simulations were carried out by systematically changing the offset between the top and the bottom slits and analyzing the transmission spectrum. The obtained transmission spectra, simulated when the background refractive index is 1, are illustrated in the Figure 2.17. It can be seen that the intensity of peak A (Figure 2.20) increases with increasing offset while another peak seems to appear adjacent to it. It is also interesting to note that peak B slightly red shifts with increasing offset.

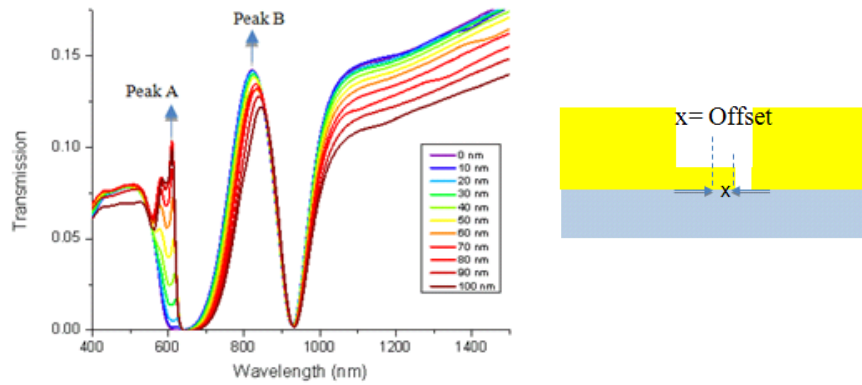


Figure 2.17 Simulated transmission spectra of the nanoledge structure under different offset values (x)

Transmission spectra of the EBL fabricated nanoledges were collected while changing the refractive index of the outside medium as depicted in Figure 2.18 (a). The bulk refractive index sensitivity of the nanoledge structure was calculated using the peak B, which was calculated to exhibit a sensitivity of 315 nm/RIU (see Figure 2.18 (b)) and figure of merits was calculated to be 3.3 RIU^{-1} . The bulk refractive index sensitivity of dip C and peak A were found to be, 189 nm/RIU and 9 nm/RIU respectively.

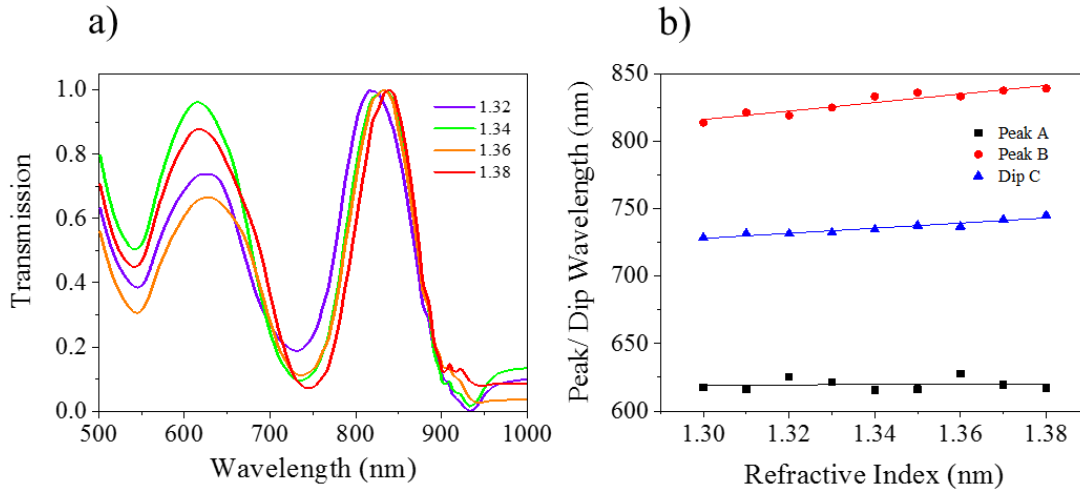


Figure 2.18 (a) Transmission spectra of the EBL fabricated nanoledge structure, periodicity of 600 nm, with different refractive index standards for normally incident TM polarized light. (b) Peak A, B, and dip C wavelengths are plotted against the refractive index of the outside medium. Slope of the fitting curve gives the RIU sensitivity of the device to be 315 nm/RIU from peak A and the figure of merit was calculated to be 3.3 per RIU

2.3.2.1 Detecting Albumin-antiAlbumin Interaction using EBL Fabricated Nanoledge Structures

We first measured the transmission spectra of the nanoledge array chip in air and confirmed the SAM formation and antibody attachment to the nanoplasmonic sensing area. The primary peaks of the transmission are normalized to the maximum transmission of the primary peak. We found that the peak A of the three spectra are located at 640.6 nm, 655.1 nm, and 662.7 nm for blank (in air), SAM only, and SAM plus anti-PSA respectively (Figure 2.19). The red shifts of the primary peak are 15 nm for the SAM only and 7 nm for the anti-PSA immobilization.

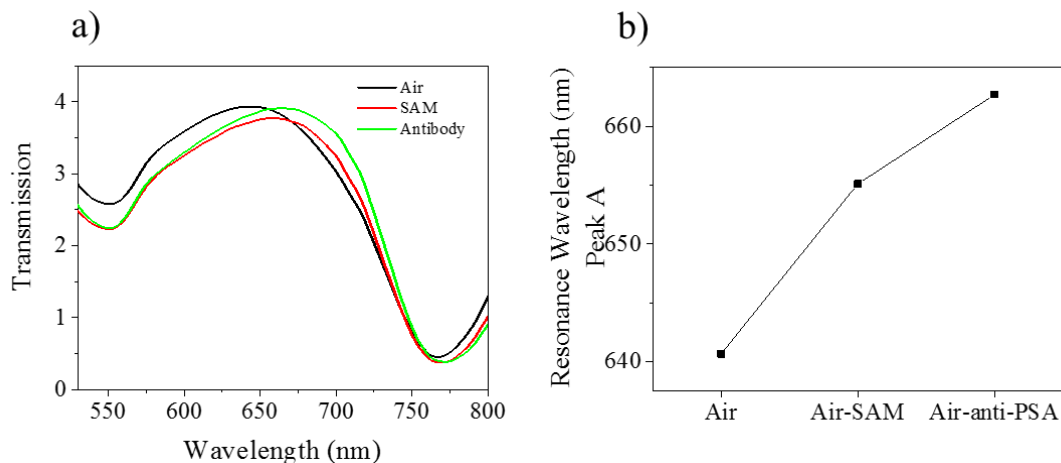


Figure 2.19 (a) Transmission spectra of the EBL fabricated nanolege array before any surface modification in air and after incubating with SAM (air) and the PSA antibody (air) is depicted. (b) Peak A position is plotted after each surface modification for clarity.

A series of PSA solutions of different concentrations were prepared for the PSA binding reaction at the SAM-anti-PSA surface, starting with incubation of buffer solution and increasing PSA concentration from 0.1 pg/mL to 100 pg/mL for 30 min. Then the transmission spectra were collected for each case. Figure 2.20 (a) shows an expanded view of spectral peak A after incubation with PSA solutions and the correlation of primary peak to concentrations of PSA in buffer solutions is shown Figure 2.20 (b). One can find that the primary peak displays a monotonically increasing red shift with increasing concentration over the range of 0-10 pg/mL.

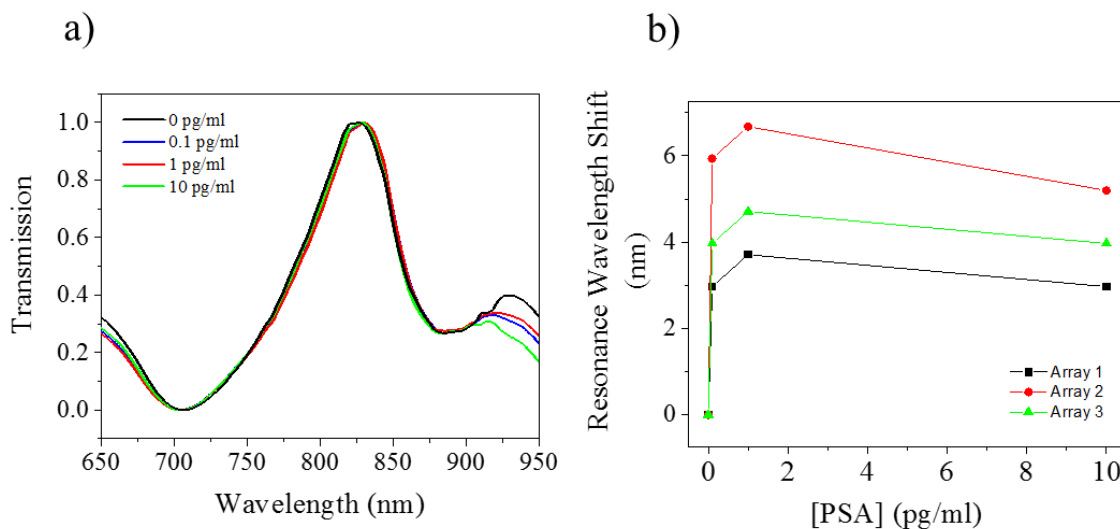


Figure 2.20 Peak spectra after incubation with PSA solutions is illustrated in (a) and in (b) is the correlation of the shift in the peak A position to concentrations of PSA in buffer solutions for three arrays of the nanoledge structure.

Binding of the bovine serum albumin (BSA) to the sensor was studied in order to detect the specificity of the sensor and to confirm the observed shift is not originating from non-specific binding of the analyte to the sensor surface. It can be observed from Figure 2.21 that no significant shift in the spectral position can be observed even after incubating with a 1000 pg/ml concentration of BSA. This observation confirms that the spectral shift observed during the PSA-antibody interaction is originating through specific binding of the PSA to the sensor. The minimum concentration used in our study is 100 fg/mL, corresponding to 2.9 pM. Given a spectrometer resolution of 0.67 nm, the peak shift of 6 nm for the 2.9 pM solution gives a detection limit of 0.32 pM. Our operating hypothesis for the loss in response for concentrations above 10 pg/mL is that the surface of anti-PSA was saturated by PSA, however, more direct evidence is needed for this

hypothesis. Future studies regarding this sensor will be to improve the reproducibility and change the surface modification to allow for a larger concentration range of the PSA detection.

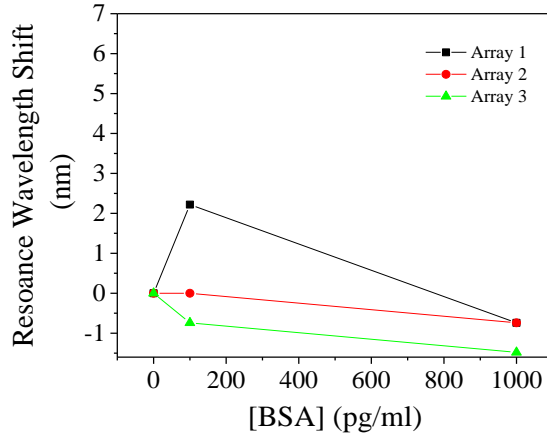


Figure 2.21 Resonance wavelength shift of the Peak A position after incubation with BSA solutions with different concentrations observed for three different arrays of EBL fabricated nanoledge structures.

2.4 CONCLUSIONS AND FUTURE WORK

A combination nanofluidic nanoplasmonics platform was designed and studied for both fluid sample delivery and plasmonic sensing concurrently. Preliminary results of both computational simulation and experiment show promise for an integration of the nanoledge array structure with microfluidic channel for biodetection. The in-plane nanoslit chip in this study should be compatible with microfluidics and emerging lab-on-chip biosensor application.

Biosensing studies performed on the nanoledge structure need further optimization to improve the reproducibility and change the surface modification to allow for a larger concentration range

of the f-PSA detection. However, demonstration of the biosensing capability of nanoledges after integration to a microfluidic system is yet to be demonstrated. In addition, non specific binding and cross interference from real physiological samples needs to be addressed. Stability and affects of long-term shelf-life for these devices also needs be investigated.

2.5 REFERENCES

- (1) Homola, J. Present and future of surface plasmon resonance biosensors. *Anal Bioanal Chem* **2003**, *377*, 528-539.
- (2) Leskova, T. A.; Maradudin, A. A.; Zierau, W. Surface plasmon polariton propagation near an index step. *Optics Communications* **2005**, *249*, 23-35.
- (3) Jung, L. S.; Campbell, C. T.; Chinowsky, T. M.; Mar, M. N.; Yee, S. S. Quantitative Interpretation of the Response of Surface Plasmon Resonance Sensors to Adsorbed Films. *Langmuir* **1998**, *14*, 5636-5648.
- (4) Kim, I.; Kihm, K. Label-free visualization of microfluidic mixture concentration fields using a surface plasmon resonance (spr) reflectance imaging. *Exp Fluids* **2006**, *41*, 905-916.
- (5) Ebbesen, T. W.; Lezec, H. J.; Ghaemi, H. F.; Thio, T.; Wolff, P. A. Extraordinary optical transmission through sub-wavelength hole arrays. *Nature* **1998**, *391*, 667-669.
- (6) Bethe, H. A. Theory of Diffraction by Small Holes. *Physical Review* **1944**, *66*, 163-182.
- (7) Ghaemi, H. F.; Thio, T.; Grupp, D. E.; Ebbesen, T. W.; Lezec, H. J. Surface plasmons enhance optical transmission through subwavelength holes. *Physical Review B* **1998**, *58*, 6779-6782.
- (8) Brolo, A. G.; Gordon, R.; Leathem, B.; Kavanagh, K. L. Surface Plasmon Sensor Based on the Enhanced Light Transmission through Arrays of Nanoholes in Gold Films. *Langmuir* **2004**, *20*, 4813-4815.
- (9) Barnes, W. L.; Dereux, A.; Ebbesen, T. W. Surface plasmon subwavelength optics. *Nature* **2003**, *424*, 824-830.
- (10) Mullett, W. M.; Lai, E. P. C.; Yeung, J. M. Surface Plasmon Resonance-Based Immunoassays. *Methods* **2000**, *22*, 77-91.

- (11) Liu, Y.; Bishop, J.; Williams, L.; Blair, S.; Herron, J. Biosensing based upon molecular confinement in metallic nanocavity arrays. *Nanotechnology* **2004**, *15*, 1368.
- (12) Gordon, R.; Brolo, A. G.; McKinnon, A.; Rajora, A.; Leathem, B.; Kavanagh, K. L. Strong Polarization in the Optical Transmission through Elliptical Nanohole Arrays. *Physical Review Letters* **2004**, *92*, 037401.
- (13) De Leebeek, A.; Kumar, L. K. S.; de Lange, V.; Sinton, D.; Gordon, R.; Brolo, A. G. On-Chip Surface-Based Detection with Nanohole Arrays. *Analytical Chemistry* **2007**, *79*, 4094-4100.
- (14) Ferreira, J.; Santos, M. J. L.; Rahman, M. M.; Brolo, A. G.; Gordon, R.; Sinton, D.; Girotto, E. M. Attomolar Protein Detection Using in-Hole Surface Plasmon Resonance. *Journal of the American Chemical Society* **2009**, *131*, 436-437.
- (15) Johnson, P. B.; Christy, R. W. Optical-Constants of Noble-Metals. *Physical Review B* **1972**, *6*, 4370-4379.
- (16) Palik, E. D.; Ghosh, G.: *Handbook of optical constants of solids*; [Set ed.; Academic Press: London, 1998.
- (17) Lee, K. L.; Lee, C. W.; Wang, W. S.; Wei, P. K. Sensitive biosensor array using surface plasmon resonance on metallic nanoslits. *J Biomed Opt* **2007**, *12*.
- (18) Kofke, M. J.; Waldeck, D. H.; Fakhraai, Z.; Ip, S.; Walker, G. C. The effect of periodicity on the extraordinary optical transmission of annular aperture arrays. *Applied Physics Letters* **2009**, *94*, 023104.
- (19) Chen, J.; Li, Z.; Yue, S.; Xiao, J.; Gong, Q. Plasmon-Induced Transparency in Asymmetric T-Shape Single Slit. *Nano Letters* **2012**, *12*, 2494-2498.
- (20) Conlisk, A. T.: *Essentials of Micro- and Nanofluidics: With Applications to the Biological and Chemical Sciences*; Cambridge University Press, 2012.
- (21) Hsu, Y.-H.; Moya, M. L.; Abiri, P.; Hughes, C. C. W.; George, S. C.; Lee, A. P. Full range physiological mass transport control in 3D tissue cultures. *Lab on a Chip* **2013**, *13*, 81-89.
- (22) Choi, S.; Lee, M. G.; Park, J.-K. Microfluidic parallel circuit for measurement of hydraulic resistance. *Biomicrofluidics* **2010**, *4*, 034110.
- (23) Love, J. C.; Estroff, L. A.; Kriebel, J. K.; Nuzzo, R. G.; Whitesides, G. M. Self-Assembled Monolayers of Thiolates on Metals as a Form of Nanotechnology. *Chemical Reviews* **2005**, *105*, 1103-1170.
- (24) Sievilä, P.; Chekurov, N.; Tittonen, I. The fabrication of silicon nanostructures by focused-ion-beam implantation and TMAH wet etching. *Nanotechnology* **2010**, *21*, 145301.

- (25) Leen, J. B.; Hansen, P.; Cheng, Y.-T.; Hesselink, L. Improved focused ion beam fabrication of near-field apertures using a silicon nitride membrane. *Opt. Lett.* **2008**, *33*, 2827-2829.
- (26) Harder, P.; Grunze, M.; Dahint, R.; Whitesides, G. M.; Laibinis, P. E. Molecular Conformation in Oligo(ethylene glycol)-Terminated Self-Assembled Monolayers on Gold and Silver Surfaces Determines Their Ability To Resist Protein Adsorption. *The Journal of Physical Chemistry B* **1998**, *102*, 426-436.
- (27) Barrios, C. A.; Banuls, M. J.; Gonzalez-Pedro, V.; Gylfason, K. B.; Sanchez, B.; Griol, A.; Maquieira, A.; Sohlstrom, H.; Holgado, M.; Casquel, R. Label-free optical biosensing with slot-waveguides. *Opt Lett* **2008**, *33*, 708-710.

3.0 ENHANCED SENSITIVITY OF DELOCALIZED PLASMONIC NANOSTRUCTURES

This chapter has been published in “Mendis, M. N.; Mandal, H. S.; Waldeck, D. H., Enhanced Sensitivity of Delocalized Plasmonic Nanostructures. *The Journal of Physical Chemistry C* 2013, 117 (48), 25693-25703”. The thesis author conducted the fabrication, optical characterization, theoretical calculations, modelling and biosensing studies of the square nanoparticle chain structures in discuss. The supporting information for this chapter is provided in Appendix A.

This work reports on the observation of a delocalized surface plasmon resonance (DSPR) phenomenon in linear chains of square-shaped silver nanoparticles (NP) as a function of the chain length and the distance between the nanoparticles in the chain. Transmission spectra of the silver nanoparticle chains reveal the emergence of new, red-shifted extinction peaks that depend strongly on the spacing between the nanoparticles and the polarization of the exciting light with respect to the chain axis. As the spacing between the nanoparticles in the linear chain decreases and the number of nanoparticles in the linear chain increases, the strength of the new extinction features increase strongly. These changes can be described by a tight-binding model for the coupled chain, which indicates that the origin of the phenomenon is consistent with an increased coupling between the nanoparticles. FDTD calculations reveal that the electric field is strongly enhanced between the nanoparticles in the chain. The DSPR response is found to be much more sensitive to dielectric changes than the localized surface plasmon resonance (LSPR).

3.1 INTRODUCTION

Nanoparticle (NP) based plasmonic sensors offer great promise for deploying miniature, multiplexed, and label free detection platforms.¹⁻³ The general working principle for this particular class of sensors is a shift in the localized surface plasmon resonance (LSPR) peak upon a change in the dielectric properties of the surrounding medium, for example, the adsorption of molecules on the surface of the NP.¹⁻³ Over the past decade, numerous reports have described different strategies for improving the sensitivity of these sensors by changing the size^{4,5}, shape^{4,6-15}, aspect ratio^{5,12,16}, and material composition⁴ of the NP. Despite these efforts, the molecular sensitivity is still generally limited to a few nm peak shifts.^{1,14,17-22} Even though recent developments²³⁻²⁶ in the field have contributed to improved sensitivity of these sensors, the search still continues for novel platforms based on these plasmonic NPs that exploit their exceptional sensitivity to perturbations in local environment for the detection of molecular and/or biomolecular events.

Clusters of NPs in close proximity exhibit a unique set of collective plasmon modes, which can be described through a superposition of plasmon modes excited on individual NPs in the assembly.²⁷⁻³¹ This topic has gained much interest in recent years because of the rich phenomena that these coupled oscillators can display, such as electromagnetic transparency and Fano resonances.^{30,32,33} The dependence of the optical response of these coupled structures on local perturbations, such as a change in the local dielectric constant and symmetry-breaking, has spurred new promise for their use in applications, as compared to uncoupled systems.

Linear chains of NPs provide a useful platform for exploring the coupling of plasmonic metal NPs, and one dimensional NP chains have been studied for their use as waveguides in nanoscale energy transfer.^{27,29,34-37} In addition, NP dimers (or nanoparticle junctions) have been used to demonstrate single molecule sensitivity for SERS applications.^{38,39} Many studies have

taken a top-down fabrication approach with precise size and gap control of the NP pairs/chains.^{27,40-49} Computational studies and far-field spectroscopic studies on one-dimensional metal NP chains show that the resonance wavelength of the longitudinal mode increases with the increasing chain length in comparison to that of a single NP, and this resonance wavelength shift plateaus with the increasing number of NPs in the chain.^{40,41,50-53} The optical properties of metal NP chains are not only dependent on the particle size⁵⁴, shape⁵⁵, and material composition⁴⁶ but also on the inter-NP distance^{29,43,47,48,50-52} and the number of NPs^{35,41,46,50-52} in a given chain. As we discuss, these phenomena indicate that the plasmon modes delocalize along the NP chain.

Despite the body of work regarding the coupling between NPs in linear chains, the use of their coupled resonances for sensing dielectric changes is largely unexplored. In this work we systematically investigate the generation of collective plasmon resonances of one-dimensional square NP chains, termed a delocalized surface plasmon resonance (DSPR), and examine its sensitivity to dielectric changes. A simple tight-binding model is applied to the experimental data for the DSPR energy as a function of chain length, and it is used to extract a coupling constant between the NPs in the chain and examine its dependence on the inter-particle spacing. The inter-particle distance dependence of the plasmonic interaction of these NP chains and its sensitivity to the environment's dielectric constant are examined. These latter findings show that it is possible to use the coupled modes to obtain resonance peak wavelength shifts from molecular adsorbates that are much larger than the shifts observed for individual NPs.

3.2 EXPERIMENTAL

3.2.1 Fabrication of Square NP chains:

Electron beam lithography (EBL, Raith e-Line) was used for the fabrication of square Ag NP ($170 \times 170 \text{ nm}^2$, and 50 nm thick) arrays ($30 \times 30 \text{ }\mu\text{m}^2$). The steps involved with the fabrication are summarized in Figure S1 in the supporting information section. Conductive indium tin oxide coated glass slides (ITO) (Delta's Technologies) were used as the substrates to minimize charging during the fabrication. ITO substrates were rinsed using three solvents: acetone, methanol and isopropanol; ultrasonication was performed in each solvent for 5 min. The ITO substrates were then rinsed with deionized water and dried with a N_2 gas stream. These substrates were baked at 180 °C for 2 min to remove any moisture from the surface. Poly-methyl-methacrylate (950k A4 PMMA, MicroChem) was spun on the substrate at a speed of 1500 rpm for 40 s using a spin processor (Laurell WS-400-6NPP-LITE) and baked on a hot plate at 180 °C for 5 min. E-beam writing was performed at an acceleration voltage of 20 keV and with an exposure dose of $300 \text{ }\mu\text{C}/\text{cm}^3$ using a $7.5 \text{ }\mu\text{m}$ aperture to write the NP chain pattern on PMMA. The sample was then developed for 90 s in a developing solvent consisting of methyl isobutyl ketone and isopropanol in a 3:1 ratio to dissolve the exposed PMMA. Then silver (Ag) was evaporated onto this sample to a thickness of 50 nm, along with 3 nm of titanium to help the Ag to better adhere to the substrate. The rate of evaporation was maintained at $0.2 \text{ \AA}/\text{s}$ to allow smooth deposition of the metal. After the metal deposition, the samples were kept overnight in acetone to remove the remaining PMMA resist.

3.2.2 Sample Characterization

Sample imaging was done using an SEM in the EBL system. The acceleration voltage was chosen to be 4 keV. Spectral characterization of the square NP chains was carried out using a microspectrophotometer (Craic QDI 2010). A linear broadband polarizer (Glan-Taylor) which was placed in between the sample and the condenser (Figure 1) was used to polarize the light for excitation of transverse and longitudinal LSPR modes. Spectra were collected using a 15× objective in a 20 μm × 20 μm square aperture and a plane 20 μm × 20 μm area of the ITO substrate was used as the reference.

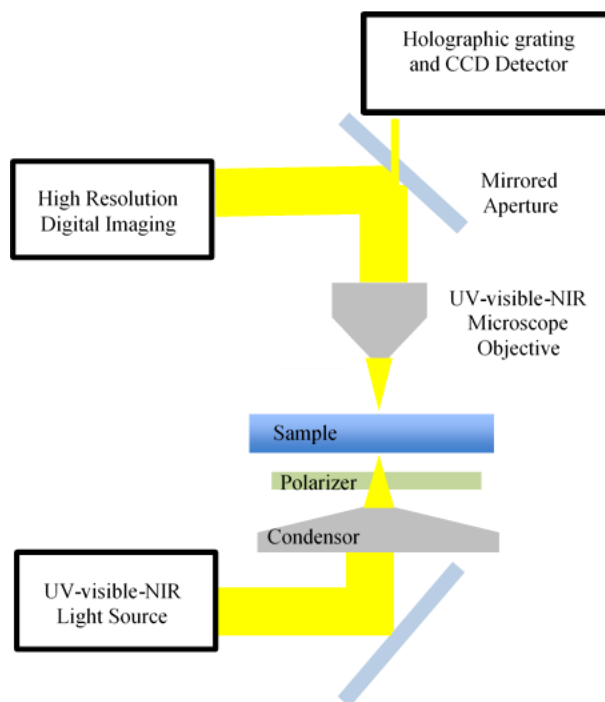


Figure 3.1 Sketch of optical set-up used during the optical characterization of the samples. The yellow lines indicate the light pathway.

3.2.3 Self-assembled Monolayers Formation

1-pentanethiol (C5), 1-octanethiol (C8), 1-decanethiol (C10), 1-dodecanethiol (C12), 1-hexadecanethiol (C16), and 1-octadecanethiol (C18) were obtained from Sigma Aldrich and used for the experiment without further purification. Self-assembly of the alkanethiol monolayer was carried out in a 1 mM solution of alkanethiol in absolute ethanol. The chips were thoroughly washed with copious amounts of ethanol to remove any impurities. Samples were incubated in each alkanethiol solution overnight to form a well-packed SAM. Transmission spectra of the square NP chain arrays were recorded before and after SAM preparation using the microspectrophotometer to determine the peak shifts.

3.2.4 Finite-difference time-domain (FDTD) simulations

Simulations were conducted using the FDTD method (Lumerical Solutions, Inc.). A three-dimensional (3D) FDTD method was used to accurately calculate the light transmission, electric field intensity profiles, and charge distribution profiles of the silver NP chain arrays. The NP chains consist of 170 nm×170 nm square NPs with a thickness of 50 nm. Edge rounding of the square NPs was done with a 5 nm radius cylinder so that they better resemble the experimentally realizable NPs. The NP clusters were simulated on an infinite substrate represented by dielectric constants extracted from Palik data for silicon dioxide.⁵⁶ In all the simulations, a uniform mesh with 1 nm in all directions was used for the silver NPs and a non-uniform mesh was used elsewhere. The boundary conditions in the plane of the structures (i.e. the \hat{x} and \hat{y} direction) were chosen to represent an infinite square array. The boundary in the \hat{z} direction was set to contain a perfectly

matched layer absorbing boundary condition. The structure was illuminated using a normally incident broadband plane wave source from the substrate side, with the polarization direction either parallel or perpendicular to the chain axis to excite longitudinal or transverse plasmon modes, respectively. A 2D monitor was used to collect and record the transmission data whereas 3D monitors placed around the NPs were used to collect field profiles. The permittivity of silver was modeled using data from Palik.⁵⁶ The edge-to-edge separations between two nearest neighbor NP chain clusters were maintained to be 1000 nm both in the \hat{x} and the \hat{y} directions.

3.3 OPTICAL RESPONSE OF NANOPARTICLE CHAINS

This section discusses the dependence of the observed transmission spectra on the nanoparticle chain properties and compares these experimental findings to the FDTD simulation results for linear NP chains. In addition an analytical formula based on a tight binding model is used to describe the dependence of the DSPR on the chain length and to extract an interparticle coupling strength.

3.3.1 Dependence on Distance between NPs in Chain:

Square NP chains were fabricated by changing the interparticle distance (d) systematically from 130 nm to ~30 nm ($d = 830$ nm, 130 nm, 105 nm, 80 nm, 75 nm, 58 nm, 47 nm, and 36 nm). Figure 2 shows transmission spectra for a square NP tetramer chain as a function of the interparticle spacing, d , under longitudinal polarization of the incident light. All the spectra are

normalized to the number of NPs in the field of view under the aperture to remove any effect from a change in the NP density.

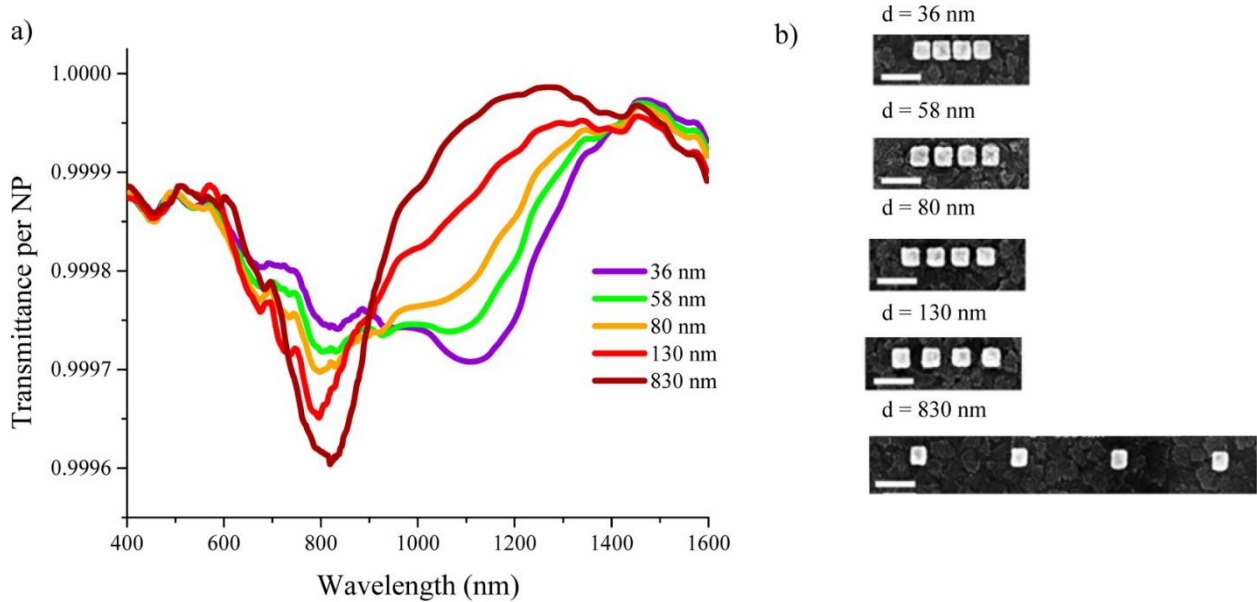


Figure 3.2 a) The transmission spectra of a square nanoparticle tetramer chain are plotted for different inter-particle separations. b) SEM images are shown for five of the square NP tetramer chains in panel A. The scale bar is 400 nm.

When isolated by a large interparticle separation (the case of $d = 830$ nm, edge to edge, in Figure 3.2), the NP chain shows an extinction spectrum that has a main LSPR peak, λ_{LSPR} , at ~ 811 nm, a less intense peak around ~ 450 nm, and no peak in the near IR region. The FDTD calculated transmission spectrum (see supporting information Figure A2 (a)) of an isolated nanoparticle also exhibits two distinct peaks, with peak positions slightly to the blue as compared to the experimental transmission spectrum. The difference between the experiment and the calculation may arise from the underlying ITO film in the samples as well as fabrication defects. The FDTD results (see Appendix A; Figure A2 (b)), show that the ~ 811 nm peak has its electric field intensity concentrated towards the substrate side and the ~ 450 nm peak has its electric field

intensity predominantly on the vacuum side. As discussed elsewhere for nanocubes, these modes likely result from a mixing of dipolar and quadrupolar modes of the silver NPs and the symmetry breaking induced by the substrate.^{11,57,58} Note that the additional small features in the transmission spectrum of the NPs may arise from diffractive coupling mediated through the substrate and air media, however the discussion of these is beyond the scope of the current study.

As the interparticle separation is reduced from 830 nm to 80 nm along the polarization direction of the excitation light, the growth of a shoulder on the extinction peak appears; the magnitude of this shoulder increases with a further reduction of the interparticle separation to 58 nm. At separation 36 nm, this shoulder has evolved into a well-defined peak of its own. It is this new red-shifted spectral feature that we refer to as the DSPR. In connection with the growth of the DSPR peak, the LSPR peak of the individual NPs decreases in amplitude. Note that the peak area under the LSPR peak reduces and the area under the DSPR peak grows rapidly with decreasing inter-particle distance. This observation reveals a shift in the oscillator strength of the plasmon resonance of the NPs from the LSPR to the DSPR as the NP spacing decreases. (The peak area under the DSPR plotted against the inter-particle distance for a four NP chain is shown in Figure A3, supporting information.)

3.3.2 Dependence on the Number of NPs in the Chain

The strength and position of the DSPR extinction feature also depends on the number of NPs in the chain. Figure 3.3(b) and 3.3(c) show transmission spectra for NP chains ($d \sim 36$ nm) comprised of 2, 3, 4, 5, and 7 NPs for two different light polarizations, longitudinal and transverse, with respect to the chain axis. The raw spectra again have been normalized by the number of NPs

in the field of view. As the number of NPs in a linear chain increases, the DSPR peak that is observed under longitudinal polarization shifts to longer wavelength. Figure 3(d) plots the wavelength at which the DSPR extinction is a maximum, λ_{DSPR} , as a function of the number of NPs in the chain. The λ_{DSPR} was determined by first subtracting the transmission spectrum of an isolated NP from that of the NP chain, and then assigning the peak maximum.

From Figure 3.3(b) it can be observed that under longitudinal polarization the maximum of the extinction shifts strongly to the red with an increase in the number of NPs in the chain. However, this shift attenuates as the chain length grows and is nearly saturated for chains of six or more NPs. A similar observation has been reported for strongly coupled linear chains of spherical NPs.⁵⁰ These spectra also reveal that the DSPR absorbance width broadens as the number of NPs in the chain increases. Broadening of the resonance peak when strong near field coupling occurs has been reported previously and has been attributed to increased radiative damping and excitation of dipole-like modes.^{50,53}

Figure 3.3(c) show the corresponding transmission spectra under transverse polarization. These spectra show only an LSPR signal, and no significant shift for chains of two or more NPs. Note that a small blue shift as compared to the case of isolated NP is indicated; see Figure 4(c) and (d). According to the dipole coupling model, a blue shift of the resonance wavelength arises from repulsion between the induced surface charges on neighboring NPs under the transverse polarization conditions, and this behavior has been reported previously.^{27,50} Also note the large drop in peak area on proceeding from one NP to two NPs, which is consistent with a dipole-dipole coupling picture for this excitation geometry.⁵⁹ For transverse polarization, the NP chains exhibit no significant changes in the resonance wavelength with changing interparticle spacing. It should be noted that defects during fabrication give rise to slight differences in the width and the length

of the square NP (ie., the NPs are not perfectly square), and this causes differences in resonance wavelengths for a single NP when the polarization direction is changed; see the case of a single NP in Figure 3.3(d). FDTD calculations suggest that there is about ~50 nm change in the resonance wavelength when the length of the NP change 150 nm – 170 nm in parallel to the direction of polarization.

Overall, the extinction per NP is higher in the chains than for isolated NPs under longitudinal polarization. To clearly observe this trend the area under the DSPR peak, which was integrated over energy (eV) and normalized per number of NPs in the field of view, was calculated for NP chains at a 36 nm inter-NP distance and is plotted in Figure 3.3(e). The area under an extinction peak is proportional to the oscillator strength for the particular transition(s); hence the plot in 3.3(e) shows how the oscillator strength of the visible and near-IR modes change for plasmonic NP chains of different length. From Figure 3.3(e) it is evident that the peak area per NP increases systematically as the chain length increases and then saturates as the number of NPs in the chain reaches about six. This chain length coincides with the length for which the DSPR resonance wavelength shift saturates. These observations suggest that the delocalization length of the DSPR excitation is about six NPs for the chains with 36 nm interparticle distance.

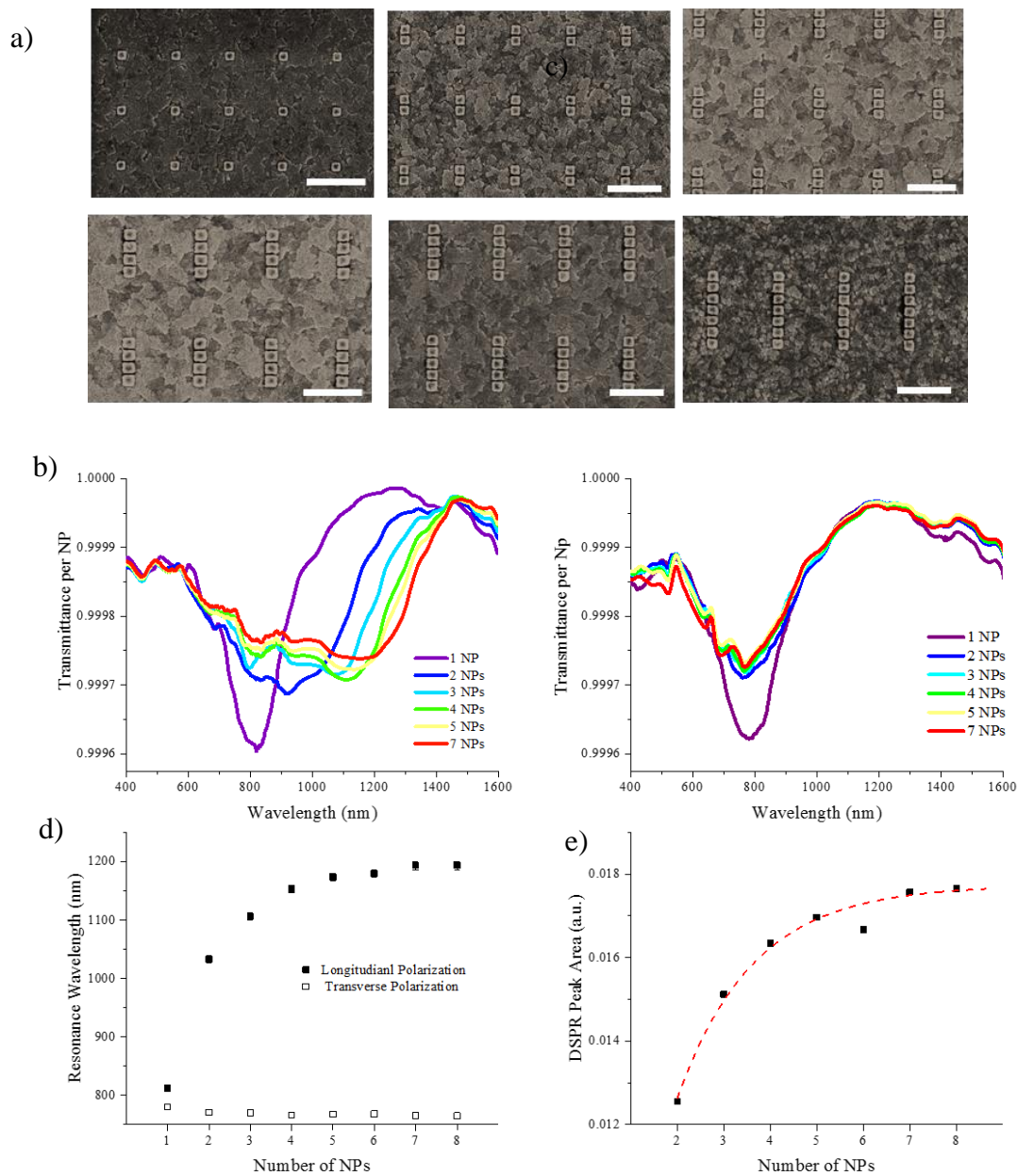


Figure 3.3 Panel a) shows the SEM images for square nanoparticle chains (the scale bar is 1000 nm). Panel b) and c) shows the evolution of transmission spectra of those chains under b) longitudinal and c) transverse polarization, collected in air. d) The wavelength maximums of the DSPR are plotted against the NP chain length (see text for details). The error bars in these peak wavelength positions are smaller than size of the symbol e) The DSPR peak area normalized per NP is plotted versus the NP chain length. The red dashed line is given as a guide to eye.

3.3.3 FDTD Simulations of NP Tetramers

To gain more insight into the origin of the spectral features, finite-difference time-domain (FDTD) simulations were conducted on a tetramer chain of square NPs to extract the electric field intensity enhancement ($|E|^2/|E_0|^2$) profile at the DSPR excitation wavelength for the case of light polarized along the NP chain. These simulations show that both the intensity and extension of the electric field between the NPs increases as the inter-NP separation decreases; see Figure 3.4(a). The electric field intensity in the middle of the gap between the NPs is plotted in Figure 4(b). These findings are consistent with those reported for NPs in close proximity^{60,61} for which the field strength is enhanced between the NPs.

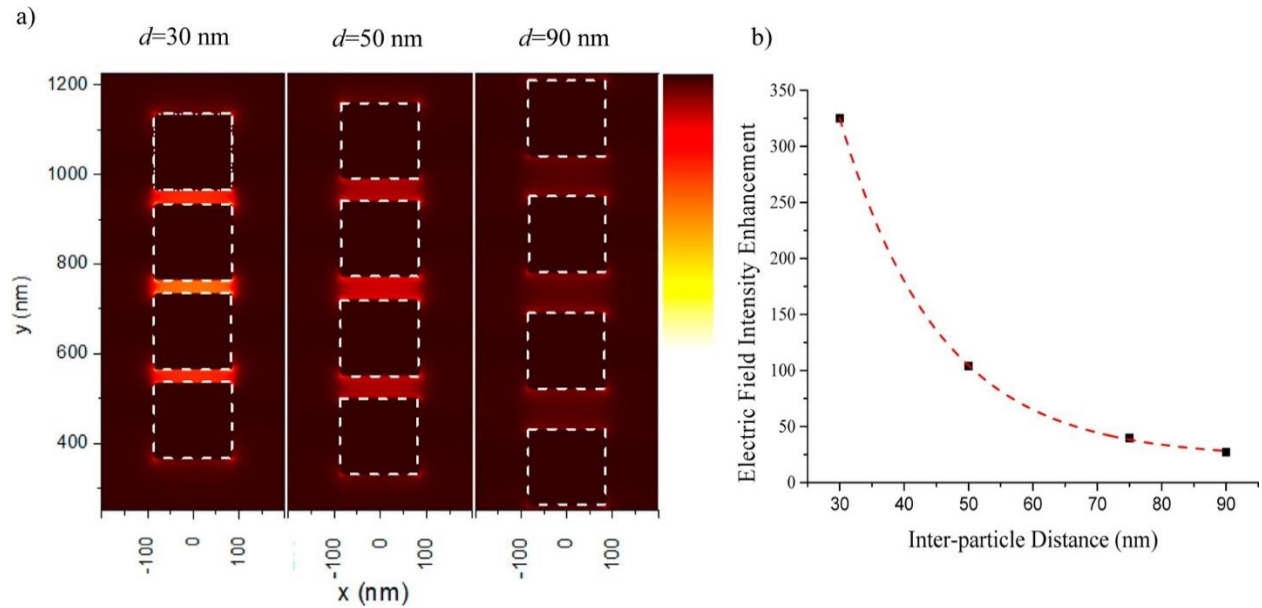


Figure 3.4 a) Electric field intensity enhancement ($|E|^2/|E_0|^2$) profiles are shown for a four NP chain with three different nanoparticle separations (d). The direction of the light polarization is parallel to the major axis of the clusters. The scale bar ranges from an amplitude of 0-700. b) The electric field intensity at the x-y center of the cluster is plotted against the inter-particle distance. The red dashed line is given as a guide to eye.

However, under transverse polarization the FDTD calculations indicate that no significant electric field enhancement occurs in the gap region between the NPs. (see Figure S4 in supporting information). These observations suggest a correspondence between the enhanced electric field in the inter-particle areas and the experimentally observed DSPR peak for the NP chain. The enhanced electric field in the region between the NPs enhances the coupling among the individual NPs and points to a coherent/collective plasmonic oscillation (with a macro-dipole) extended through the NP chain; i.e., a delocalized surface plasmon resonance (DSPR).

3.3.4 Tight-Binding Model for NP Chain

A simple tight-binding approach (or Hückel model) can be used to rationalize the observations and to provide a semi-quantitative understanding of the coupled NP system.⁶² In this model, only nearest neighbor coupling between the NPs is considered and the coupling strength is described by a parameter A . Using this approach for N NPs in a chain, one finds that the eigenenergies E are given by

$$E = E_0 + 2A \cos\left(\frac{m\pi}{N+1}\right) \quad \text{Equation 3.1}$$

In Equation 1, E_0 is considered to be the resonance energy of a single NP and m is a mode number. For a fixed value of A , the resonance energy E of the NP chain decreases, and it asymptotically approaches a value of $E = E_0 + 2A$ for an infinitely long NP chain ($N \rightarrow \infty$). This behavior is consistent with the spectral observations for a chain of square NPs under longitudinal polarization; the resonance wavelength of the DSPR peak systematically red shifts towards a

limiting value as the number of NPs in the chain increases. Equation 1 also predicts that the resonance energy E should decrease, as the coupling constant A increase at a fixed value of N . This prediction is consistent with the systematic red shift that is observed for the DSPR as the inter-particle distance is reduced at a fixed number of NPs in the chain (see Figure 3.2(a)).

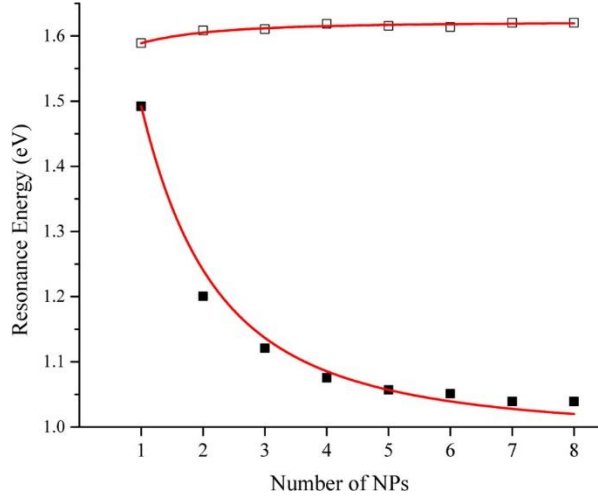


Figure 3.5 The resonance energy maximum of the DSPR is plotted versus the number of NPs in the chain under longitudinal (■) and transverse (□) polarization; the red line shows a fit to the data by Equation 1. This analysis is for a 36 nm fixed inter-particle distance.

The plots in Figure 3.5 for the NP chains with a 36 nm spacing show that Equation 1 describes the experimentally obtained data well. Figure 3.5 shows the experimentally determined DSPR peak energy as a function of the number of NPs in the chain. The value of E_0 is taken to be the resonance energy of the single NP array, in which the NPs are separated by 830 nm. The red line indicates the best fit by Equation 1 which yields a coupling constant of -0.25 eV under longitudinal excitation of the NPs. In the fit, the mode number m was assumed to be one which

indicates an in-phase excitation of all NPs in the chain. Other mode numbers correspond to different resonances in the system, which may or may not be excited by direct light illumination, but they would be higher in energy than the $m=1$ mode. When light is transverse polarized, no DSPR peak is observed. If one fits the resonance energy of the main transmission dip by Equation 1, a small coupling constant of +0.016 eV is extracted (Figure 3.5). These parameters indicate that the NP chains exhibit significant coupling under the longitudinal polarization, but a negligible coupling under transverse polarization.

3.3.5 Distance Dependence of the NP Coupling

Two different regimes of coupling and its distance dependence have been distinguished for arrays of NPs. For the inter-NP distances on the order of the wavelength of light, far field diffractive coupling with an inverse distance dependence dominates; they can affect the spectral line shape.⁶³ For the interparticle distances that are comparable to the NP size or smaller, near field interactions are important. Brongersma *et al.*^{27,29} report an inverse distance-cubed (center-to-center distance between two adjacent NPs) dependence for the plasmon peak energy of 50 nm diameter NPs at distances of 75 nm to 125 nm, which is consistent with the predictions of the point dipole model. In a simulation study using the T-matrix method, Harris *et al.*⁵² have reported an inverse distance dependence for the wavelength shift of nanosphere chains at very small gap separations, and this behavior is compared to the van der Waals interaction between spheres at very short interparticle distances.⁶⁴ A number of works^{43,47,48} report an exponential decay in the peak shift ratio with increasing inter-particle gap scaled by the NP size for the longitudinally coupled plasmon between two NPs. This relationship was reported to yield a universal decay constant

irrespective of NP shape, size, material or the type of resonance giving rise to the ‘plasmon ruler equation’⁴³:

$$\frac{\lambda - \lambda_0}{\lambda_0} = \alpha \cdot \exp\left(-\frac{d/L}{\tau}\right) \quad \text{Equation 3.2}$$

in which λ is the resonance wavelength of the NP dimer, λ_0 is the resonance wavelength of an isolated NP, d is the inter-particle spacing between the NPs in the dimer, and τ is the characteristic decay constant. In order to explore the effect of the inter-NP separation on the DSPR, the resonance energy was compared with these existing models.

Figure 3.6(a) shows a plot of the natural logarithm of the DSPR peak wavelength shift ratio $\left(\frac{\lambda - \lambda_0}{\lambda_0}\right)$ versus d/L , the ratio of the interparticle distance (d) to the length (L) of the square NP. For each chain length the data display a linear behavior, and it is possible to extract the decay constant and maximum fractional wavelength shift from the slope and the intercept of the best fit line; see Figure 3.6(a). Figure 3.6(b) shows how the fractional wavelength shift and its characteristic decay constant depend on the NP chain length. The data in Figure 3.6(b) indicate that the decay constant for two square NP chain is around 0.58 ± 0.2 , which is much larger than what has been found for coupled Au disks (~ 0.2).⁴³ From Figure 3.6(b) it is evident that the decay constant increases for a three NP chain as compared to a two NP chain, and then decreases with further increase in the chain length until it plateaus at about 0.8 ± 0.1 . This high value may reflect a shape dependence of the decay constant as suggested by Tabor *et. al*⁶⁵, a dependence on the material response (Ag vs Au), or a combination of the two. This observation suggests the existence of very strong near neighbor coupling in square shaped NP chains.

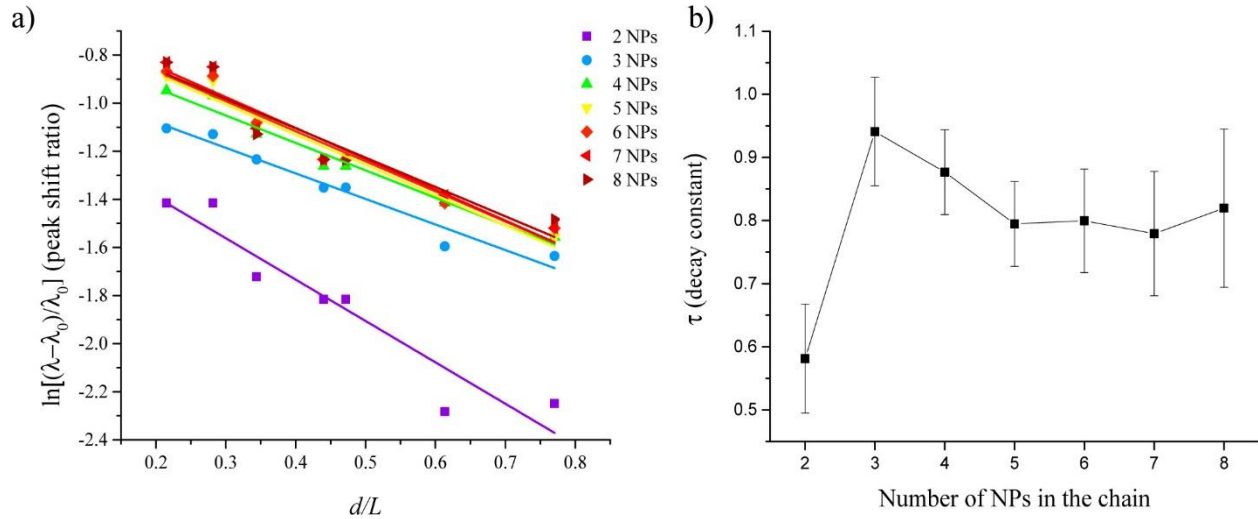


Figure 3.6 (a) The scaled DSPR wavelength shift ratio is plotted versus the scaled gap ratio for different chain lengths of square NP chains. The slope of the best linear fit for each chain length provides the decay constant and these values are plotted in panel (b).

Different functional forms were used to evaluate the effect of the interparticle distance on the coupling constant A , which was obtained from fits of the data by Equation 1; see Figure 3.7(a). Figures 3.7(b) through 3.7(d) show different functional relationships for the decay of A with the interparticle separation. Because some previous works have predicted that a power law function should exhibit a good fit for strongly coupled plasmonic systems,⁶⁶⁻⁶⁹ a log-log plot of the coupling constant versus the inter-NP distance was performed; see Figure 3.7(b). As the inter-NP distance increases the numerical value of the coupling constant decreases, and its fall-off can be described by a power law of the form $A \propto d^{-0.42}$. In order to further investigate these results FDTD calculations were performed to obtain the transmission spectra of NP chains of different gap separations. The transmission spectra were fitted by a *Breit-Wigner-Fano lineshape*⁷⁰ in order to

deconvolute the DSPR peak and extract its wavelength position; then Equation 3.1 was used to obtain the coupling constant A . A log-log plot of these coupling constant A values and the interparticle distance d exhibit a relationship of, $A \propto d^{-0.3}$ that is similar to the experimental data. (see Figure A5 in supporting information).

Figure 3.7(c) shows a plot of the log of the coupling constant versus the log of the center-to-center distance, and a fit (red curve) by an equation of the form $A \propto (L+d)^{-x}$, where now $(L+d)$ is the center-to-center separation between two NPs. If a simple point dipole model was appropriate, then one expects to find a slope of -3, which is represented by the dashed line and clearly gives a poor fit. From the slope of the best fit line a value of -1.5 is extracted for the exponent; *i.e.*, the coupling constant has a $(L+d)^{-1.5}$ distance dependence. The fact that the distance dependence deviates from the point dipole prediction is not surprising, as the gaps studied here are small compared to the size of the NP. These observations demonstrate that the extended nature of the charge distribution is important to consider for these large non-spherical NPs.

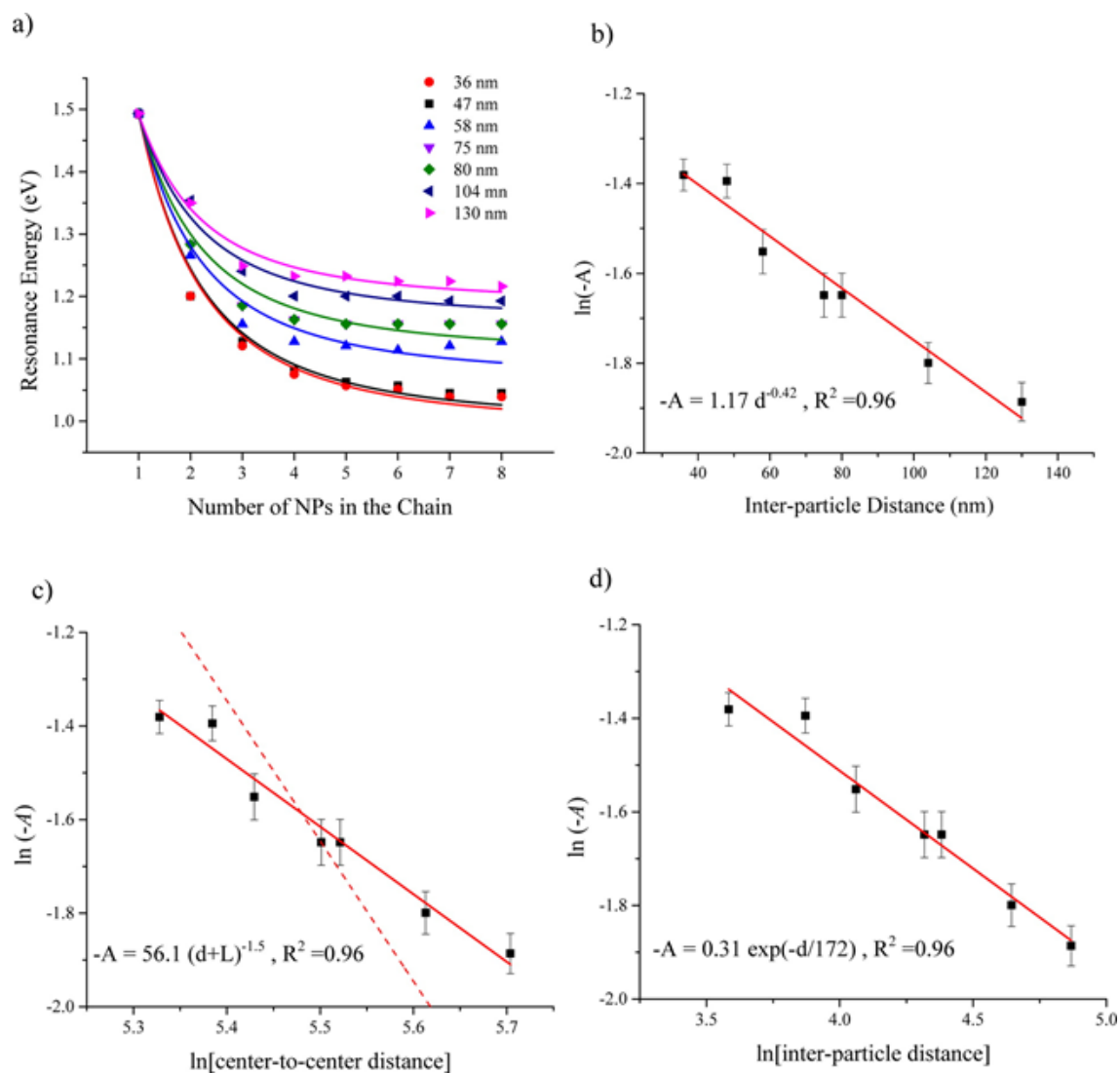


Figure 3.7 (a) The resonance energy maximum of the DSPR is plotted versus the number of NPs in the chain under longitudinal polarization for different inter-particle distances, similar to panel 6(a), to obtain a coupling constant A . A plot of the log of the coupling constants versus the log of the center-to-center distances between nanoparticles is shown in (b), and the natural logarithm of the coupling constant ($-A$) versus the center-to-center distance between NPs in the chain is shown in c). Panel (d) shows a plot and analyses for an exponential function. In panel b, c, and d the solid red line is the best fit to a line, and in panel c the red dashed line indicates the point dipole model.

Figure 3.7(d) shows a plot of the $\ln(-A)$ versus distance, and a fit to an exponential decay dependence. The single exponential decay fit gives a slope of -0.0058 nm^{-1} , indicating a characteristic decay length of $\sim 172 \text{ nm}$; or if it is scaled by the NP length of 170 nm it is ~ 1.0 . FDTD simulations (see Figure A5(b)) are in good agreement with this result. All these analyses suggest that the coupling between square NPs in these one dimensional chains is much stronger than that reported for dimers and chains of other shaped NPs.

3.4 EFFECT OF SAM ON NP CHAIN OPTICAL RESPONSE

Given that the localized surface plasmon resonance (LSPR) of NPs is strongly dependent on molecular adsorbates⁷¹, the sensitivity of the DSPR's peak wavelength to an adsorbed molecular film was tested by forming alkanethiol self-assembled monolayers (SAMs) of different lengths on different square NP chains.

Figure 3.8(a) shows the normalized transmittance spectrum for an array with $d = 830 \text{ nm}$ LSPR mode that is untreated and compares it to that for Ag NPs that are coated with a dodecanethiol SAM. Analysis of the two spectra shows that the SAM shifts the peak wavelength by $\sim 11 \text{ nm}$ to the red. Figure 3.8(b) shows the transmission spectra of a six nanoparticle chain with $\sim 30 \text{ nm}$ interparticle distance (corrected for the NP density) after modifying the metal NP surface with different chain length alkanethiol SAMs. The transmission spectra display very large red shifts in the DSPR wavelength that depends on the length of the alkyl chains of the SAM and are much larger than that found for the isolated NPs in Figure 3.8(a). For example, when the NP chains were chemically modified by a 1-dodecanethiol SAM, the six NP chain ($d = 30 \text{ nm}$) showed a shift of 115 nm , as compared to the $\sim 11 \text{ nm}$ shift in Figure 3.8(a). The ellipsometric thickness calculated

using the SAM prepared on plain Ag films prepared in the same manner shows that the coverage lies in the expected range (Figure A6).

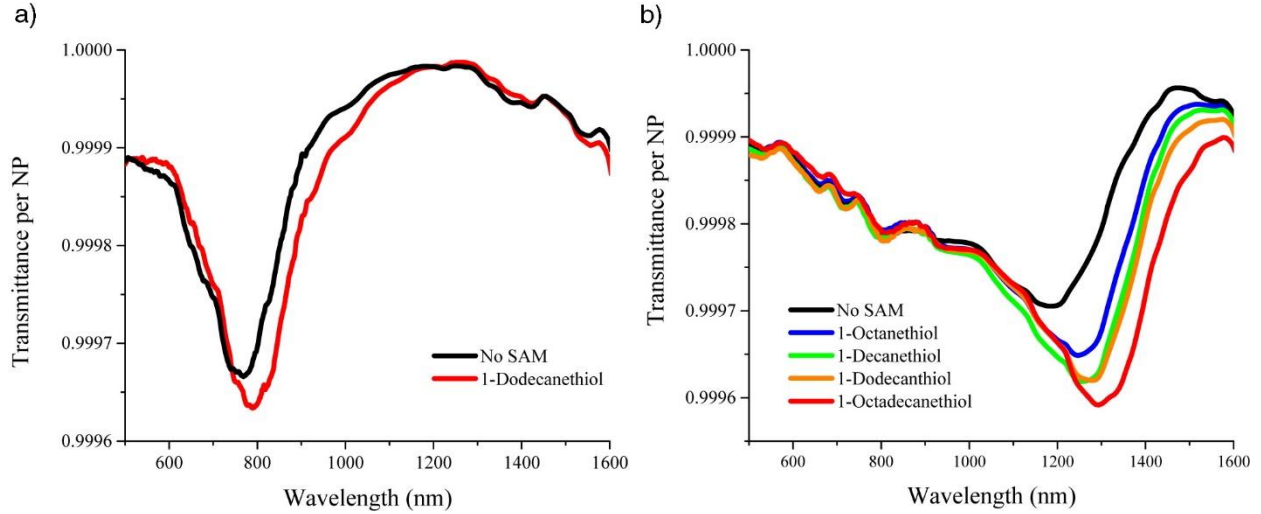


Figure 3.8 Transmission spectra are shown for (a) NPs with large inter-particle separation ($d = 830$ nm) before (black) and after 1-dodecanethiol modifications and (b) for a six NP chain array ($d = 30$ nm) before (black) and after SAM modification (other colors).

Figure 3.9 shows a plot of the SAM induced λ_{DSPR} shift versus the NP chain length ($d = 30$ nm), where the shifts were extracted from transmission spectra of the arrays before and after SAM modification. It is evident that when the number of NPs in the chain increases the resonance wavelength shift increases for a given alkanethiol SAM thickness.

The resonance wavelengths of the SAM coated chain arrays were analyzed by using Equation 3.1. The coupling constant A was found for the NP chain arrays without a SAM (A_{Air}) and with a SAM (A_{SAM}), and they are tabulated in Table 1 for different alkanethiol chain lengths. It can be noted that even though the samples are fabricated using the same procedure, the coupling constant A_{Air} varies between the different devices. It is assumed that these differences arise from

variations in the fabrication, i.e.– changes in NP size and inter-NP distance. The parameter values in Table 1 show that the coupling constant, A , increases after SAM formation by about 10%.

Enhancement in the electromagnetic coupling between metal NP dimers with an increase in dielectric constant of the medium near the NP surface has been reported in few previous studies,^{72,73} and it has been attributed to a reduction in the coulombic restoring force acting on the electrons. That is, as the medium dielectric constant increases, the induced polarization in the NP increases resulting in an increased dipole moment for the NP. The larger dipole should lead to a larger interaction energy between the NPs, even though the increased dielectric constant would act to shield some of this interaction. This mechanism for the enhanced coupling in the presence of a SAM can account for the enhanced sensitivity of the DSPR to molecular adsorbates.

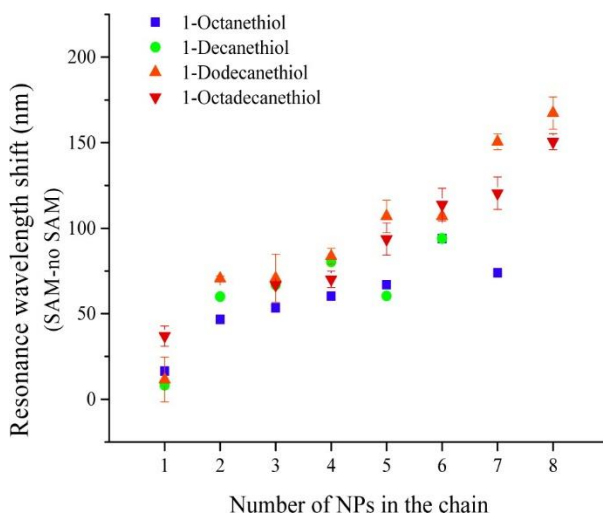


Figure 3.9 The plot of the DSPR peak shift upon SAM adsorption vs. the number of NPs in the chains ($d = 30$ nm).

Table 3.1 Coupling constant, A of square nanoparticle array samples with ~ 30 nm inter-particle distance indicating its value before and after SAM preparation. Increment in the coupling constant can be seen after SAM preparation.

Alkanethiol SAM	Coupling constant before SAM preparation (A_{Air})	Coupling constant after SAM preparation (A_{SAM})
Octanethiol	-0.309 ± 0.005	-0.331 ± 0.008
Decanethiol	-0.29 ± 0.02	-0.32 ± 0.01
Dodecanethiol	-0.261 ± 0.005	-0.307 ± 0.003
Octadecanethiol	-0.257 ± 0.007	-0.271 ± 0.002

3.5 CONCLUSION

In this work, the optical response of one dimensional chains of square shaped NPs fabricated using electron beam lithography have been investigated and compared with an analytical model. It was shown experimentally that under longitudinal polarization and at short inter-particle distances the chains exhibited a delocalized surface plasmon mode (DSPR). For a given interparticle distance, it was observed that the wavelength position of the DSPR initially red shifts with increasing number of NPs in the chain and reaches an asymptotic value. The application of the plasmon ruler equation to the square NP dimer gave rise to a longer characteristic decay constant than is reported for spherical or disk shaped NPs. This difference may reflect the influence of NP shape on the plasmon coupling.

An analytical expression based on a tight binding model was used to obtain a coupling constant for the interparticle coupling strength from the observed spectral shifts. The coupling constant displayed an $\sim d^{-0.42}$ distance dependence over the range of interparticle distances studied

here. This distance dependence is much stronger than that predicted by a point dipole model or van der Waals interaction models for different shaped NPs.

The sensitivity of the DSPR wavelength for molecular absorbates was found to be larger than that previously reported for LSPR modes of individual NPs and NP dimers; thus the large redshifts in the peak wavelength position of NP chains is a promising sensing strategy.

3.6 REFERENCES

- (1)Mayer, K. M.; Hafner, J. H.: Localized Surface Plasmon Resonance Sensors. *Chem. Rev.* **2011**, *111*, 3828-3857.
- (2)Anker, J. N.; Hall, W. P.; Lyandres, O.; Shah, N. C.; Zhao, J.; Van Duyne, R. P.: Biosensing with plasmonic nanosensors. *Nat Mater* **2008**, *7*, 442-453.
- (3)Willems, K. A.; Van Duyne, R. P.: Localized Surface Plasmon Resonance Spectroscopy and Sensing. *Annu. Rev. Phys. Chem.* **2007**, *58*, 267-297.
- (4)Lee, K.-S.; El-Sayed, M. A.: Gold and Silver Nanoparticles in Sensing and Imaging: Sensitivity of Plasmon Response to Size, Shape, and Metal Composition. *The Journal of Physical Chemistry B* **2006**, *110*, 19220-19225.
- (5)Slaughter, L. S.; Chang, W.-S.; Swanglap, P.; Tcherniak, A.; Khanal, B. P.; Zubarev, E. R.; Link, S.: Single-Particle Spectroscopy of Gold Nanorods beyond the Quasi-Static Limit: Varying the Width at Constant Aspect Ratio. *The Journal of Physical Chemistry C* **2010**, *114*, 4934-4938.
- (6)Mock, J. J.; Barbic, M.; Smith, D. R.; Schultz, D. A.; Schultz, S.: Shape effects in plasmon resonance of individual colloidal silver nanoparticles. *The Journal of Chemical Physics* **2002**, *116*, 6755-6759.
- (7)Mock, J. J.; Smith, D. R.; Schultz, S.: Local Refractive Index Dependence of Plasmon Resonance Spectra from Individual Nanoparticles. *Nano Letters* **2003**, *3*, 485-491.

- (8) Miller, M. M.; Lazarides, A. A.: Sensitivity of Metal Nanoparticle Surface Plasmon Resonance to the Dielectric Environment. *The Journal of Physical Chemistry B* **2005**, *109*, 21556-21565.
- (9) Burgin, J.; Liu, M.; Guyot-Sionnest, P.: Dielectric Sensing with Deposited Gold Bipyramids. *The Journal of Physical Chemistry C* **2008**, *112*, 19279-19282.
- (10) Banholzer, M. J.; Harris, N.; Millstone, J. E.; Schatz, G. C.; Mirkin, C. A.: Abnormally Large Plasmonic Shifts in Silica-Protected Gold Triangular Nanoprisms†. *The Journal of Physical Chemistry C* **2010**, *114*, 7521-7526.
- (11) Sherry, L. J.; Chang, S.-H.; Schatz, G. C.; Van Duyne, R. P.; Wiley, B. J.; Xia, Y.: Localized Surface Plasmon Resonance Spectroscopy of Single Silver Nanocubes. *Nano Letters* **2005**, *5*, 2034-2038.
- (12) Chen, H.; Kou, X.; Yang, Z.; Ni, W.; Wang, J.: Shape- and Size-Dependent Refractive Index Sensitivity of Gold Nanoparticles. *Langmuir* **2008**, *24*, 5233-5237.
- (13) Nehl, C. L.; Liao, H.; Hafner, J. H.: Optical Properties of Star-Shaped Gold Nanoparticles. *Nano Letters* **2006**, *6*, 683-688.
- (14) Mayer, K. M.; Lee, S.; Liao, H.; Rostro, B. C.; Fuentes, A.; Scully, P. T.; Nehl, C. L.; Hafner, J. H.: A Label-Free Immunoassay Based Upon Localized Surface Plasmon Resonance of Gold Nanorods. *ACS Nano* **2008**, *2*, 687-692.
- (15) Bukasov, R.; Shumaker-Parry, J. S.: Highly Tunable Infrared Extinction Properties of Gold Nanocrescents. *Nano Letters* **2007**, *7*, 1113-1118.
- (16) Link, S.; Mohamed, M. B.; El-Sayed, M. A.: Simulation of the Optical Absorption Spectra of Gold Nanorods as a Function of Their Aspect Ratio and the Effect of the Medium Dielectric Constant. *The Journal of Physical Chemistry B* **1999**, *103*, 3073-3077.
- (17) Svedendahl, M.; Chen, S.; Dmitriev, A.; Käll, M.: Refractometric Sensing Using Propagating versus Localized Surface Plasmons: A Direct Comparison. *Nano Letters* **2009**, *9*, 4428-4433.
- (18) Marinakos, S. M.; Chen, S.; Chilkoti, A.: Plasmonic Detection of a Model Analyte in Serum by a Gold Nanorod Sensor. *Anal. Chem.* **2007**, *79*, 5278-5283.
- (19) Haes, A. J.; Chang, L.; Klein, W. L.; Van Duyne, R. P.: Detection of a Biomarker for Alzheimer's Disease from Synthetic and Clinical Samples Using a Nanoscale Optical Biosensor. *J. Am. Chem. Soc.* **2005**, *127*, 2264-2271.
- (20) Zhao, J.; Das, A.; Schatz, G. C.; Sligar, S. G.; Van Duyne, R. P.: Resonance Localized Surface Plasmon Spectroscopy: Sensing Substrate and Inhibitor Binding to Cytochrome P450. *The Journal of Physical Chemistry C* **2008**, *112*, 13084-13088.

- (21) McFarland, A. D.; Van Duyne, R. P.: Single Silver Nanoparticles as Real-Time Optical Sensors with Zeptomole Sensitivity. *Nano Letters* **2003**, *3*, 1057-1062.
- (22) Sonnichsen, C.; Reinhard, B. M.; Liphardt, J.; Alivisatos, A. P.: A molecular ruler based on plasmon coupling of single gold and silver nanoparticles. *Nat Biotech* **2005**, *23*, 741-745.
- (23) Liu, N.; Weiss, T.; Mesch, M.; Langguth, L.; Eigenthaler, U.; Hirscher, M.; Sonnichsen, C.; Giessen, H.: Planar Metamaterial Analogue of Electromagnetically Induced Transparency for Plasmonic Sensing. *Nano Letters* **2009**, *10*, 1103-1107.
- (24) Hao, F.; Nordlander, P.; Sonnefraud, Y.; Dorpe, P. V.; Maier, S. A.: Tunability of Subradiant Dipolar and Fano-Type Plasmon Resonances in Metallic Ring/Disk Cavities: Implications for Nanoscale Optical Sensing. *ACS Nano* **2009**, *3*, 643-652.
- (25) Shen, Y.; Zhou, J.; Liu, T.; Tao, Y.; Jiang, R.; Liu, M.; Xiao, G.; Zhu, J.; Zhou, Z.-K.; Wang, X.; Jin, C.; Wang, J.: Plasmonic gold mushroom arrays with refractive index sensing figures of merit approaching the theoretical limit. *Nat Commun* **2013**, *4*.
- (26) Hao, F.; Sonnefraud, Y.; Dorpe, P. V.; Maier, S. A.; Halas, N. J.; Nordlander, P.: Symmetry Breaking in Plasmonic Nanocavities: Subradiant LSPR Sensing and a Tunable Fano Resonance. *Nano Letters* **2008**, *8*, 3983-3988.
- (27) Maier, S. A.; Brongersma, M. L.; Kik, P. G.; Atwater, H. A.: Observation of near-field coupling in metal nanoparticle chains using far-field polarization spectroscopy. *Physical Review B* **2002**, *65*, 193408.
- (28) Brandl, D. W.; Mirin, N. A.; Nordlander, P.: Plasmon Modes of Nanosphere Trimers and Quadrumers. *The Journal of Physical Chemistry B* **2006**, *110*, 12302-12310.
- (29) Brongersma, M. L.; Hartman, J. W.; Atwater, H. A.: Electromagnetic energy transfer and switching in nanoparticle chain arrays below the diffraction limit. *Physical Review B* **2000**, *62*, R16356-R16359.
- (30) Lassiter, J. B.; Sobhani, H.; Fan, J. A.; Kundu, J.; Capasso, F.; Nordlander, P.; Halas, N. J.: Fano Resonances in Plasmonic Nanoclusters: Geometrical and Chemical Tunability. *Nano Letters* **2010**, *10*, 3184-3189.
- (31) Fan, J. A.; Wu, C.; Bao, K.; Bao, J.; Bardhan, R.; Halas, N. J.; Manoharan, V. N.; Nordlander, P.; Shvets, G.; Capasso, F.: Self-Assembled Plasmonic Nanoparticle Clusters. *Science* **2010**, *328*, 1135-1138.
- (32) Luk'yanchuk, B.; Zheludev, N. I.; Maier, S. A.; Halas, N. J.; Nordlander, P.; Giessen, H.; Chong, C. T.: The Fano resonance in plasmonic nanostructures and metamaterials. *Nat Mater* **2010**, *9*, 707-715.

- (33) Zhang, Y.; Wen, F.; Zhen, Y.-R.; Nordlander, P.; Halas, N. J.: Coherent Fano resonances in a plasmonic nanocluster enhance optical four-wave mixing. *Proceedings of the National Academy of Sciences* **2013**, *110*, 9215-9219.
- (34) Quinten, M.; Leitner, A.; Krenn, J. R.; Aussenegg, F. R.: Electromagnetic energy transport via linear chains of silver nanoparticles. *Opt. Lett.* **1998**, *23*, 1331-1333.
- (35) Maier, S. A.; Kik, P. G.; Atwater, H. A.; Meltzer, S.; Harel, E.; Koel, B. E.; Requicha, A. A. G.: Local detection of electromagnetic energy transport below the diffraction limit in metal nanoparticle plasmon waveguides. *Nat Mater* **2003**, *2*, 229-232.
- (36) Citrin, D. S.: Coherent Excitation Transport in Metal–Nanoparticle Chains. *Nano Letters* **2004**, *4*, 1561-1565.
- (37) Solis, D.; Willingham, B.; Nauert, S. L.; Slaughter, L. S.; Olson, J.; Swanglap, P.; Paul, A.; Chang, W.-S.; Link, S.: Electromagnetic Energy Transport in Nanoparticle Chains via Dark Plasmon Modes. *Nano Letters* **2012**, *12*, 1349-1353.
- (38) Theiss, J.; Pavaskar, P.; Echternach, P. M.; Muller, R. E.; Cronin, S. B.: Plasmonic Nanoparticle Arrays with Nanometer Separation for High-Performance SERS Substrates. *Nano Letters* **2010**, *10*, 2749-2754.
- (39) Michaels, A. M.; Jiang; Brus, L.: Ag Nanocrystal Junctions as the Site for Surface-Enhanced Raman Scattering of Single Rhodamine 6G Molecules. *The Journal of Physical Chemistry B* **2000**, *104*, 11965-11971.
- (40) Wei, Q. H.; Su, K. H.; Durant, S.; Zhang, X.: Plasmon Resonance of Finite One-Dimensional Au Nanoparticle Chains. *Nano Letters* **2004**, *4*, 1067-1071.
- (41) Maier, S. A.; Kik, P. G.; Atwater, H. A.: Observation of coupled plasmon-polariton modes in Au nanoparticle chain waveguides of different lengths: Estimation of waveguide loss. *Applied Physics Letters* **2002**, *81*, 1714-1716.
- (42) Atay, T.; Song, J.-H.; Nurmikko, A. V.: Strongly Interacting Plasmon Nanoparticle Pairs: From Dipole–Dipole Interaction to Conductively Coupled Regime. *Nano Letters* **2004**, *4*, 1627-1631.
- (43) Jain, P. K.; Huang, W.; El-Sayed, M. A.: On the Universal Scaling Behavior of the Distance Decay of Plasmon Coupling in Metal Nanoparticle Pairs: A Plasmon Ruler Equation. *Nano Letters* **2007**, *7*, 2080-2088.
- (44) Aćimović, S. S.; Kreuzer, M. P.; González, M. U.; Quidant, R.: Plasmon Near-Field Coupling in Metal Dimers as a Step toward Single-Molecule Sensing. *ACS Nano* **2009**, *3*, 1231-1237.

- (45) Ueno, K.; Misawa, H.: Spectral properties and electromagnetic field enhancement effects on nano-engineered metallic nanoparticles. *Phys. Chem. Chem. Phys.* **2013**, *15*, 4093-4099.
- (46) Koenderink, A. F.; de Waele, R.; Prangma, J. C.; Polman, A.: Experimental evidence for large dynamic effects on the plasmon dispersion of subwavelength metal nanoparticle waveguides. *Physical Review B* **2007**, *76*, 201403.
- (47) Gunnarsson, L.; Rindzevicius, T.; Prikulis, J.; Kasemo, B.; Käll, M.; Zou, S.; Schatz, G. C.: Confined Plasmons in Nanofabricated Single Silver Particle Pairs: Experimental Observations of Strong Interparticle Interactions. *The Journal of Physical Chemistry B* **2004**, *109*, 1079-1087.
- (48) Su, K. H.; Wei, Q. H.; Zhang, X.; Mock, J. J.; Smith, D. R.; Schultz, S.: Interparticle Coupling Effects on Plasmon Resonances of Nanogold Particles. *Nano Letters* **2003**, *3*, 1087-1090.
- (49) Kofke, M. J.; Waldeck, D. H.; Walker, G. C.: Composite nanoparticle nanoslit arrays: a novel platform for LSPR mediated subwavelength optical transmission. *Opt. Express* **2010**, *18*, 7705-7713.
- (50) Barrow, S. J.; Funston, A. M.; Gómez, D. E.; Davis, T. J.; Mulvaney, P.: Surface Plasmon Resonances in Strongly Coupled Gold Nanosphere Chains from Monomer to Hexamer. *Nano Letters* **2011**, *11*, 4180-4187.
- (51) Chen, T.; Pourmand, M.; Feizpour, A.; Cushman, B.; Reinhard, B. M.: Tailoring Plasmon Coupling in Self-Assembled One-Dimensional Au Nanoparticle Chains through Simultaneous Control of Size and Gap Separation. *The Journal of Physical Chemistry Letters* **2013**, 2147-2152.
- (52) Harris, N.; Arnold, M. D.; Blaber, M. G.; Ford, M. J.: Plasmonic Resonances of Closely Coupled Gold Nanosphere Chains. *The Journal of Physical Chemistry C* **2009**, *113*, 2784-2791.
- (53) Willingham, B.; Link, S.: Energy transport in metal nanoparticle chains via sub-radiant plasmon modes. *Opt. Express* **2011**, *19*, 6450-6461.
- (54) Bouhelier, A.; Bachelot, R.; Im, J. S.; Wiederrecht, G. P.; Lerondel, G.; Kostcheev, S.; Royer, P.: Electromagnetic Interactions in Plasmonic Nanoparticle Arrays. *The Journal of Physical Chemistry B* **2005**, *109*, 3195-3198.
- (55) Zou, S.; Schatz, G. C.: Narrow plasmonic/photonic extinction and scattering line shapes for one and two dimensional silver nanoparticle arrays. *The Journal of Chemical Physics* **2004**, *121*, 12606-12612.
- (56) Palik, E. D.: Handbook of Optical Constants of Solids. Elsevier.
- (57) Zhang, S.; Bao, K.; Halas, N. J.; Xu, H.; Nordlander, P.: Substrate-Induced Fano Resonances of a Plasmonic Nanocube: A Route to Increased-Sensitivity Localized Surface Plasmon Resonance Sensors Revealed. *Nano Letters* **2011**, *11*, 1657-1663.

- (58) Mahmoud, M. A.; Chamanzar, M.; Adibi, A.; El-Sayed, M. A.: Effect of the Dielectric Constant of the Surrounding Medium and the Substrate on the Surface Plasmon Resonance Spectrum and Sensitivity Factors of Highly Symmetric Systems: Silver Nanocubes. *J. Am. Chem. Soc.* **2012**, *134*, 6434-6442.
- (59) Jain, P. K.; Eustis, S.; El-Sayed, M. A.: Plasmon Coupling in Nanorod Assemblies: Optical Absorption, Discrete Dipole Approximation Simulation, and Exciton-Coupling Model. *The Journal of Physical Chemistry B* **2006**, *110*, 18243-18253.
- (60) Kim, S. I.; Imura, K.; Kim, S.; Okamoto, H.: Confined Optical Fields in Nanovoid Chain Structures Directly Visualized by Near-Field Optical Imaging. *The Journal of Physical Chemistry C* **2010**, *115*, 1548-1555.
- (61) Krenn, J. R.; Dereux, A.; Weeber, J. C.; Bourillot, E.; Lacroute, Y.; Goudonnet, J. P.; Schider, G.; Gotschy, W.; Leitner, A.; Aussenegg, F. R.; Girard, C.: Squeezing the Optical Near-Field Zone by Plasmon Coupling of Metallic Nanoparticles. *Phys. Rev. Lett.* **1999**, *82*, 2590-2593.
- (62) Harrison, W. A.: *Applied quantum mechanics*; World Scientific: Singapore ; River Edge, N.J., 2000.
- (63) Zou, S.; Schatz, G. C.: Theoretical studies of plasmon resonances in one-dimensional nanoparticle chains: narrow lineshapes with tunable widths. *Nanotechnology* **2006**, *17*, 2813.
- (64) Hamaker, H. C.: The London—van der Waals attraction between spherical particles. *Physica* **1937**, *4*, 1058-1072.
- (65) Tabor, C.; Murali, R.; Mahmoud, M.; El-Sayed, M. A.: On the Use of Plasmonic Nanoparticle Pairs As a Plasmon Ruler: The Dependence of the Near-Field Dipole Plasmon Coupling on Nanoparticle Size and Shape†. *The Journal of Physical Chemistry A* **2008**, *113*, 1946-1953.
- (66) Arnold, M. D.; Blaber, M. G.; Ford, M. J.; Harris, N.: Universal scaling of local plasmons in chains of metal spheres. *Opt. Express* **2010**, *18*, 7528-7542.
- (67) Hill, R. T.; Mock, J. J.; Hucknall, A.; Wolter, S. D.; Jokerst, N. M.; Smith, D. R.; Chilkoti, A.: Plasmon Ruler with Angstrom Length Resolution. *ACS Nano* **2012**, *6*, 9237-9246.
- (68) Huang, F. M.; Wilding, D.; Speed, J. D.; Russell, A. E.; Bartlett, P. N.; Baumberg, J. J.: Dressing Plasmons in Particle-in-Cavity Architectures. *Nano Letters* **2011**, *11*, 1221-1226.
- (69) Ciraci, C.; Hill, R. T.; Mock, J. J.; Urzhumov, Y.; Fernández-Domínguez, A. I.; Maier, S. A.; Pendry, J. B.; Chilkoti, A.; Smith, D. R.: Probing the Ultimate Limits of Plasmonic Enhancement. *Science* **2012**, *337*, 1072-1074.
- (70) Yanik, A. A.; Cetin, A. E.; Huang, M.; Artar, A.; Mousavi, S. H.; Khanikaev, A.; Connor, J. H.; Shvets, G.; Altug, H.: Seeing protein monolayers with naked eye through plasmonic Fano resonances. *Proceedings of the National Academy of Sciences* **2011**, *108*, 11784-11789.

(71) Malinsky, M. D.; Kelly, K. L.; Schatz, G. C.; Van Duyne, R. P.: Chain Length Dependence and Sensing Capabilities of the Localized Surface Plasmon Resonance of Silver Nanoparticles Chemically Modified with Alkanethiol Self-Assembled Monolayers. *J. Am. Chem. Soc.* **2001**, *123*, 1471-1482.

(72) Jain, P. K.; El-Sayed, M. A.: Noble Metal Nanoparticle Pairs: Effect of Medium for Enhanced Nanosensing. *Nano Letters* **2008**, *8*, 4347-4352.

(73) Kinnan, M. K.; Kachan, S.; Simmons, C. K.; Chumanov, G.: Plasmon Coupling in Two-Dimensional Arrays of Silver Nanoparticles: I. Effect of the Dielectric Medium. *The Journal of Physical Chemistry C* **2009**, *113*, 7079-7084.

4.0 QUANTIFYING THE INTERACTION OF HIV CAPSID PROTEIN WITH LIPID RAFTS USING SURFACE PLASMON RESONANCE

The studies in this chapter were done in collaboration with Dr. Joanne Yeh group, Structural Biology Department, University of Pittsburgh. Thesis author conducted method development for lipid bilayer and raft preparation, fluorescence measurements, and data fitting. *Unpublished.*

This work reports on the interaction between HIV capsid proteins with lipid bilayer films containing sphingomyelin and cholesterol, measured using surface plasmon resonance technique. Specific binding of HIV capsid protein hexamer to the modified lipid bilayer film was quantified and analyzed with two different binding models. The full length capsid protein exhibited no interaction with the bilayer, indicating that the quaternary structure of the capsid proteins might be playing an important role during its interaction with the lipid rafts. Glycerol kinase exhibit no interaction with these membranes validating the observed interactions between HIV capsid protein hexamer and modified lipid membranes.

4.1 INTRODUCTION

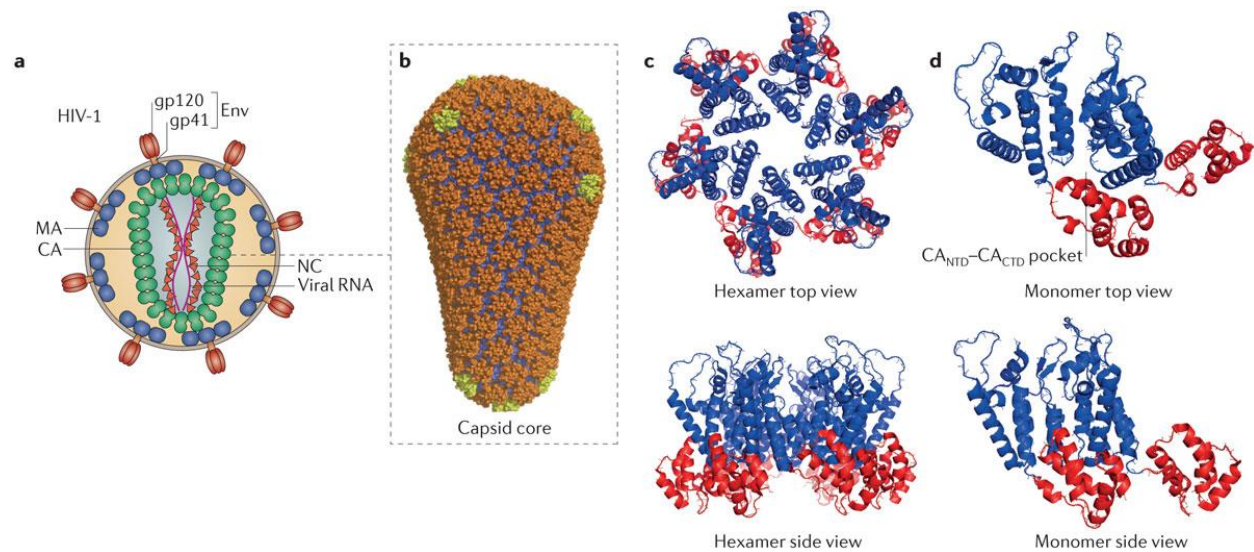
4.1.1 Role and Structure Human Immunodeficiency Virus Capsid Proteins

Human immunodeficiency virus (HIV) is a retrovirus that causes HIV infection and leads to depletion of specific cells in the immune system, resulting in immunodeficiency and thus vulnerability to opportunistic infections. The genome of a retrovirus, such as HIV, is composed of two single stranded ribonucleic acid (RNA) chains and along with the core proteins are encased in a protein shell termed the capsid.^{1,2} The virus uses a host cell for its replication, in which the RNAs are first transcribed to double standard DNA that is translocated into the host nucleus. The first phase of the viral replication cycle begins with the adhesion of virus to the host cell and fusion of the cell and viral membranes. Subsequently, the viral core is delivered into the cytoplasm, where the capsid gets disassembled to release the transcribed viral DNA. Cellular transcription results in synthesis of viral genomic RNA and proteins that assemble at the host cell plasma membrane for budding off as virions (virus particle).^{1,3} It has been long known that the HIV envelope is enriched with sphingolipids and cholesterol relative to the host plasma membrane suggesting that the viruses bud from specific plasma membrane microdomains where these lipids are more abundant than others.

The assembly process of the components of the virus at the plasma membrane is known to be mediated via a polyprotein precursor (Gag) that is cleaved into the mature proteins: the MA (matrix), CA (capsid), NC (nucleocapsid), and other viral proteins, subsequent to budding.^{1,4} After maturation CA proteins assemble into the conical capsid,¹ but interestingly, recent studies have shown that not all the molecules of CA are involved in capsid formation.⁵⁻⁷ Furthermore, CA proteins are also known to drive Gag multimerization during assembly.¹ It is not yet well

established whether the MA protein, which mediates membrane binding and insertion of envelope glycoproteins into the virions, is the only unique protein bound to membranes or where there are other lipid-binding proteins.⁶ Recent studies have shown the affinity of CA protein to several lipids.^{6,8} Thus a complete understanding of the lipid-binding processes requires a quantitative study of the several Gag produced proteins, including CA proteins and their domains in the presence of lipids. It can be speculated that the understanding of the role of these Gag proteins in the virus replication cycle is important, as they can provide potential drug targets because of their vital role in the virus life cycle.

As illustrated in Figure 4.1 HIV type 1, the most common pathogenic strain of the virus, is cone shaped and contains ~1500 copies of CA proteins arranged in a hexameric lattice. The body of the fullerene capsid is linked with ~ 250 CA hexamers, whereas the ends of the cone are capped by exactly 12 CA pentamers.^{1,9} Each full length CA protein is formed by two independently folded domains, the N-terminal domain (NTD) and C-terminal domain (CTD), connected by a flexible linker.^{1,9-11} When CA is assembled into pentamers and hexamers, each NTD is located on the outer surface of the capsid core and each CTD is oriented towards the interior of the structure. The NTD contains three α -helices, which stabilize the hexameric subunits of CA proteins. NTD-CTD contacts between adjacent CA monomers further stabilize the hexameric or pentameric subunits.³ Larger assemblies of hexamers and pentamers are held together by hydrophobic residues in the CTD, which provide the basis of the mature fullerene capsid core.



Nature Reviews | Microbiology

Figure 4.1 a) A Schematic representation of the mature HIV-1 virion, showing the viral glycoprotein envelope (Env, which is made of glycoprotein 120 (gp120) and gp41 subunits), as well as the Gag polypeptide-derived proteins matrix (MA), capsid (CA) and nucleocapsid (NC). The conical viral capsid core is assembled from CA hexamers and pentamers. The capsid core harbours the viral RNA genome, which is associated with NC. b) The conical capsid core assembles into a fullerene cone, containing hexameric (orange) and pentameric (yellow) CA subunits. c) Top view and side view of the hexameric subunits that form the primary capsid core of HIV-1. Interactions between the CA amino-terminal domain (NTD; blue) and the CA carboxy-terminal domain (CTD; red) of adjacent monomers stabilize the assembled hexamer. d) Structure of two CA monomers of a hexamer, illustrating the NTD-CTD pocket, which mediates interactions between CA and host cell proteins. This figure is taken from Reference 1.¹

4.1.2 Lipid Rafts

In the classical fluid mosaic description of a cell membrane, lipid bilayers are thought to form a two dimensional homogenous solvent that allows proteins to pass through freely.¹² This prevailing view has been modified since it was first proposed, as membrane compartmentalization is known to occur and arise from lipid-lipid, lipid-protein, and membrane-cytoskeleton interactions. Several types of microdomains exist in plasma membranes and lipid rafts are one such microdomain largely defined according to their insolubility in nonionic detergents.¹³⁻¹⁵ The lipid raft microdomains are known to be rich in sphingolipids and cholesterol, and the side chains of the phospholipids present are usually enriched with saturated fatty acids as compared to the surroundings.^{15,16} In contrast, nonraft regions of the cell membrane are known to contain glycerophospholipids that are rich in unsaturated chains where carbon chains are known to contain one or more *cis* double bonds.¹⁶ Most sphingolipids contain a single double bond in a *trans* configuration, located between the fourth and fifth carbon atoms of the 18-carbon sphingoid base. The presence of saturated fatty acid chains in sphingolipids allows them to pack tightly together through van der Waals interactions forming a gel like phase. On the other hand, the presence of polyunsaturated chains in glycerophospholipids hinders the close packing of the chains leading to a loosely pack disordered state referred to as a liquid-crystalline phase (L_d).

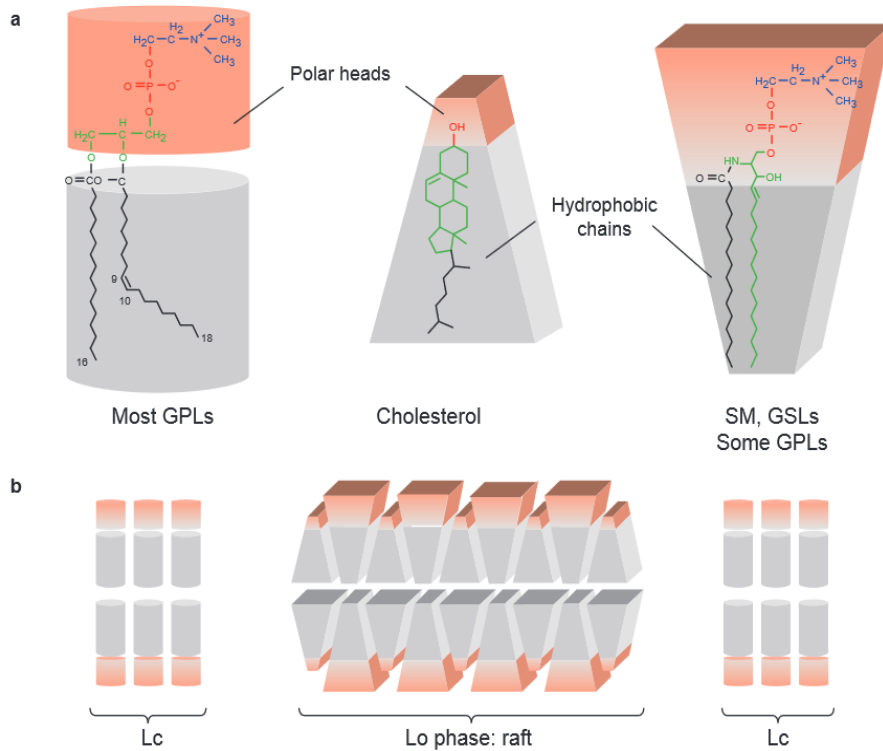


Figure 4.2 (a) Glycerophospholipids, which form the L_d phase of the plasma membrane, are roughly cylindrical; however, cholesterol and sphingolipids have a pyramidal or cone-like shape. In sphingolipids the polar head group occupies a larger area than does the hydrophobic region, whereas the converse is true for cholesterol. (b) Given the remarkable fit between the global shape of cholesterol and sphingolipids any void between associated sphingolipids is thought to be filled by cholesterol functioning as a molecular spacer. The enrichment of cholesterol in L_o phase domains is consistent with this model. This Figure is adapted from reference 16.¹⁶

These structural features explain the differential packing capabilities in the glycerophospholipids and sphingolipids, which leads to their phase separation in the plasma membrane. Cholesterol has been shown to preferentially intercalate in between sphingolipids in a way to fill void spaces associated with the sphingolipid molecules acting as a spacer molecule. The close interaction between cholesterol and sphingomyelin has been demonstrated in various reconstituted membrane systems. Owing to the presence of cholesterol, sphingolipids adopt a tight packed liquid ordered phase (L_o). It has also been proposed that cholesterol might localize along the border between raft sphingolipids and glycerophospholipids, which could create an energy-favorable transition area between L_o and L_d phases in the plasma membrane

Planar supported lipid layers and giant unilamellar vesicles are the widely used model systems for studying lipid rafts. Several methods have been utilized to study lipid rafts and associated membrane proteins. The traditional method of using detergent resistance as an indicator as to the presence of lipid rafts have been criticized because detergents themselves can induce phase separation and partitioning of proteins.^{17,18} Therefore a variety of other methods have been developed to study the phase behavior of the model or native membrane and their association with proteins *in situ*. Methods such as mass spectrometry can be used to study the lipid composition directly on the sample.^{19,20} But since the samples need to be freeze dried and measurements are performed under high vacuum conditions, this method limits the direct probing of protein interaction with lipid rafts. Another widely used method is fluorescence microscopy.^{21,22} This method allows direct probing of lipid rafts in model membranes, as well as living cells and raft-protein interactions but it is limited by the availability of fluorescent labels that are capable of selectively partitioning into membrane domains.²² Also fluorescence tagging of the proteins may introduce structural features that may prevent them from mimicking the types of biological

interactions under study. Other widely used methods for probing lipid rafts include AFM^{23,24} and NMR,^{25,26} but they are limited to model membranes and cannot be used to directly detect raft protein interactions. In contrast to these prevailing methods, in the present study the surface plasmon resonance technique is used to directly probe the lipid immobilization and protein interaction in model lipid raft membranes.

4.1.3 **BIAcore Surface Plasmon Resonance Instrument**

The surface plasmon resonance instrument, Biacore SPR (GE instruments) uses excitation of the propagating surface plasmon in a 50 nm thin Au film. Light wavelength of 760 nm is utilized for SPR excitation in a Kretschman configuration (see section 1.1.1). In the instrument, the Au film makes the floor of a microfluidic flow cell through which a solution containing an analyte is allowed to flow. As the analyte binds to ligands that are immobilized on the Au surface, they accumulate and cause a change in the local refractive index. This change in local refractive index changes the phase matching condition for surface plasmon excitation, i.e., the angle of the minimum in total internal reflection intensity. The reflected intensity is monitored in real time and the result is plotted as response or resonance units (RUs) versus time (a sensorgram). At the same time, a response can occur because of the change in the refractive indices between of the sample solution and running buffer. In order to account for this background signal, a reference flow cell which does not contains the relevant ligand for analyte binding is used. One RU is equivalent of 10^{-6} refractive index units (RIU), which makes this technique extremely sensitive to any changes in the local refractive index.²⁷

The fact that this instrument produces real time data makes it well suited for studying real time binding kinetics. In a typical ligand-analyte binding study, the ligand molecules are usually immobilized on the sensor surface first. Then the analytes are allowed to flow across the ligand surface, during which analytes are associated with the ligands on the surface. After, the analyte injection is stopped, a buffer is flowed through the cell and it triggers dissociation of the analyte from the ligand.

In the present study, a BIAcore SPR is used to monitor the interaction between the capsid proteins, full length capsid and capsid hexamer, and supported bilayer that are modified with sphingomyelin and cholesterol. Real time kinetic interactions were performed and binding constants were calculated with existing models. The collected data suggests a specific interaction of Capsid hexamer with lipid membranes but no such specificity was observed for the full length capsid. These results highlight the interaction between capsid proteins with lipid rafts, which could be a potential drug target for the HIV virus.

4.2 EXPERIMENTAL METHODS

4.2.1 Substrate Preparation

Substrates for these experiments were prepared by e-beam evaporation (AJA Deposition System) of a 50 nm thin film of Au on glass substrates that are supported by a 5 nm Ti layer. Glass substrates with 0.1 mm thicknesses were used for SPR experiments. The surface roughness of these substrates was found to be 0.7 ± 0.1 nm using AFM imaging. All substrates were cleaned either using an oxygen plasma or piranha solution prior to the experiment.

4.2.2 Lipid Solution Preparation

Lipids, 1,2-dipalmitoyl-sn-glycero-3-phosphoethanolamine (DPPE), 1,2-distearoyl-sn-glycero-3-phosphocholine (DSPC), Sphingomyelin (SM), and Cholesterol (CH) were purchased from Avanti Polar Lipids Inc. and used without further purification. Chemical reagents for the amine coupling reaction (N-hydroxysulfosuccinimide) (sulfo-NHS) and N-(3-dimethylaminopropyl)-N-ethylcarbodiimide hydrochloride (EDC) were purchased from Sigma Aldrich and used without any further purification. Surfactants, n-octyl- β -D-glucoside (OG) and n-Dodecyl β -D-maltoside (DM), were purchased from Sigma Aldrich.

A lipid (DSPC and DPPE) stock solution was prepared by first dissolving DSPC in ethanol and then drying it under a stream of nitrogen. PBS (phosphate buffered saline, 20 mM sodium phosphate and 150 mM KCl) was added to obtain a final concentration of 5 mg/ml and this solution was sonicated for 5 min. The solution was subjected to 6 freeze thaw cycles. These solutions were stored at -80 °C and prior to their use in experiments, the lipid solutions were passed through a 0.2 micron filter five times at room temperature.

4.2.3 Lipid Bilayer Preparation

The procedure for lipid bilayer preparation was adapted from the literature with some modification.²⁸ The substrates were immersed in 1 mM 4-mercaptobenzoic acid (4-MBA) in ethanol overnight to form a self-assembled monolayer (SAM). Substrates were then washed with copious amount of ethanol to remove any impurities. The thickness of the 4-MBA layer was monitored by ellipsometry. These 4-MBA modified substrates were immersed in a freshly prepared solution of 0.4 M EDC and 0.1 M sulfo-NHS for 10 min for surface activation. The

substrates were washed with PBS buffer and immersed in DPPE for 30 min, to be covalently bound to a 4-MBA SAM. The substrates were then incubated in different concentrations of DSPC solutions for varying time periods of lipid bilayer formation. The thickness of these mixed DSPC-DPPE bilayer films was measured using ellipsometry and AFM.

4.2.4 In situ Lipid Bilayer Preparation in BIAcore

A similar procedure to that described above was used for in situ preparation of mixed lipid bilayer films in the BIAcore SPR instrument. First, the Au substrates were immersed in 1 mM 4-mercaptobenzoic acid (4-MBA) in ethanol overnight to form a self-assembled monolayer (SAM). Then the 4-MBA modified chips were attached to the support to be inserted into the Biacore 3000 so that the DSPC-DPPE (1,2-dihexadecanoyl-sn-glycero-3-phosphoethanolamine) mixed bilayer formation was monitored in real time.

A freshly prepared mixture of 0.4 M EDC and sulfo-NHS of 0.1 M concentration was injected at 5 μ l/min for 10 min to activate the carboxyl groups on the surface. Then it was washed with a buffer of 20 mM PBS (pH 7.5). After washing, 1 mg/ml (1.45 mM) DPPE in 20 mM PBS was injected at 5 μ l/min for 30 min to covalently bind to the 4-MBA SAM. Subsequently the chip was washed with PBS buffer. DSPC at different concentrations were prepared in 20 mM PBS (pH 7.5) and injected at 5 μ l/min for 30 min to form the DSPC-DPPE mixed lipid bilayer. 3 min injections of 40 mM OG at 5 μ l/min was performed to regenerate the surface.

4.2.5 **In Situ Lipid Raft Preparation**

A sphingomyelin (SM) stock solution was prepared at 5 mg/ml in ethanol. A 0.1 ml aliquot of SM stock solution was purged with a stream of nitrogen and 20 mM PBS (pH 7.0) and 0.05 mM n-Decyl- β -D-maltopyranoside (DM) was added to make a 1 mg/ml concentration of SM. The cholesterol (CH) stock solution was prepared at 15 mg/ml in chloroform and 0.2 ml of the stock solution was purged with N₂. A 20 mM PBS (pH 7.0) and 0.05 mM DM was used to dilute CH to a final concentration of 1 mg/ml. The SM and CH solution were mixed at a molar ratio of 5:2 and 5:3 separately. These SM: CH mixtures were injected onto the lipid bilayers in the BiAcore instrument at a rate of 5 μ l/min for 30 min for lipid raft preparation.

4.2.6 **The Interaction of Capsid Proteins to SM-CH Raft**

A full length capsid (FLCA) was expressed and purified by the Yeh group according standard protocols developed by their group.¹⁰ The cross linked capsid hexamer (CAH) was prepared by the Aiken lab.²⁹ These proteins were diluted to different concentrations and injected at a 10 μ l/min rate onto the SM-CH modified channels for 3 min to enable association with the lipid film on the substrate. After 3 min of injection of the analyte, the phosphate buffer (pH 7.5) was injected for 5 min for dissociation phase monitoring.

4.2.7 **Atomic Force Microscopy Characterization**

AFM measurements were performed with an Agilent 5500 atomic force microscopy system using silicon cantilevers with a resonance frequency of 42-58 kHz and a spring constant of 0.15-

0.45 N/m (qp-BioT-20, Nanosensors) in deionized water. Precise values of the spring constants were determined using a thermal oscillation technique.³⁰ The bilayer film thickness was determined from the difference in the average height of the substrate covered with the lipid bilayer film and the bare gold substrate. The gold surface was exposed by scraping off the bilayer film in a 200 nm by 200 nm square area by performing a single AFM scan in a contact mode with an applied load force of ca. 20 nN. Following this procedure, a larger 1 μm by 1 μm square area was imaged in acoustic AFM mode to capture the original bilayer film together with the exposed gold substrate area. Switching between AFM operating modes was performed with a fully contracted z-axis piezoelement (the tip and the substrate were out of contact).

4.2.8 Fluorescence Recovery after Photobleaching (FRAP)

The diffusion coefficient of lipids in the prepared bilayer films were determined by the FRAP technique. The lipid bilayer films for this experiments were prepared similar to the method described in section 4.2.1 on Au films, but in the step where the substrates were incubated 0.5 mg/ml DSPC, 1mol % of the fluorescent lipid, L- α -Phosphatidylethanolamine-N-(lissamine rhodamine B sulfonyl) (ammonium salt) (RhB-PE, Avanti Polar Lipids) was added to the solution. As prepared lipid bilayer films were imaged with a confocal fluorescence microscope (Olympus FV1000 Fluoview) under 10x water immersion objective. A diode pumped solid state (DPSS) laser emitting at 559 nm wavelength was used for excitation of the RhB-PE in-cooperated to the lipid bilayer film. A fraction of 0.5% of the 15 mW power of the laser was used for imaging. Photobleaching was carried out using 100 % of the laser power at a circular area with a diameter of 7.95 μm for a duration of 1 s. The fluorescent recovery of the bleached area was monitored in intervals of 15 s for 10 min, using a 575 nm - 625 nm band pass filter.

4.3 RESULTS AND DISCUSSIONS

4.3.1 Lipid Bilayer Preparation

The procedure for layer-by-layer assembly of lipid bilayer films on a Au surface is illustrated in Figure 4.1. The membrane architecture is prepared in three steps: i) self-assembly of a 4-MBA spacer group on Au; ii) covalent coupling of DPPE to 4-MBA; and iii) DSPC vesicle spreading to form the complete lipid bilayer.

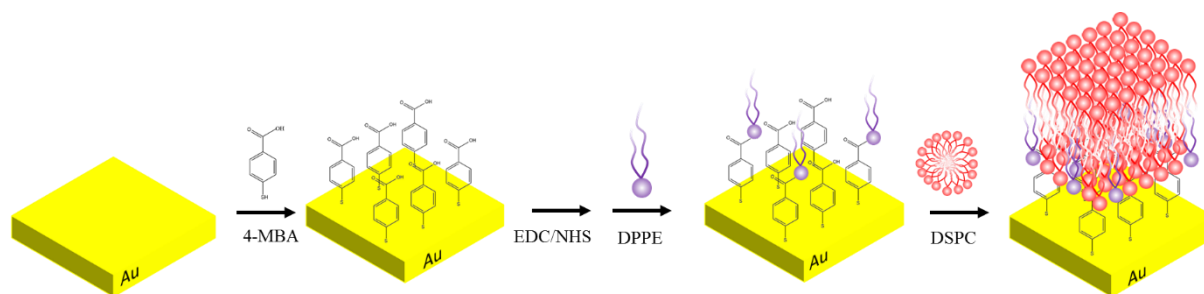


Figure 4.3 The schematic diagram illustrates the process used for the assembly of DSPC-DPPE mixed lipid bilayer films on Au substrates. (Not drawn to scale).

Characterization of the 4-MBA spacer group thickness was done using ellipsometry and the thickness was found to be 1.62 ± 0.07 nm. The mixed DSPC-DPPE bilayer thicknesses that were obtained using ellipsometry, while changing the incubation time and DSPC concentration, are depicted in Figure 4.4 (a). In this graph, the dashed line indicates the expected total film thickness of the bilayer film including the 4-MBA spacer layer. It was found that incubating in 0.5 mg/ml DSPC for 1 hr gave an average thickness that was equivalent to that expected for a lipid bilayer film. In order to further confirm successful lipid bilayer formation, aqueous medium AFM imaging was performed on bilayer films prepared using these optimized conditions. The AFM tip

was used to clear the bilayer film in a 0.5 micron square area on the image by scanning in contact mode with a 20 nN tip force. Then tapping mode was used to image the bilayer surface surrounding the scratch as illustrated in Figure 4.4 (b). The average z height distribution between the scratched area and the bilayer film indicates a 6 ± 2.2 nm difference, further confirming the successful bilayer film preparation conditions.

During in situ preparation of lipid bilayer films, the SPR recording was done in full scan mode to obtain the thickness after each of the subsequent steps in the assembly process. The shift in RU in SPR is caused by the introduction of a new layer with a thickness (d) that has been calculated using Equation 4.1.

$$RIU = \frac{\Delta RU}{1000000} = (n_{layer} - n_{buffer}) \times (1 - e^{-\frac{2d}{l}}) \quad \text{Equation 4.1}$$

Here n_{layer} and n_{buffer} are the bulk refractive indices of the lipid layer and the buffer, respectively. The characteristic plasmon decay length (l) of the 50 nm Au film, was found to be around 250 nm from the literature.³¹ Upon injection of DPPE, the refractive index response of the system shifted to a higher value and this change is shown in Figure 4.5 (a). The mean thickness of the DPPE layer was calculated to be 0.48 nm by using Equation 4.1. The mean coverage of 18.9% of DPPE molecules on the surface was calculated using an estimated length for the DPPE (1.8 nm) along with its monolayer thickness of 2.55 nm.³²

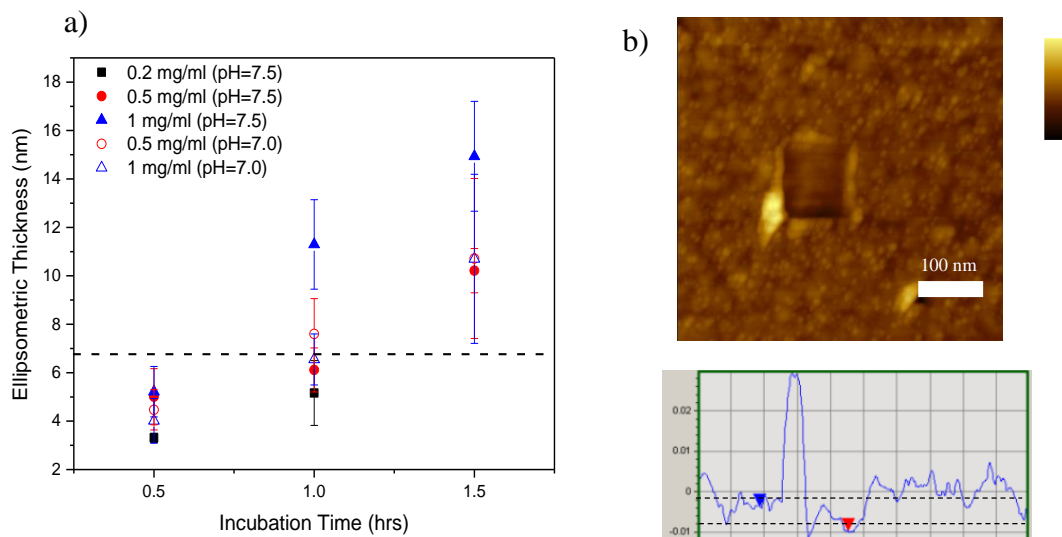


Figure 4.4 Panel (a) plots the measured ellipsometric thickness obtained for DSPC-DPPE mixed lipid bilayer films against the incubation time while changing the DSPC concentration and pH. The closed and open symbols correspond to bilayer formation at pH 7.5 and 7.0, respectively. In panel (b), an AFM image is shown for a lipid bilayer film, obtained while incubating for 1 hr in 0.5 mg/ml DSPC lipid solution at pH 7.0 is shown. The height difference between the scratched window in the image and the surrounding of the image is 6 ± 2 nm.

The formation of the DPPE-DSPC mixed bilayer was monitored by the change in the net RIU upon injecting different concentrations of DSPC over different time periods, ranging from 30 minutes to 2 hr. The dependence of the lipid bilayer formation on the DSPC concentration and time is illustrated in Figure 4.5(b). The dashed line indicates the expected bilayer thickness and the error bars on the data points are the standard deviation of measurements in four separate channels on the sample.

By comparing all the different bilayer thickness measurement methods, the optimal incubating conditions for successful lipid bilayer film formation were determined to be 1 hr

incubation in 0.5 mg/ml concentration of DSPC. The dynamic preparation of lipid bilayer films *in situ* in SPR

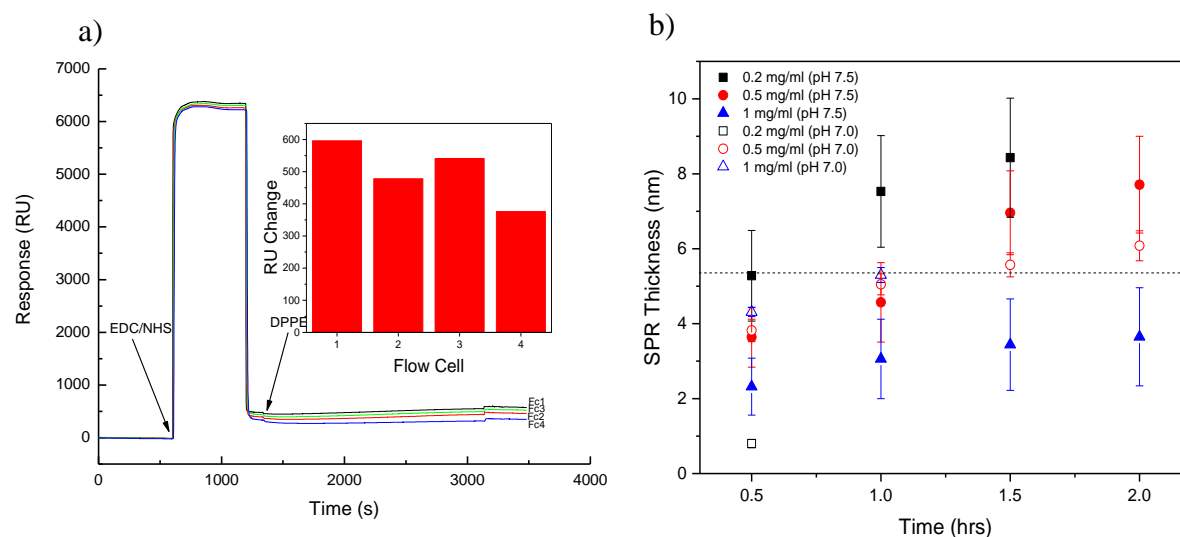


Figure 4.5 Panel a shows the response change during the immobilization of DPPE on a 4-MBA modified gold chip. The net RU change due to immobilization of DPPE is given in the table in the inset. Panel b shows a plot of the SPR thickness change with time for different concentrations of DSPC. Open and closed symbols represent different pH values of the DSPC lipid solution, pH 7.0 and 7.5, respectively.

The fluorescence recovery after photobleaching (FRAP) technique was utilized to estimate the diffusion coefficient of the DSPC lipid bilayer film prepared under optimized conditions. For this purpose, a 1 mol % of Rh-B PE fluorescent lipid was incorporated into the film. The absorption and emission spectra of the RhB is shown in the Figure 4.6(a). A diode laser of 559 nm was used for the excitation and the emission was collected using 575- 625 nm band pass filter. The spot size of the laser beam that was sent through the water immersion x10 objective was calculated to be 0.545 μm . The emission in the 7.95 μm area that was photobleached was collected and plotted in

Figure 4.6(b). Assuming that the only form of mobility during the recovery is by diffusion and a Gaussian beam laser profile for the bleaching, the fluorescence intensity (F_K) can be described by the Equation 4.2.³³

$$F_K(t) = A \sum_{n=0}^{15} \left[\frac{(-K)^n}{n!} \right] \left[1 + n \left(1 + \frac{2t}{\tau_D} \right) \right]^{-1} \quad \text{Equation 4.2}$$

In the above equation, A is the fluorescence intensity before bleaching and t is the time after photobleaching. The parameter K is the rate constant for the irreversible first order photobleaching reaction. The constant τ_D is the recovery time, which is can used as follow to calculate the diffusion coefficient (D).³⁴

$$D = \frac{w^2}{4\tau_D} \quad \text{Equation 4.3}$$

Here w is the width of the bleached area. Using the above relationship, a diffusion coefficient for DSPC bilayer film was calculate to be $0.107 \pm 0.004 \mu\text{m}^2\text{s}^{-1}$. Similar numbers have been reported for the diffusion coefficient of lipid bilayers conatining DSPC measured using FRAP method.³⁵

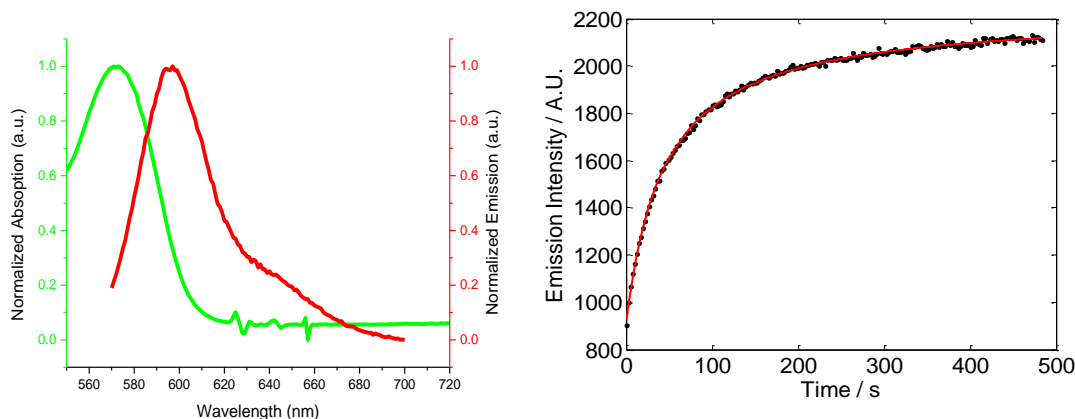


Figure 4.6 The normalized absorbance (green) and emission (red) spectra of the Rh-B PE is shown in panel (a). In panel (b) solid black squares illustrates the recovery of emission intensity collected by a 575- 625 nm band pass filter after photobleaching. The solid red line is the fit of the equation 4.4 (a) to the collected data.

4.3.2 Lipid Raft Preparation

Lipid rafts were prepared by injecting different ratios of SM:CH onto sample channels in the BIAcore and allowing the SM:CH mixture to titrate into the lipid bilayer film for 30 min. A net increment in the RIU response was observed and this change was assigned to immobilization of SM and CH molecules onto the lipid bilayer film. The number of molecules immobilized were calculated according to the response change and are reported in the Table 4.1. The titrated SM and CH molecules are thought to form lipid rafts during the immobilization process.

Table 4.1 Immobilized sphingomyelin and cholesterol as a percentage of bilayer lipid composition

SM:CH	DSPC-DPPE (mole)	SM-CH rafts (mole)	Percentage of rafts (%)
5:2	6.50×10^{-12}	0.21×10^{-12}	3.23
5:3	7.88×10^{-12}	0.13×10^{-12}	1.65

4.3.3 Interaction of Full Length Capsid with Lipid Rafts

The net response change while injecting full length capsid protein (FLCA) on to sample channels as compared to an unmodified reference channel, is depicted in Figure 4.7, where panels (a) and (b) correspond to sample channels modified with 5:2 and 5:3 ratios of SM:CH. No net change in RIU response can be noted indicating that FLCA has no affinity to lipid films modified with SM and CH.

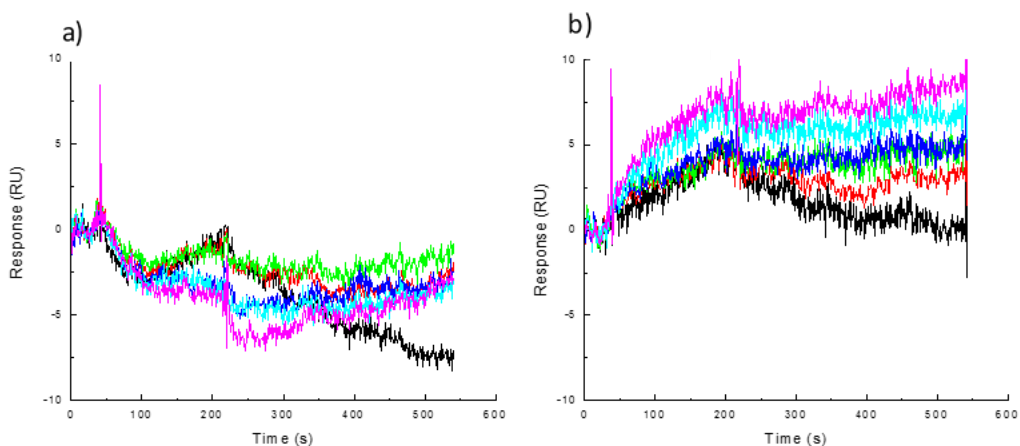


Figure 4.7 The plots corresponds to the response change after FLCA injection onto lipid bilayer films that are modified with (a) 5:2 and (b) 5:3 ratios of SM:CH.

4.3.4 Interaction of Capsid Hexamer with Lipid Rafts

Figure 4.8 illustrates the SPR sensorgrams obtained during the CAH interaction study, where sample channels were modified with 5:2 (Figure 4.5 (a)) and 5:3 (Figure 4.5 (b)) ratios of SM: CH. The CAH were diluted to different concentrations, ranging from 3.3 nM to 300 nM, and were injected to the SM-CH modified channels and reference channel. The reference channel was

left unmodified (no SM or CH) to determine the net binding of CAH to the lipid bilayer. The RU response in the sensorgrams were obtained by subtracting the response of the reference channel from that of the sample channels to give the net response of the CAH binding that arises because of SM-CH modification. The larger response observed for the modified channels indicates that there is a preference for the CAH to bind to lipid bilayers with SM and CH. It is also interesting to note that channels modified with a 5:3 ratio of SM: CH had a larger response as compared to channels with a 5:2 ratio. Channels modified with a SM: CH 5:1 ratio exhibited no net response during the interaction study and no further analysis was performed on the data collected on these channels.

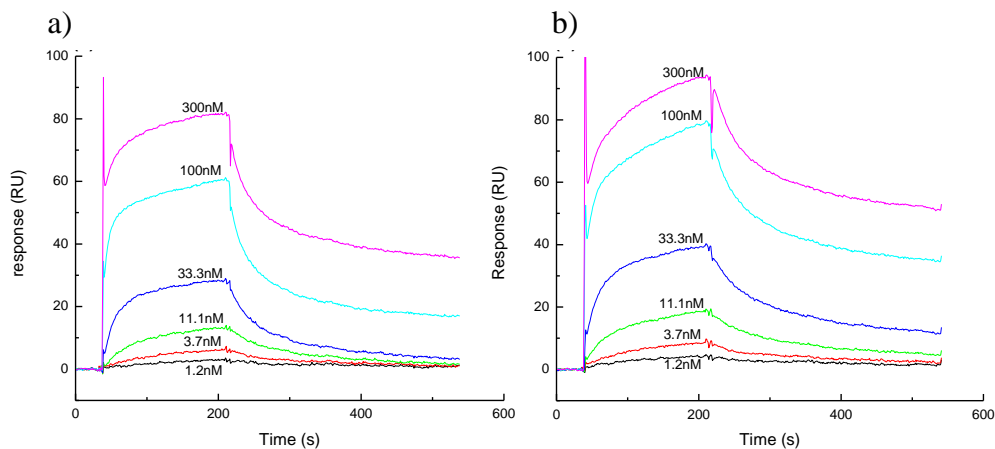


Figure 4.8 The response change of CAH binding on SM-CH rafts at different ratios of 5:2 (a) and 5:3 (b) are shown.

4.3.5 Interaction of Glycerol Kinase with Lipid Rafts

Glycerol kinase (GK) is a key enzyme in the regulation of glycerol uptake and metabolism, and located in the outer mitochondrial surface inside the cell.³⁶ Since the protein associated with lipid rafts are mostly structural and signaling proteins,³⁷ GK was used in this experiment to detect any non-specific binding onto SM-CH modified bilayer membranes. As illustrated in Figure 4.6 it can be seen that the response of the sample channels modified with 5:2 (see Figure 4.6 (a)) and 5:3 (Figure 4.6(b)) SM:CH ratios exhibit a minimal change with respect to that of the reference channel after injection of increasing concentrations of GK. This observation confirms that the nonspecific binding onto lipid bilayer films modified with SM-CH are similar to unmodified ones and that the response observed during the interaction study likely arises from specific binding of the CAH to SM-CH modified surfaces.

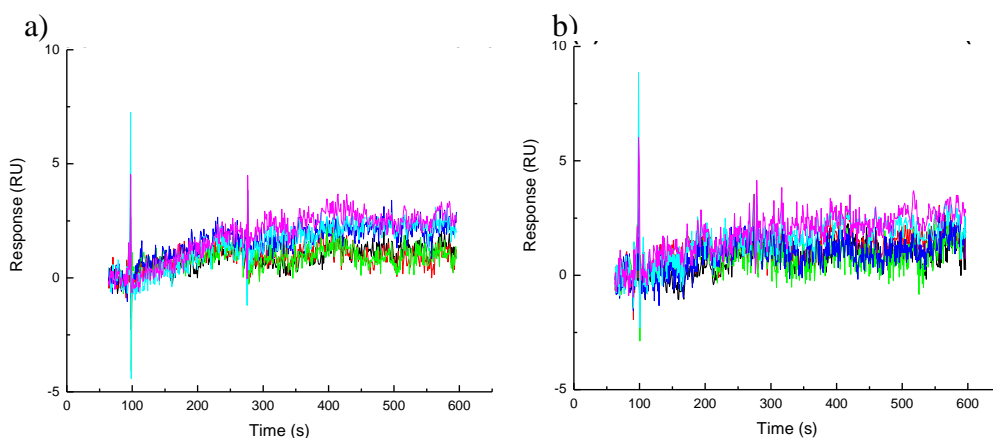


Figure 4.9 The sensorgrams of glycerol kinase (GK) to SM-CH rafts are shown for different ratios of 5:2 (A) and 5:3 (B) in 20 mM sodium phosphate (pH 7.0), 150 mM KCl. The concentrations of GK used were 1.2, 3.7, 11.1, 33.3, 100 and 300 nM (0.069, 0.21, 0.62, 1.9, 5.6 and 16.8 mg/mL).

4.3.6 Quantifying the Binding Affinity of CAH to modified Lipid Membranes

Affinity is the strength of binding of the analyte to its binding site. It is typically measured and reported by the equilibrium dissociation constant (K_D), which is used to evaluate and rank order strengths of bimolecular interactions. As with most biological interactions, the binding of the CAH protein to the raft is assumed to be a reversible process and the rate of the binding reaction is proportional to the concentrations of the reactants. The fact that the BIAcore SPR generates real time binding data makes it well suited for analysis of binding kinetics. Since the exact mechanism of the CAH protein binding to lipid rafts is still unknown, the data can be used to obtain affinity constants for the interaction.

The first model that was used to derive binding constants is the simple Langmuir 1:1 model ($A + L \leftrightarrow AL$). It assumes that the binding surface is homogenous and all the binding sites, which are the lipid rafts (L) are equivalent. Analyte, in this case the CAH (A), is considered monovalent and the binding events are considered to be independent. In the association phase of the interaction, CAH protein of different concentrations were injected onto the sample and reference channels. In this phase, the concentration of the CAH was kept under steady state and therefore they drive the equilibrium forward. In this limit the following relationship describes the rate of CAH-raft complex (AL) formation during the association phase of the 1:1 interaction.

$$\frac{dC_{AL}}{dt} = k_a C_A^0 [C_L^0 - C_{AL}] - k_d C_{AL}$$

Equation 4.4

In Eqn 4.3, C^0 is the initial concentration and C is the concentration at a given time of the species of interest. The term $[C_L^0 - C_{AL}]$ describes the concentration of unbound lipid rafts on the surface.

The symbols k_a and k_d give the association and dissociation rate constants, respectively. Integration of the above relationship leads to the expression given in Equation 4.4, where the RU response obtained during the interaction, which is directly related to the amount of AL complexes, can be used to calculate the k_a and k_d . RI is the background signal.

$$RU_{association} = C_{AL} = \frac{C_A^0(1 - e^{-(C_A^0 k_a + k_d)(t-t_0)})k_a C_L^0}{C_A^0 k_a + k_d} + RI \quad \text{Equation 4.5}$$

$$RU_{association} = R_{eq}(1 - e^{-\frac{t-t_0}{\tau_{2}}}) + RI \quad \text{Equation 4.6}$$

$$\text{where, } R_{eq} = \frac{C_A^0 k_a C_L^0}{C_A^0 k_a + k_d} \quad \text{and,} \quad \tau_{2} = \frac{1}{C_A^0 k_a + k_d}$$

In order to find the value of K_a from the response described by Equation 4.4, the values for k_d must be obtained by evaluating the dissociation phase of the sensorgram. During the dissociation phase of the interaction study, injection of the CAH was stopped and the PBS buffer was allowed to circulate through the channels. With no A present, the AL complex dissociates and the rate of the dissociation can be expressed by following equation.

$$\frac{dC_{AL}}{dt} = -k_d C_{AL} \quad \text{Equation 4.7}$$

$$RU_{dissociation} = C_{AL} = R_0 e^{-\frac{t-t_0}{\tau_{1}}} + RI \quad \text{Equation 4.8}$$

$$\text{where, } \tau_{1} = \frac{1}{k_d}$$

Figure 4.10 depicts the fit of the dissociation and association phases according to the model described above for two SM: CH ratios studied. A goodness of the fitting was obtained by calculating the χ^2 , according to following relationship.

$$\chi^2 = \sum_1^n \frac{(RU_{fitting} - RU_{data})^2}{RU_{data}} \quad \text{Equation 4.9}$$

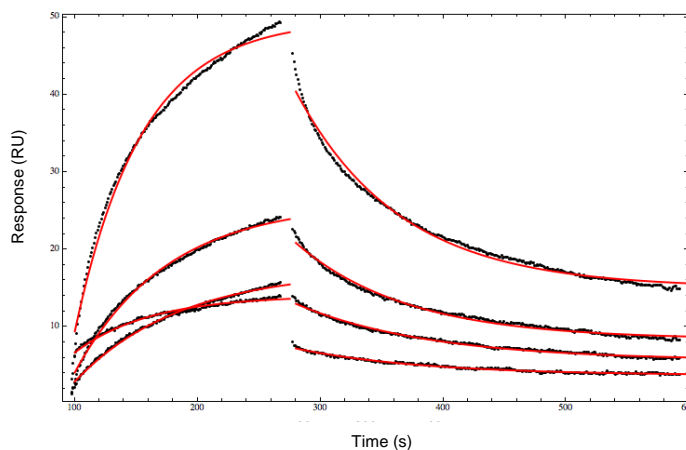


Figure 4.10 A fit of the Langmuir 1:1 model (red solid line) to the data collected (black solid symbols) during the interaction between CAH and lipid bilayer modified with 5:2 SM:CH ratio is shown. Table 4.1 at the bottom indicates the fitted parameters.

Table 4.2 Fitted parameters of the data on the Figure 4.9 to Langmuir model

[CAH] / M	$k_a / M^{-1} s^{-1}$	k_d / s^{-1}	K_D / M	C_0^L / RU	χ^2_{Ass}	χ^2_{Diss}
1.20×10^{-9}	7.75×10^5	6.77×10^{-3}	8.73×10^{-9}	3.71×10^1	0.054	0.074
3.70×10^{-9}	5.92×10^5	9.86×10^{-3}	1.67×10^{-8}	3.84×10^1	0.079	0.083
1.11×10^{-8}	6.53×10^5	1.16×10^{-2}	1.78×10^{-8}	3.61×10^1	0.082	0.11
3.33×10^{-8}	6.50×10^5	1.57×10^{-2}	2.41×10^{-8}	4.10×10^1	0.62	0.389
1.00×10^{-7}	1.05×10^5	1.92×10^{-2}	1.82×10^{-7}	5.81×10^1	1.76	1.09
3.00×10^{-7}	1.88×10^4	1.84×10^{-2}	9.82×10^{-7}	1.01×10^2	2.39	1.80

The change in binding of CAH to lipid bilayers modified with different SM: CH ratios indicate that the relative amount of the species in lipid bilayers plays a crucial role in the binding event. Table 4.2 summarizes all the parameters obtained from fitting the data in Figure 4.10. A good fit to the data at lower analyte concentrations by the model indicates that the binding can be described by 1:1 interaction between the capsid hexamer protein and the rafts in this concentration range for both SM: CH ratios studied. It can be also noted that the residual error is slightly larger at higher concentrations of CAH for both the 5:2 and 5:3 cases.

At equilibrium, the rate of CAH-raft complex formation is equal to the rate of dissociation into its components [L] + [A]. The association and dissociation rate constants obtained from the fitted data can be used to calculate the dissociation constant (K_D). K_D is the ratio of the analyte dissociation rate (k_d), how quickly it dissociates from its binding site, to the analyte association rate (k_a) of the CAH, how quickly it binds to the lipid raft. The K_D values listed in Table 4.2 were determined by taking the ratio between the k_a and k_d rates according to following equation.

$$K_D = \frac{C_A C_L}{C_{AL}} = \frac{k_d}{k_a} \quad \text{Equation 4.10}$$

From the plot of average K_D vs CAH concentration, depicted in Figure 4.11, it can be observed that the fit of the simple 1:1 model to the data exhibits a concentration dependence of K_D when the CAH concentration is larger than 33 nM. Note that the errors bar indicate the standard deviation obtained from three different trials carried out under similar conditions. This observation contradicts the assumptions in the simple 1:1 model, which predicts a single affinity constant when the system is under equilibrium. For concentrations below 33 nM, the dissociation constant K_D

obtained for both 5:2 and 5:3 SM-CH modified lipid bilayer films were within the error to each other.

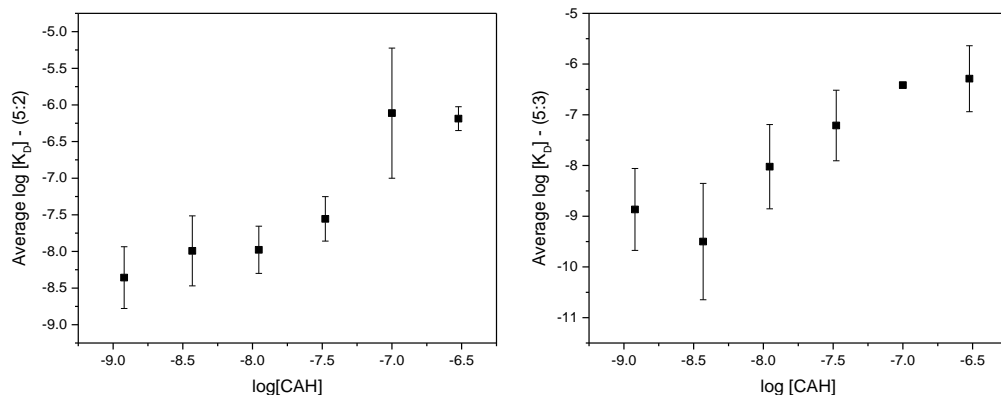


Figure 4.11 Log of affinity constant obtained by Langmuir model is plotted against the log of concentration of the CAH for lipid bilayer films modified with (a) 5:2 and (b) 5:3 SM:CH ratios. Average affinity constant obtained during three trials is given with the error bar indicating the standard deviation between the calculated affinity constants.

When complex, non-optimal binding occurs due to multiple types of interactions taking place on the SM-CH modified bilayer film, the resulting sensorgram will show characteristics that deviate from the classical 1:1 bimolecular interaction. It can be noted from Figure 4.12 that the association phase in higher concentration curves are biphasic, rising steeply at first and then continuing to rise at a slower pace where a 1:1 interaction would be expected to level off at equilibrium in a smooth monophasic binding curve. The biphasic nature of the curves are also reflected in the dissociation step, where a fast initial decay is followed by slower decay later in the profile.

In order to account for this non-ideal behavior, a 1:2 heterogeneous ligand model was used to derive the affinity constants in the system. In this model, the presence of two types of lipid rafts on the surface was assumed.

$$\frac{dC_{AL1}}{dt} = k_a C_A^0 [R_{max} - C_{AL1}] - k_{d1} C_{AL1} \quad \text{Equation 4.11}$$

$$\frac{dC_{AL2}}{dt} = k_a C_A^0 [R_{max2} - C_{AL2}] - k_{d1} C_{AL2} \quad \text{Equation 4.12}$$

$$RU_{association} = C_{AL1} + C_{AL2} = R_{eq1} \left(1 - e^{-\frac{t-t_0}{\tau_{11}}} \right) + R_{eq2} \left(1 - e^{-\frac{t-t_0}{\tau_{12}}} \right) + RI \quad \text{Equation 4.13}$$

$$\text{where, } R_{eq1} = C_A^0 k_{a1} C_{L1}^0 \text{ and } R_{eq2} = C_A^0 k_{a2} C_{L2}^0$$

$$\text{also, } \tau_{11} = \frac{1}{C_A^0 k_{a1} + k_{d1}} \text{ and } \tau_{12} = \frac{1}{C_A^0 k_{a2} + k_{d2}}$$

In the dissociation phase, the response change in the system can be expressed by the following equations.

$$\frac{dC_{AL1}}{dt} = -k_{d1} C_{AL1} \quad \text{Equation 4.14}$$

$$\frac{dC_{AL2}}{dt} = -k_{d2} C_{AL2} \quad \text{Equation 4.15}$$

$$RU_{dissociation} = C_{AL1} + C_{AL2} = R_{eq1} e^{-\frac{t-t_0}{\tau_{21}}} + R_{eq2} e^{-\frac{t-t_0}{\tau_{22}}} + RI \quad \text{Equation 4.16}$$

$$\text{where, } \tau_{21} = \frac{1}{k_{d1}} \text{ and } \tau_{22} = \frac{1}{k_{d2}}$$

Fit of the data to the 1:2 model is shown in Figure 4.12 where the lipid bilayer is modified with 5:2 SM-CH. The fitting parameters are given in Table 4.3. Figure 4.13 (a) (5:2) and 4.12 (b)

(5:3) depict the log of the average dissociation constants obtained for the interaction between CAH and SM:CH modified lipid bilayer films and the error bar in the data illustrates the standard deviation between the K_D values derived from the three data sets collected. It can be noted that the dissociation constants appear more dispersed when plotted against the analyte concentration. Again, at higher CAH concentrations, a slight increment of the dissociation constant was observed for both 5:2 and 5:3 SM:CH modified lipid bilayer films. Though at lower CAH concentrations (33 nM and below), the obtained dissociation constants were independent of the CAH concentration and well within the error of each other. Since the concentration dependence of the dissociation constant was observed for higher concentrations of CAH, it can be understood to be arising from non-specific binding to the sensor surface. This type of behavior for the analyte-ligand interactions are common when the analyte concentrations are far above the K_D , as weaker non-specific interactions tend to come into play.

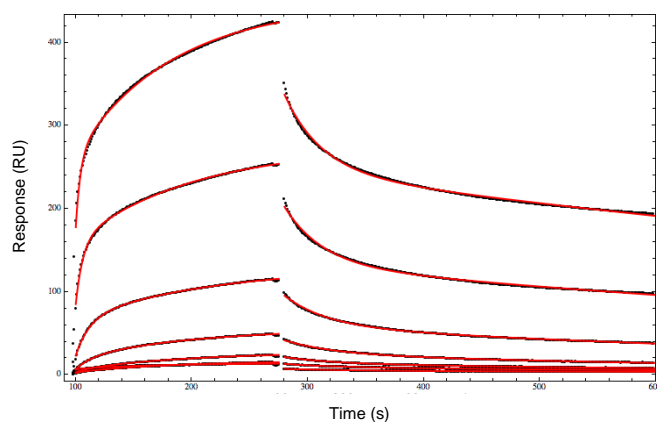


Figure 4.12 Fit of the heterogeneous ligand 1:2 model (red solid line) to the data collected (black solid symbols) during the interaction between CAH and lipid bilayer modified with 5:2 SM:CH ratio. Table 4.2 at the bottom indicates the fitted parameters.

Table 4.3 Fitted parameters of the data on the Figure 4.9 to heterogenous ligand model.

[CAH] / 10 ⁻⁹ M	k _{d1} / 10 ⁻² s ⁻¹	k _{d2} / 10 ⁻² s ⁻¹	k _{a1} / 10 ⁶ M ⁻¹ s ⁻¹	k _{a2} / 10 ⁸ M ⁻¹ s ⁻¹	K _{D1} / 10 ⁻¹⁰ M	K _{D2} / 10 ⁻¹⁰ M	χ ² Association	χ ² Dissociation
1.20	2.10	0.154	7.99	1.49	1.93	1.40	0.10	0.011
3.7	2.42	0.171	2.33	2.14	7.35	11.3	0.083	0.013
11.1	0.179	2.34	4.83	0.00763	48.4	23.5	0.12	0.068
33.3	0.138	2.71	0.22	0.0179	62.6	151	0.93	0.27
100	0.100	3.02	0.0889	0.0131	113	231	1.87	1.53
300	0.0771	3.10	0.0371	0.00689	208	450	1.70	2.89

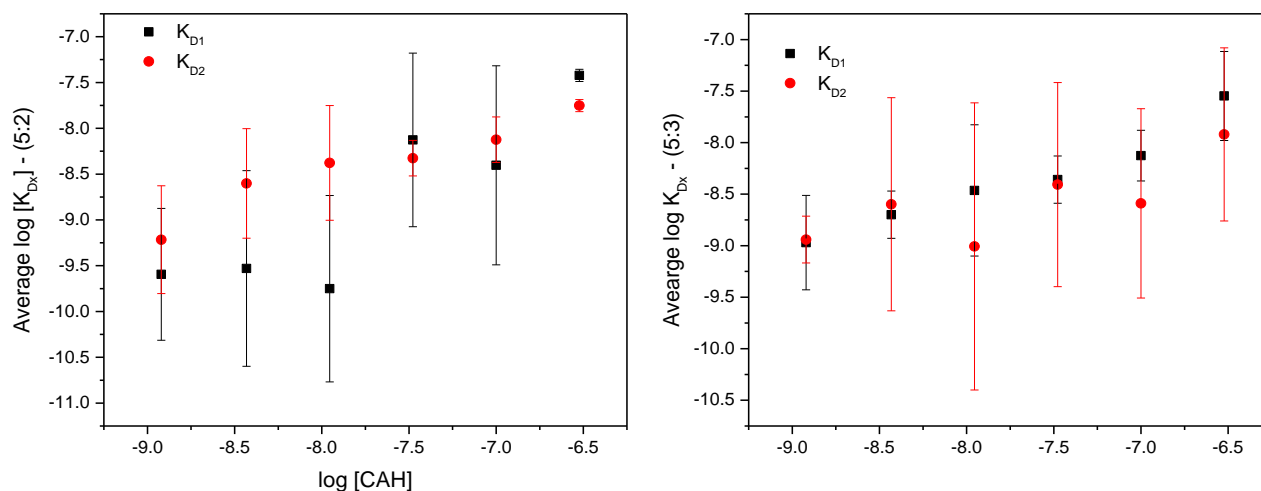


Figure 4.13 Log of affinity constants obtained by heterogeneous ligand model is plotted against the log of concentration of the CAH for lipid bilayer films modified with (a) 5:2 and (b) 5:3 SM:CH ratios. Average affinity constants, K_{D1} (black) and K_{D2} (red), obtained during three trials is given with the error bar indicating the standard deviation between the calculated affinity constants.

4.4 CONCLUSIONS AND FUTURE WORK

In this study successful preparation of a model lipid bilayer film was demonstrated and characterized with different methods. Lipid rafts were prepared by allowing sphingomyelin and cholesterol to be titrated into the model lipid bilayer. Specific binding of HIV capsid protein hexamer to the sphingomyelin and cholesterol modified lipid bilayer film was quantified using SPR. The full length capsid protein exhibited no interaction with the bilayer, indicating that the quaternary structure of the capsid proteins might be playing an important role during its interaction with the lipid rafts. Glycerol kinase was used as a negative control to verify any nonspecific interactions.

A Langmuir (1:1) binding model and heterogeneous ligand (1:2) models were used to quantify the affinity constants for the interaction between CAH and lipid rafts. A concentration dependence of the affinity constants indicates some nonspecific interaction of CAH at higher concentrations. Optimization of the conditions may be needed to obtain a better understanding of the mechanism of interaction. Further investigations are also needed to verify the degree and homogeneity of raft formation on the model lipid membrane.

4.5 REFERENCES

- (1) Campbell, E. M.; Hope, T. J. HIV-1 capsid: the multifaceted key player in HIV-1 infection. *Nat Rev Micro* **2015**, *13*, 471-483.
- (2) Mascarenhas, A. P.; Musier-Forsyth, K. The capsid protein of human immunodeficiency virus: interactions of HIV-1 capsid with host protein factors. *FEBS Journal* **2009**, *276*, 6118-6127.

- (3)Brügger, B.; Glass, B.; Haberkant, P.; Leibrecht, I.; Wieland, F. T.; Kräusslich, H.-G. The HIV lipidome: A raft with an unusual composition. *Proceedings of the National Academy of Sciences of the United States of America* **2006**, *103*, 2641-2646.
- (4)Ono, A.; Freed, E. O. Plasma membrane rafts play a critical role in HIV-1 assembly and release. *Proceedings of the National Academy of Sciences* **2001**, *98*, 13925-13930.
- (5)Lanman, J.; Lam, T. T.; Emmett, M. R.; Marshall, A. G.; Sakalian, M.; Prevelige, P. E. Key interactions in HIV-1 maturation identified by hydrogen-deuterium exchange. *Nat Struct Mol Biol* **2004**, *11*, 676-677.
- (6)Briggs, J. A. G.; Simon, M. N.; Gross, I.; Krausslich, H.-G.; Fuller, S. D.; Vogt, V. M.; Johnson, M. C. The stoichiometry of Gag protein in HIV-1. *Nat Struct Mol Biol* **2004**, *11*, 672-675.
- (7)Benjamin, J.; Ganser-Pornillos, B. K.; Tivol, W. F.; Sundquist, W. I.; Jensen, G. J. Three-dimensional Structure of HIV-1 Virus-like Particles by Electron Cryotomography. *Journal of Molecular Biology* **2005**, *346*, 577-588.
- (8)Barrera, F. N.; del Álamo, M.; Mateu, M. G.; Neira, J. L. Envelope Lipids Regulate the In Vitro Assembly of the HIV-1 Capsid. *Biophysical Journal* **2008**, *94*, L8-L10.
- (9)Pornillos, O.; Ganser-Pornillos, B. K.; Kelly, B. N.; Hua, Y.; Whitby, F. G.; Stout, C. D.; Sundquist, W. I.; Hill, C. P.; Yeager, M. X-Ray Structures of the Hexameric Building Block of the HIV Capsid. *Cell* **2009**, *137*, 1282-1292.
- (10) Du, S.; Betts, L.; Yang, R.; Shi, H.; Concel, J.; Ahn, J.; Aiken, C.; Zhang, P.; Yeh, J. I. Structure of the HIV-1 Full-Length Capsid in a Conformationally-Trapped Unassembled State Induced by Small-Molecule Binding. *Journal of molecular biology* **2011**, *406*, 371-386.
- (11) Pornillos, O.; Ganser-Pornillos, B. K.; Yeager, M. Atomic-level modelling of the HIV capsid. *Nature* **2011**, *469*, 424-427.
- (12) Singer, S. J.; Nicolson, G. L. The Fluid Mosaic Model of the Structure of Cell Membranes. *Science* **1972**, *175*, 720-731.
- (13) Simons, K.; Ehehalt, R. Cholesterol, lipid rafts, and disease. *The Journal of Clinical Investigation* **2002**, *110*, 597-603.
- (14) Pike, L. J. Lipid rafts: bringing order to chaos. *Journal of Lipid Research* **2003**, *44*, 655-667.
- (15) Simons, K.; Toomre, D. Lipid rafts and signal transduction. *Nat Rev Mol Cell Biol* **2000**, *1*, 31-39.
- (16) Fantini, J.; Garmy, N.; Mahfoud, R.; Yahy, N. Lipid rafts: structure, function and role in HIV, Alzheimer's and prion diseases. *Expert Reviews in Molecular Medicine* **2002**, *4*, 1-22.

- (17) London, E.; Brown, D. A. Insolubility of lipids in Triton X-100: Physical origin and relationship to sphingolipid/cholesterol membrane domains (rafts). *Biochimica et Biophysica Acta - Biomembranes* **2000**, *1508*, 182-195.
- (18) Heerklotz, H. Triton promotes domain formation in lipid raft mixtures. *Biophysical Journal* **2002**, *83*, 2693-2701.
- (19) Kraft, M. L.; Weber, P. K.; Longo, M. L.; Hutcheon, I. D.; Boxer, S. G. Phase separation of lipid membranes analyzed with high-resolution secondary ion mass spectrometry. *Science* **2006**, *313*, 1948-1951.
- (20) Lozano, M. M.; Liu, Z.; Sunnick, E.; Janshoff, A.; Kumar, K.; Boxer, S. G. Colocalization of the ganglioside GM1 and cholesterol detected by secondary ion mass spectrometry. *Journal of the American Chemical Society* **2013**, *135*, 5620-5630.
- (21) Sezgin, E.; Levental, I.; Grzybek, M.; Schwarzmann, G.; Mueller, V.; Honigmann, A.; Belov, V. N.; Eggeling, C.; Coskun, Ü.; Simons, K.; Schwille, P. Partitioning, diffusion, and ligand binding of raft lipid analogs in model and cellular plasma membranes. *Biochimica et Biophysica Acta - Biomembranes* **2012**, *1818*, 1777-1784.
- (22) Klymchenko, Andrey S.; Kreder, R. Fluorescent Probes for Lipid Rafts: From Model Membranes to Living Cells. *Chemistry & Biology* **2014**, *21*, 97-113.
- (23) Johnston, L. J. Nanoscale Imaging of Domains in Supported Lipid Membranes. *Langmuir* **2007**, *23*, 5886-5895.
- (24) Choucair, A.; Chakrapani, M.; Chakravarthy, B.; Katsaras, J.; Johnston, L. J. Preferential accumulation of A β (1-42) on gel phase domains of lipid bilayers: An AFM and fluorescence study. *Biochimica et Biophysica Acta (BBA) - Biomembranes* **2007**, *1768*, 146-154.
- (25) Soni, S. P.; LoCascio, D. S.; Liu, Y.; Williams, J. A.; Bittman, R.; Stillwell, W.; Wassall, S. R. Docosaehaenoic Acid Enhances Segregation of Lipids between Raft and Nonraft Domains: 2H-NMR Study. *Biophysical Journal* **2008**, *95*, 203-214.
- (26) Guo, W.; Kurze, V.; Huber, T.; Afdhal, N. H.; Beyer, K.; Hamilton, J. A. A solid-state NMR study of phospholipid-cholesterol interactions: Sphingomyelin-cholesterol binary systems. *Biophysical Journal* **2002**, *83*, 1465-1478.
- (27) Roper, D. K. Determining Surface Plasmon Resonance Response Factors for Deposition onto Three-Dimensional Surfaces. *Chemical engineering science* **2007**, *62*, 1988-1996.
- (28) Arslan Yildiz, A.; Yildiz, U. H.; Liedberg, B.; Sinner, E.-K. Biomimetic membrane platform: Fabrication, characterization and applications. *Colloids and Surfaces B: Biointerfaces* **2013**, *103*, 510-516.

- (29) Zhao, G.; Perilla, J. R.; Yufenyuy, E. L.; Meng, X.; Chen, B.; Ning, J.; Ahn, J.; Gronenborn, A. M.; Schulten, K.; Aiken, C.; Zhang, P. Mature HIV-1 capsid structure by cryo-electron microscopy and all-atom molecular dynamics. *Nature* **2013**, *497*, 643-646.
- (30) Hutter, J. L.; Bechhoefer, J. Calibration of atomic-force microscope tips. *Review of Scientific Instruments* **1993**, *64*, 1868-1873.
- (31) Jung, L. S.; Campbell, C. T.; Chinowsky, T. M.; Mar, M. N.; Yee, S. S. Quantitative Interpretation of the Response of Surface Plasmon Resonance Sensors to Adsorbed Films. *Langmuir* **1998**, *14*, 5636-5648.
- (32) Kienle, D.; de Souza, J.; Watkins, E.; Kuhl, T. Thickness and refractive index of DPPC and DPPE monolayers by multiple-beam interferometry. *Anal Bioanal Chem* **2014**, *406*, 4725-4733.
- (33) Axelrod, D.; Koppel, D. E.; Schlessinger, J.; Elson, E.; Webb, W. W. Mobility measurement by analysis of fluorescence photobleaching recovery kinetics. *Biophysical Journal* **1976**, *16*, 1055-1069.
- (34) Soumpasis, D. M. Theoretical analysis of fluorescence photobleaching recovery experiments. *Biophysical Journal* **1983**, *41*, 95-97.
- (35) Ratto, T. V.; Longo, M. L. Obstructed Diffusion in Phase-Separated Supported Lipid Bilayers: A Combined Atomic Force Microscopy and Fluorescence Recovery after Photobleaching Approach. *Biophysical Journal* **2002**, *83*, 3380-3392.
- (36) Adams, V.; Griffin, L.; Towbin, J.; Gelb, B.; Worley, K.; McCabe, E. R. B. Porin interaction with hexokinase and glycerol kinase: Metabolic microcompartmentation at the outer mitochondrial membrane. *Biochemical Medicine and Metabolic Biology* **1991**, *45*, 271-291.
- (37) Lucero, H. A.; Robbins, P. W. Lipid rafts–protein association and the regulation of protein activity. *Archives of Biochemistry and Biophysics* **2004**, *426*, 208-224.

5.0 ELIMINATING FERMI-LEVEL PINNING IN PbS QUANTUM DOTS USING ALUMINA INTERFACIAL LAYER

This chapter has been published in “Bloom, B. P.*; Mendis, M. N.*; Wierzbinski, E.; Waldeck, D. H. Eliminating Fermi-level pinning in PbS quantum dots using an alumina interfacial layer. *Journal of Materials Chemistry C* 2016, 4, 704-712” (*first co-authors). The thesis author conducted the synthesis, and optical characterization of the PbS quantum dots, all sample preparations, and cyclic voltametric studies of the quantum dots in discuss. The supporting information for this chapter is provided in Appendix B.

Fermi level pinning at quantum dot (QD) – metal interfaces is reported to limit the performance of QD based solar cells. Through a systematic approach we show that the insertion of a thin alumina layer in between a PbS QD and a Au substrate can eliminate Fermi level pinning. In this study band edge energies of different sized PbS QD monolayers with different cross-linkers on Au substrates were measured using ultraviolet photoelectron spectroscopy and electrochemistry. The measured VBM was found to be insensitive to changes in the QD size or cross-linker, when it was immobilized directly on the Au revealing Fermi level pinning of QD valence band to Au Fermi level. After insertion of a thin film of alumina in between the PbS quantum dot monolayer film and the Au substrate, the measured valence band position revealed a shift as a function of ligand and QD size. These results identify a general method to eliminate Fermi level pinning in QDs and an approach to predictably control the energetics at the QD- metal interfaces beneficial for improving the performance of QD based solar cells.

5.1 INTRODUCTION

Third generation solar cells are aimed at overcoming the thermodynamic limit set for the power conversion efficiency calculated by Shockley and Queisser in 1961 for a single junction and to do so at low-cost.^{1,2} Several approaches have been proposed to exceed this limit and one of the most promising schemes is the multi exciton generation by semiconductor quantum dots (QDs). Compared to organic bulk heterojunction solar cells that suffer from lower carrier diffusion lengths and large offsets in the donor and acceptor levels, QD based solar cells have important advantages that mitigate these constraints. The optical band gap in the QDs can be adjusted by changing their size, shape, surface passivation, and composition. Moreover, QDs allow for easy inexpensive solution based synthesis and processing, making them cost effective for large scale fabrication. In addition to these attributes, the organic ligand shell on a QD can be used to fine tune the electronic properties and the solvation characteristics.

In photovoltaic devices, QD films are commonly sandwiched between a cathode and an anode, which may be a metal (Schottky junction cells) or another semiconductor (p-n heterojunction solar cells), to form a complete functional device. Upon illumination by photons with sufficient energy, an electron-hole pair is formed in the QDs and they must be separated and extracted to opposing electrodes to produce a current. In a conventional p-n junction solar cell the charge carriers are driven by an electric field at the interface of the two semiconductors. One common strategy for enhancing charge separation is to alter the band positions within the QD films so that they form a staggered type-II alignment, creating a favorable energy cascade for both electron and hole transport.³⁻⁵ Using arrays of different sized CdSe QDs, Weiss et al. have demonstrated that the photocurrent produced by each sized QD is largely dependent on the relative spatial arrangement and the band offset between them.⁶ Similarly, El-Ballouli et al. have shown

that favorable charge transfer from PbS QDs to PCBM⁷ and cationic porphyrins⁸ is determined by the size of the nanoparticle. In a previous study by Wang et al, donor- acceptor assemblies of CdSe-CdTe QD layers were shown to facilitate unidirectional charge transfer as long as proper energy band alignment is maintained in the photovoltaic device.⁵ In a recent implementation of this strategy Chuang et al., used ligand induced band energy shifts to create a QD energy gradient that led to a photovoltaic efficiency over 8%.³ Furthermore, an efficiency as high as 10.7% has been achieved by tuning the energy alignment at the rectifying interface, a new record for QD based solar cells.⁹

Surface ligands have been shown to shift the absolute energy positions of the valence band maximum (VBM) and conduction minimum (CBM) of QDs, and a growing body of evidence suggests that the magnitude of the energy shift can be characterized as a function of the dipole moment between the surface and linking group and the intrinsic dipole moment of the ligand itself.¹⁰⁻¹² By changing the capping ligand one can shift band energies of CdSe^{10,13-15}, CdS¹⁶, PbS^{4,11,17,18}, as well as other nanocrystals¹⁹. Most recently, researchers have been using ligands to shift the absolute energy levels of QDs and to form an energy level gradient for efficient charge separation. However, the magnitudes of the ligand's influence on the band energies can be affected by the electronic and chemical properties of a QD photovoltaic device at interfaces. When QDs are adsorbed onto a metal, charge equilibrium between the metal and the QD occurs; and it can 'pin' the electronic states of the QD to the Fermi level of the metal substrate. Often times the electronic energies of QDs determined in solution or under flat band conditions are used in determining a photovoltaic device architecture. When Fermi level pinning occurs in QD based solar cell devices, the QD size and ligand induced effects over the energy position may no longer persist. In a study on CdSe QDs immobilized onto Au substrates by a decanedithiol linker, Markus et al. have shown

that the absolute energy position of the VBM of the QDs larger than 2.8 nm does not change.²⁰ Depending upon the relationship of the QDs electronic states to that of the substrate, the CBM can also be pinned.²¹ Previous electrochemical and UPS measurements on CdTe QD monolayers attached to an Au substrate through dithiol linkers showed no shift in VBM over the size range of 3.7 to 6.0 nm.²² In Schottky junction solar cells, Fermi level pinning reduces the interfacial barrier height for charge injection and can reduce overall device efficiency. In some cases the pinning between the QDs and a can persist for significant distances, e.g. 25 nm thick MO_3 layers.²³ Because the photoinduced free carriers must transfer through interfaces to be collected, control over the electronic properties of the QD-metal junction are important for improving the photoconversion efficiency of QD based solar cells.

5.1.1 Ligand effects on PbS QD Energetics

In photovoltaic devices, QDs are usually coated with short ligands to achieve better electronic coupling by changing the inter-QD tunneling distance and the effective dielectric constant. In a study by Liu et al, the dependence of ligand length and QD size on carrier mobility were reported for PbSe QDs field effect transistors.²⁴ The degree of QD surface passivation is also important for minimizing trap induced charge recombination. Wanger et al. showed that the effective density of trapped carriers has a strong dependence on ligand treatment in PbS QD films.²⁵ Zhitomirsky et al. measured the effect that QD films treated with organic (mercaptoproponic acid) or a mixture of hybrid organic-inorganic (tetrabutylammonium iodide) ligand types have on charge mobility, trap density, and exciton diffusion length in QD films.²⁶ They have found that films with such organic-inorganic passivation exhibit the largest charge diffusion lengths. These findings have led to the use of organic-inorganic hybrid passivation of

PbS QDs to make a photovoltaic device with 7% power conversion efficiency.²⁷ Control of energetics at the rectifying interface of the PbS QD solar cells has allowed further improvement in photoconversion efficiency up to 10.7 %.

Axnanda et al. used photoelectron spectroscopy to measure the work function of 30 nm thick PbS QD films as a function of the capping ligand and observed a ligand effect on the energetics.¹⁷ This work showed that methoxide, mercaptopropionic acid, and ethanedithiol (EDT) ligands could shift the VBM over a range of 0.3 eV. The resulting deeper work function VBM energy position has been explained by incomplete surface passivation and the presence of hole trap states. In a more comprehensive study, Brown et al. examined the band energies of PbS QD films (~100 nm) modified with 12 different ligands and reported that the VBM shifts over a range of 0.9 eV with ligand.¹¹ The same group has used the VBM energy offset between tetrabutylammonium iodide (TBAI) and 1, 2-ethanedithiol (EDT) capping ligands to alter the band energy positions and produce favorable charge transport in a photovoltaic device, achieving a power conversion efficiency of 8.5 %.³ In another study by Crisp et al. it was shown that inorganic metal halide ligands in thick films of PbS (~ 300 -750 nm) leads to high efficiency photovoltaic devices.¹⁸ They have used four different metal halides and attributed the improved device efficiency to better carrier transport in the film with halide passivation. Their XPS studies performed on the films of PbS treated with iodide ligands suggest a deeper work function, as compared to sulfur containing ligands. Santra et al. used three different para-substituted thiophenols with different dipole moments as capping ligands for PbS QD films (350 nm) to fabricate type-II heterojunction solar cells and reported a systematic shift in the VBM in PbS QDs.⁴ Again type-II VBM alignment was shown to facilitate favorable unidirectional charge transport,

however, when the bands edges are aligned in a way that the electron and hole encounter a potential barrier to reach the respective electrodes, a lower efficiency results.

Taken together, all the above studies affirm the role of capping ligand in manipulating the electronic band energies of PbS QDs and subsequently, the band alignment in solar cells. Control over the carrier mobility, trap state density, and charge diffusion has been achieved by tuning the cross-linker. Major advances in photoconversion efficiency have been obtained using this strategy in QD solar cell devices. Moreover, photovoltaic devices of PbS QD-polymer blends (poly((4,8-bis(octyloxy)benzo(1,2-b:4,5-b')-dithiophene-2,6-diyl)(2((dodecyloxy)carbonyl)thieno(3,4-b)-thiophenediyl))) have reported a dependence of the open circuit voltage and overall device performance on the PbS QD ligand treatment which has been credited to the ligands influence over the carrier lifetime.²⁸ Despite these advances, the overall power conversion efficiencies of the QD based solar cells still remain below their expected performance largely because of low open circuit voltage.²⁹⁻³² Generally this limitation has been understood to originate from the presence of sub-bandgap states or midgap states that are formed by a large number of surface states associated with the defects on the QD surface. Such midgap states drive Fermi level pinning at the QD/metal interface in Schottky junction solar cells; as a result, the open circuit voltage is controlled by the pinning rather than the metal's work function or the QD's band edge.³¹ This work is substantiated by the work of Yoon et al. who showed that insertion of an LiF layer between the top Al contact and PbS QDs improved the open circuit voltage in PbS QD solar cells.³³ Furthermore, oxidized interfacial layers on PbS QDs,³⁴ as well as insertion of a CdS shell on PbS QDs,³⁵ have been shown to increase the open circuit voltage in Schottky junction solar cell. A general approach to passivate these gap states and eliminate Fermi pinning at the QD – metal interfaces is not available.

PbS quantum dots (QDs) are promising candidates for third generation photovoltaics because the elements are earth abundant³⁶, the bandgap is tunable over a wavelength range that can best exploit the solar spectrum³⁷, and they offer the potential for multiple exciton generation^{38,39}. This work examines the band edge energetics in PbS QD films and demonstrates the conditions for Fermi level pinning versus ligand control over the energetics. More specifically, this work shows that a thin alumina film (circa 1 to 3 nm) can be used to eliminate Fermi level pinning effects. The energy band positions of PbS QD monolayers on Au substrates, with and without an alumina layer, were measured using electrochemistry and ultraviolet photoelectron spectroscopy. When a monolayer of PbS QDs was deposited on top of an Au substrate, valence band positions were independent of known trends with QD size and surface ligand type, indicating strong Fermi level pinning. Introduction of a thin alumina interfacial layer between the Au and PbS inhibits Fermi level pinning so that the QD size and ligand can be used to manipulate the band edge positions. These findings highlight the importance of interfacial states in photovoltaic devices and enable precise control over QD properties for charge injection.

5.2 EXPERIMENTAL

5.2.1 Substrate Preparation

Substrates (12.5 mm × 25.0 mm) for these experiments were prepared by e-beam evaporation (AJA Deposition System) of 100 nm thick films of Au on glass substrates supported by a 5.0 nm Ti adhesion layer. For bare Au experiments the samples were plasma cleaned and used immediately. For experiments with an alumina layer, half of the substrate was covered with a wafer

tape and poly-methyl-methacrylate (950k A11 PMMA, Micro Chem) was spun on it at a speed of 1500 rpm for 1 min using a spin processor (Laurell WS-400-6NPP-LITE). The wafer tape was removed, and the substrates were baked on a hot plate at 180 °C for 5 min. Thin films of Al₂O₃ were then deposited using atomic layer deposition (Cambridge Nanotech Fiji). The samples were then kept overnight in acetone to remove the PMMA and to expose the underlying Au substrate on half of the electrode.

5.2.2 PbS QD synthesis and characterization

The synthesis of PbS QDs followed a general procedure described elsewhere.⁴⁰ All of the materials, such as; PbCl₂ (Stern Chemicals), oleylamine (OLA, Sigma Aldrich), oleic acid (OA, Sigma Aldrich), and bis(trimethylsilyl) sulfide (TMS, Sigma Aldrich) were purchased in the highest purity grade available and used without further purification. In a typical synthesis, 3.0 mmol PbCl₂ (0.834 g) was mixed with 10 ml of OLA and degassed at 80.0 C, followed by heating to 140.0 C under argon. The suspension was maintained at this temperature for 30 min and then cooled to 30.0 C. Then 210.0 μl of TMS mixed in 2.0 ml of OLA was injected into the reaction mixture. The mixture was then rapidly elevated to a high temperature while stirring and subsequently quenched in a water bath once the desired QD size was obtained. The PbS QDs were precipitated from solution through the addition of acetone and centrifugation. The purified QDs were then dissolved in octane with 500 μl of OA, for ligand exchange, for 12 hours. The subsequent solution was then filtered using a 0.2 μm syringe filter, purified again, and then dissolved in 4.0 ml of octane.

Absorption spectra of the PbS QDs were recorded in octane using a spectrometer (Model 8453 Agilent Spectrometer). PbS QD emission spectra were obtained after exciting at 500 nm wavelength using a spectrofluorometer (Nanolog, Hobira).

5.2.3 PbS Thin Film Preparation and Ligand Exchange

All of the QD films were prepared by spin-casting. For each QD size, the PbS QD concentration was determined by evaluating the absorption spectrum. 10 μ l of the PbS QD solution was spun onto Au substrates at a speed of 2500 rpm for 15 s. The resulting QD film was then cross-linked (*vide infra*) and thickness was determined using AFM (Agilent Technologies) under tapping mode. This thickness was then used to determine a dilution factor of the QD solution to obtain a submonolayer thickness. The sample was prepared again and AFM was used to confirm submonolayer formation.

Ligands used for solid state ligand exchange, 1,4-benzenedithiol (BDT, Alpha Aesar), 1,2-ethanedithiol (EDT, Sigma Aldrich), and ethylenediamine (EDA, Sigma Aldrich) were used as purchased. All ligands were dissolved in acetonitrile at varying concentrations; 1.7 mM BDT and one volume percent for both EDT and EDA. In a typical ligand exchange procedure, ~ 0.3 ml of ligand solution was dispersed onto the PbS monolayer film and allowed to sit for 1 min. The film was flushed with acetonitrile and spun dry two times to remove any unbound ligand. The samples were immediately transferred to a glove bag and stored under argon until electrochemical or UPS analysis.

5.2.4 Atomic Force Microscopy Characterization

AFM measurements were performed with an Agilent 5500 atomic force microscopy system using silicon cantilevers with resonance frequency of 96-175 kHz and spring constant of 5-37 N/m (PPP-SEIHR, Nanosensors). Precise values of the spring constants were determined using a thermal oscillation technique.⁴¹ The film thickness was determined from the difference in the average height of the substrate covered with the PbS nanoparticle film and the bare gold substrate. The gold surface was exposed by scraping off the film in a 500 nm by 500 nm square area by performing a single AFM scan in a contact mode with an applied load force of ca. 500 nN. Following this procedure, a larger 4 micrometer by 4 micrometer square area was imaged in acoustic AFM mode to capture the original nanoparticle film together with the exposed gold substrate area. Switching between AFM operating modes was performed with a fully contracted z-axis piezoelement (the tip and the substrate were out of contact).

5.2.5 Electrochemical Characterization

Cyclic voltammetry on PbS films was performed in deoxygenated acetonitrile (99.9%, Sigma Aldrich) in a three electrode configuration on a CH Instruments 618B potentiostat. A Pt wire was used for the counter electrode, and Ag/AgNO₃ was used as the reference electrode. A 0.1 M solution of tetrabutylammonium hexafluorophosphate (Sigma Aldrich) was used as the supporting electrolyte. Voltammograms were obtained by scanning from 0 V to -1.2 V at a scan rate of 200 mV/s. The onset of the reduction peak for the QD was determined after subtraction of the background charging current, through an exponential fit. The formal potential of ferrocene / ferrocenium was used to calibrate the Ag/AgNO₃ reference electrode and convert the CBM of the

PbS QDs to the vacuum energy scale.²² The VBM was determined through addition of the optical band gap and exciton binding energy to the CBM.

5.3 PHOTOEMISSION SPECTROSCOPY CHARACTERIZATION

UPS measurements were performed using an ESCALAB 250XI XPS at a base pressure of $\sim 10^{-10}$ millibar. Electrical contact to the stage was made using copper tape on the edge of the Au substrate. Experiments were performed to ensure that no Cu photoemission signal contributed to the spectra. A bias of -5.0 eV was applied to the stage so that 1) the secondary electron cut off of the sample is distinguishable from that of the detector and 2) to ensure that the local vacuum level of the sample is more negative than that of the detector. A pass energy of 1.0 eV and a dwell time of >50 s were used to increase resolution and eliminate charging. A He (I) discharge lamp, 21.22 eV, was used as the ultraviolet source. The onset region and subsequent determination of the valence states were fit using previously published protocols.²⁰ In all experiments the Fermi edge of the underlying Au substrate is monitored to accurately reference the data.

5.4 RESULTS

Absorbance and emission spectra of the three different sized PbS quantum dots (QDs) used in this study are shown in Figure 5.1 (a). The sizes of these QDs were estimated from the empirical model developed by Moreels et al.⁴² Note that the Stokes shift observed for the PbS QDs changes with size in a manner consistent with previous literature.^{43,44} The PbS QDs were then spin-coated

onto an Au substrate and AFM measurements were performed. Figure 1 (b) and (c) show an example AFM image and measured thickness used to characterize each QD film for the determination of average thickness.

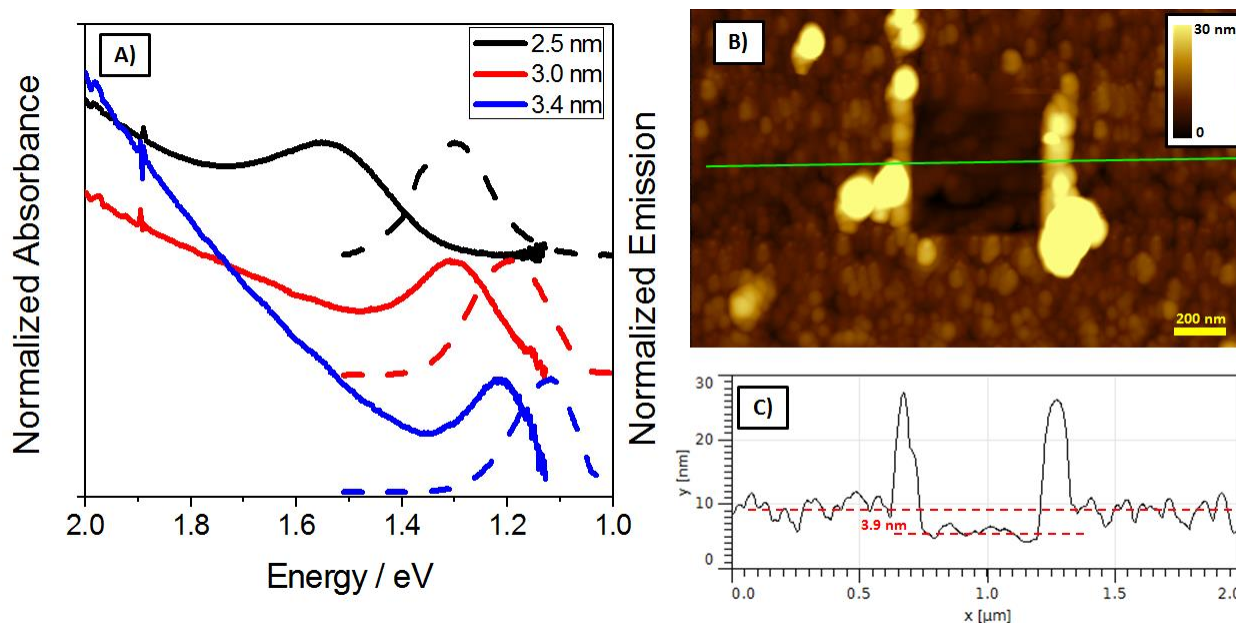


Figure 5.1 a) Normalized absorbance (solid line) and emission (dashed line) spectra of 2.5, 3.0, and 3.4 nm QDs in octane; b) AFM image of 3.0 nm PbS QDs that are cross-linked with EDT on Au; and c) height profile of the scratched QD film.

Figure 5.2 shows representative data from UPS (a) and electrochemistry (b) for 3.0 nm PbS with an EDA cross-linker. For UPS measurements, the VBM is determined by measuring the onset of the photoelectron spectra relative to the Fermi edge of Au (E_f). The work function of a bare Au substrate (4.8 eV) was then used to reference these data to absolute electrode potential found in the electrochemical measurements. Cyclic voltammetry measurements on the CBM of PbS were

performed in a manner similar to that reported previously.²² Briefly, the PbS QDs exhibited a cathodic peak in the potential range of -0.9 to -0.5 volts versus Ag/AgNO₃, similar to those reported by Hyun et al.⁴⁵ Because the range overlaps with the limit of the solvent's potential window it was necessary to perform background subtraction. The voltammogram, excluding the peak region, was fit to an exponential (green) and then subtracted from the data to give a background subtracted (blue) curve, Figure 5.2 (b). This procedure minimizes the effect of the capacitive current and allows for more accurate determination of the onset potential. Using the known absolute electrode potential for ferrocene, the onset potential can then be related to the vacuum energy scale by referencing to the ferrocene / ferrocenium redox couple.

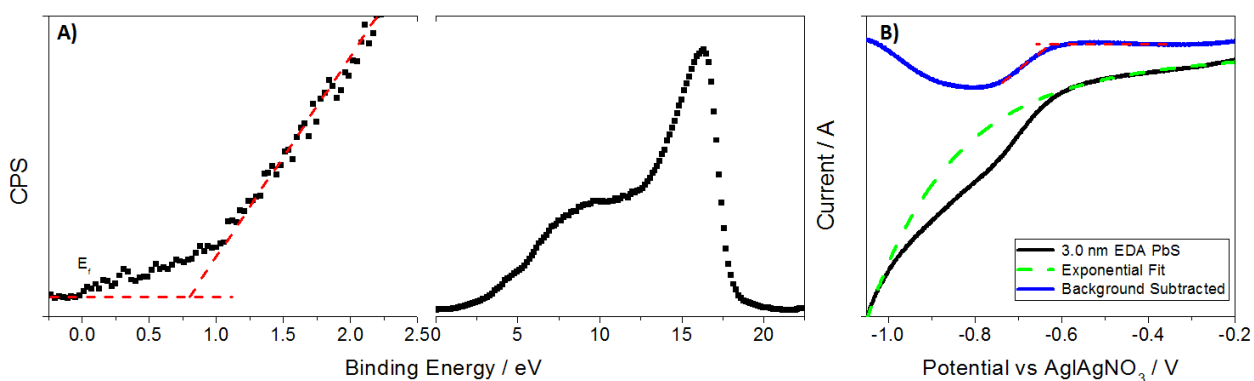


Figure 5.2 UPS spectra (a) and cyclic voltammogram (b) of 3.0 nm PbS QDs that are cross-linked by EDA to determine the VBM and CBM respectively. UPS of the onset region (a, left) and the full spectra (a, right) are shown. The red dashed line in both the UPS spectra and voltammogram show the onset potential associated with the corresponding electronic states.

Figure 5.3 summarizes the VBM and the CBM positions that were determined for thin films of the three different sized QDs that are capped with three different ligands: EDT, BDT, and EDA. The VBM was experimentally determined by UPS (Figure 3B, stars) and the CBM was

experimentally determined using cyclic voltammetry (Figure 5.3 (a), stars). The optical bandgap and exciton binding energy were then used to determine the other bandedge. The measurements were performed on the same sample which was divided into two separate pieces using a glass cutter following the thin film fabrication. Each symbol represents the average of three independent measurements (an example of each is included in the supporting information). The standard deviation of the measurement is used for the error bars in the electrochemistry measurements and the resolution of the instrument, 0.1 eV, is used for the error bars in the UPS measurements. Slight differences in the electronic state positions obtained through the UPS and voltammetry methods exist and are attributed to environmental differences during measurement. Note that each of the experimental methods has limitations that affect the accuracy. The voltammetry is performed in an electrolyte solution where dielectric and double layer, as well as solvation, effects can influence the measured reduction potential. The UPS measurements are performed in vacuum and can be affected by local vacuum level shifts.⁴⁶ Despite the differences in energy found for the VBM from the two different techniques the experimental data are in reasonable agreement. Moreover, the two methods independently demonstrate that the VBM of the PbS QD monolayer films does not change significantly over the size range and cross-linker types studied. In both experiments the CBM shifts systematically to higher energies with a decrease in QD size. For UPS measurements on medium and large sized QDs the CBM is reported below the bulk band energy of PbS (4.35 eV),¹⁵ providing further evidence that Fermi-level realignment occurs at the metal-NP interface.

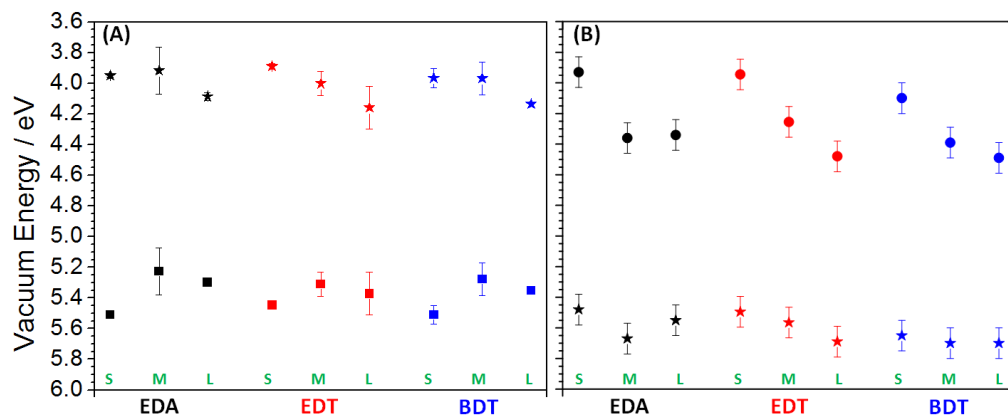


Figure 5.3 Electronic states of PbS monolayers determined by cyclic voltammetry (a) and photoelectron spectroscopy (b) are plotted versus the three different ligands used for cross-linking: EDA (black), EDT (red), and BDT (blue). Stars are representative of the experimentally determined values and a combination of the optical band gap and exciton binding energy was used to calculate the other bandedge. The S, M, and L represent the three different QD diameters 2.5 nm, 3.0 nm, and 3.4 nm, respectively. The dashed black line corresponds to the bulk CBM of PbS and the gray bar illustrates that all of the experimental UPS data fall within the error associated with the UPS measurement 5.6 +/- 0.1 eV. The error bars in the UPS measurement are a result of instrument resolution and the error bars in the electrochemistry data are representative of the standard deviation of multiple measurements.

When a thin interfacial layer of alumina is placed between the PbS monolayer film and the Au substrate, a trend different from that shown in Figure 3 was observed. The Au substrate used for these studies contained Al_2O_3 on one half of the substrate while the other half was bare Au (see Figure 5.4(a)). This procedure enabled a direct comparison of the two systems under identical conditions. UPS was employed to deduce the VBM for EDT cross-linked monolayer films of 2.5 nm and 3.0 nm diameter PbS QDs with 1 and 3 nm alumina layers (supporting information Figure S4). Figure 5.4(a) shows the bandedge values obtained, as relative shifts from the Fermi level of Au (E_f), from these measurements. The plot shows that when no alumina is present (0 nm), no relative shift in VBM from the Fermi level of Au is found as a function of QD size. When alumina

is present, however, the two different sized QDs have distinctly different electronic energy positions. Furthermore this shift depends on the thickness of the interfacial alumina, indicating that the PbS VBM is being decoupled from the Au Fermi level and the expected size dependent VBM shift is becoming manifest. Namely, the larger nanoparticles (in the 1 and 3 nm alumina thickness) have the VBM slightly higher, closer to that of bulk PbS. Note that a different cleaning procedure (see experimental section) was used here than in the previous measurements (Figure 5.3) in order to maintain the integrity of the film. As a result the work function of Au can shift slightly, however, both are internally consistent.

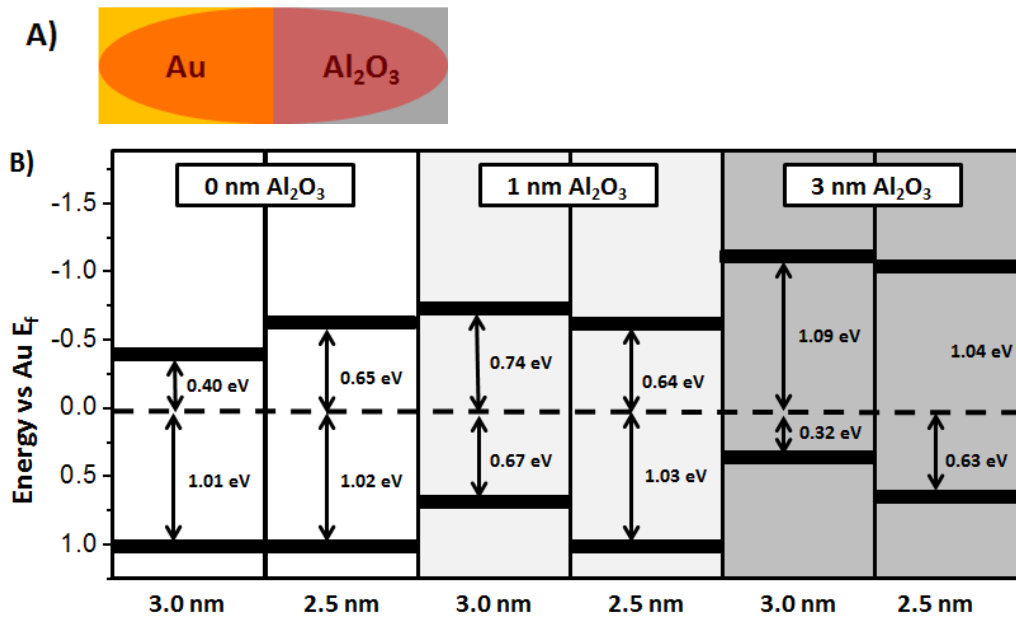


Figure 5.4 Diagram (a) shows a schematic of the substrate configuration used in this part of the study and diagram (b) shows the UPS determined energy band positions of the PbS monolayers. In (b) the VBM and CBM are presented as relative shifts from the Au Fermi level ($E_f = 0$ eV) for two different size QDs and three different thicknesses of alumina. The black boxes correspond to the band edge positions and their shift from E_f is provided next to the double headed arrow.

Figure 5.5 shows the VBM and CBM of PbS QD monolayers on 100 nm Au substrates and their energies obtained by UPS for 2.5 nm QDs (open symbol) and 3.0 nm QDs (closed symbol) without (a) and with (b) a 3 nm alumina interfacial layer. The NPs are cross-linked in the same manner that was used in the Fermi level pinning study: BDT, EDT, and EDA. The energy of the VBM (black symbols) and CBM (red symbols) are reported with respect to the Au Fermi edge in the UPS spectra (supporting information Figure S5). On the Au substrate without alumina, it is clear that there is no variation in the VBM with QD diameter and cross-linker type. When alumina is present the VBM changes in a manner consistent with earlier reports: 1) the shift in VBM is correlated with the ligand identity for QDs of the same size and 2) the VBM shifts more strongly for QDs with a larger surface-to-volume ratio.

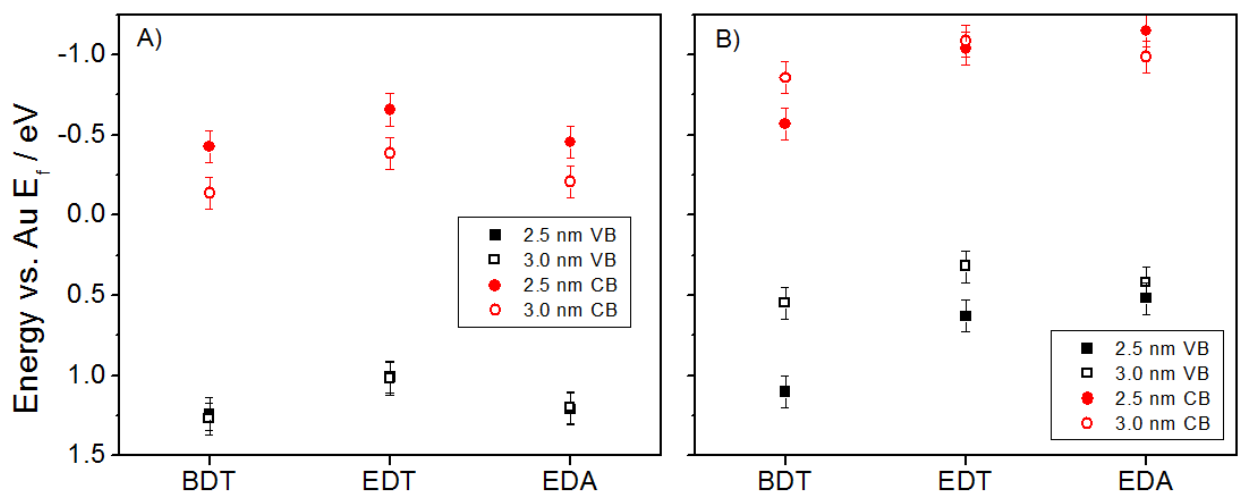


Figure 5.5 VBM (black symbols) and CBM (red symbols) of PbS monolayers with 2.5 nm (open symbols) and 3 nm (closed symbols) size QDs, as determined by UPS. Diagram (a) is on the bare Au part of the substrate and diagram (b) is for the part of the substrate covered with 3.0 nm of alumina. Three different cross-linkers were studied: BDT, EDT and EDA. Energy level positions are reported with respect to the Au Fermi edge in the UPS spectra.

5.5 DISCUSSION

When a semiconductor QD is in physical and electrical contact with a metal, charge equilibration occurs and the semiconductor's electronic states couple to those of the metal. If these interactions are caused by localized interfacial states,⁴⁷ then the charge exchange creates an electric field that 'pins' the semiconductor bandedge to the metal Fermi level. Which bandedge is pinned depends on the details of the orbitals that contribute to the electronic coupling and the surface state energy, with respect to the bandedge. Fermi level pinning results in different sizes of QDs exhibiting similar barrier heights for charge injection upon photoexcitation. This phenomenon has been demonstrated for quantum dots at the interface with either a metal, or metal oxide, through electrochemical,^{20,22} photoemission,^{20-22,48-50} and Kelvin probe techniques.⁵¹ The data in Figure 2 show that this pinning behavior is observed for monolayers of three differently sized PbS QDs on Au. Interestingly, the pinning effect persists for different cross-linkers (EDT, EDA, and BDT) despite recent studies which indicate that a change in the surface passivation changes bandedge positions of the QDs.

It is important to appreciate the difference between the monolayer films studied herein and the thicker films reported on by a number of other workers.^{4,11,17} As the film thickness increases, the outer layers which are no longer directly coupled to the substrate, should have their energetics affected by the coupling between QDs, rather than by the asymmetric QD to metal coupling. In this limit, strong ligand dipolar effects are expected to determine the VBM and CBM of the PbS NPs. Thus one expects that the profile of bandedge energy with thickness will change through a thick film, from the Fermi level pinning value at the metal electrode surface to the QD-QD coupling value for thick films.

This study shows how the Fermi level pinning, caused by electronic coupling between the QDs surface states and the underlying metal electrode, can be eliminated by inserting a thin Al₂O₃ layer. The presence of this layer acts to reduce the metal-QD coupling and charge exchange. As Figure 3 illustrates, an increase in the thickness of Al₂O₃ from 0 nm to 3 nm between Au and an EDT cross-linked PbS monolayer causes a shift in the VBM energy from a size independent pinned value to a size dependent value. These data provide direct evidence that strong coupling and charge displacement between the NPs and the Au electrode cause the Fermi level pinning, and ligand control is returned when this coupling is weakened enough. A different type of oxide film could be used to modulate the magnitude of the effect observed here; for example Beard et al. have examined how the open circuit voltage of a PbS QD film changes with thickness of a MoO₃ layer (up to 25 nm) between it and a metal electrode.²³ As such, it is expected that the barrier height for charge injection would be weakly dependent or even independent of cross-linker type or NP size when the thickness of MoO₃ is less than this amount. The large thicknesses needed to reduce the pinning effect in their study likely arises because the electronic states of the MoO₃ are energetically close to the electronic states of PbS; ie. enhancing their mixing.

The system under investigation in Figure 5.4 is in agreement with the explanation given by Choi et al. in which a PbS film was annealed in air to passivate the NPs with a thin oxide layer prior to deposition of the top contact (LiF/Al/Ag).³⁴ The PbO passivates the surface state defects on the QDs that are assumed to participate in charge equilibration and therefore inhibits Fermi level pinning. In this situation, the Schottky barrier height for hole injection is expected to increase and the surface recombination is minimized, thus leading to an improvement in device photoconversion efficiency. Using a core-shell QD consisting of a CdS shell and PbS core has also been shown as a way to increase open circuit voltage compared to core only devices of the same

size, presumably for the same reason.³⁵ Deposition of a thin alumina film accomplishes the same goal as oxidation of the PbS and passivation with a CdS shell; namely, it inhibits charge equilibration at the interface, but unlike the other methods it also preserves the QD's chemical composition.

Shifts in the electronic state energies of the PbS QDs as a function of cross linker are also expected to return in the presence of an alumina tunneling barrier. Figure 5 shows how the VBM of 2.5 and 3.0 nm PbS QDs transition from ligand independent behavior on Au (a) to ligand dependent characteristic shifts, similar to those reported by Brown et al.¹¹, when alumina is present (b). Previous studies on CdSe have shown that small QDs exhibit larger ligand effects than large QDs because of their larger surface-to-volume ratio.¹⁰ Figure 5.5(b) shows that BDT, EDT, and EDA cross-linkers shift the VBM much more for 2.5 nm PbS QDs than for 3.0 nm PbS QDs, in agreement with this claim. These ligand dependent shifts in electronic energies further corroborate the conclusion that the thin alumina layer acts to decouple the electronic states of QDs from Au. Operating under these conditions it should now be possible to tune the PbS QD properties at the interface and overcome charge injection and separation issues that have plagued previous architectures.

5.6 CONCLUSION

This work demonstrates that Fermi level pinning persists in monolayer PbS QD films on Au substrates with different cross-linkers. Introduction of a thin alumina layer between the PbS QDs and the Au substrate was shown to weaken Fermi level pinning enough that size- and ligand-dependent properties are manifest. These findings point to a procedure for using ligand tuning of

QD energetics to enhance charge injection and separation to overcome the open circuit voltage deficit reported for PbS.

5.7 REFERENCES

- (1) Brown, G. F.; Wu, J. Third generation photovoltaics. *Laser & Photonics Reviews* **2009**, *3*, 394-405.
- (2) Nozik, A. J.; Beard, M. C.; Luther, J. M.; Law, M.; Ellingson, R. J.; Johnson, J. C. Semiconductor Quantum Dots and Quantum Dot Arrays and Applications of Multiple Exciton Generation to Third-Generation Photovoltaic Solar Cells. *Chemical Reviews* **2010**, *110*, 6873-6890.
- (3) Chuang, C.-H. M.; Brown, P. R.; Bulović, V.; Bawendi, M. G. Improved performance and stability in quantum dot solar cells through band alignment engineering. *Nat Mater* **2014**, *13*, 796-801.
- (4) Santra, P. K.; Palmstrom, A. F.; Tanskanen, J. T.; Yang, N.; Bent, S. F. Improving Performance in Colloidal Quantum Dot Solar Cells by Tuning Band Alignment through Surface Dipole Moments. *The Journal of Physical Chemistry C* **2015**, *119*, 2996-3005.
- (5) Wang, Y.; Wang, L.; Waldeck, D. H. Electrochemically Guided Photovoltaic Devices: A Photocurrent Study of the Charge Transfer Directionality between CdTe and CdSe Nanoparticles. *The Journal of Physical Chemistry C* **2011**, *115*, 18136-18141.
- (6) Weiss, E. A.; Porter, V. J.; Chiechi, R. C.; Geyer, S. M.; Bell, D. C.; Bawendi, M. G.; Whitesides, G. M. The Use of Size-Selective Excitation To Study Photocurrent through Junctions Containing Single-Size and Multi-Size Arrays of Colloidal CdSe Quantum Dots. *Journal of the American Chemical Society* **2008**, *130*, 83-92.
- (7) Kim, G.-H.; García de Arquer, F. P.; Yoon, Y. J.; Lan, X.; Liu, M.; Voznyy, O.; Yang, Z.; Fan, F.; Ip, A. H.; Kanjanaboos, P.; Hoogland, S.; Kim, J. Y.; Sargent, E. H. High-Efficiency Colloidal Quantum Dot Photovoltaics via Robust Self-Assembled Monolayers. *Nano Letters* **2015**.
- (8) Bloom, B. P.; Zhao, L.-B.; Wang, Y.; Waldeck, D. H.; Liu, R.; Zhang, P.; Beratan, D. N. Ligand-Induced Changes in the Characteristic Size-Dependent Electronic Energies of CdSe Nanocrystals. *The Journal of Physical Chemistry C* **2013**, *117*, 22401-22411.
- (9) Brown, P. R.; Kim, D.; Lunt, R. R.; Zhao, N.; Bawendi, M. G.; Grossman, J. C.; Bulović, V. Energy Level Modification in Lead Sulfide Quantum Dot Thin Films through Ligand Exchange. *ACS Nano* **2014**, *8*, 5863-5872.

- (10) Yang, S.; Prendergast, D.; Neaton, J. B. Tuning Semiconductor Band Edge Energies for Solar Photocatalysis via Surface Ligand Passivation. *Nano Letters* **2012**, *12*, 383-388.
- (11) Wang, C.; Shim, M.; Guyot-Sionnest, P. Electrochromic Nanocrystal Quantum Dots. *Science* **2001**, *291*, 2390-2392.
- (12) Wu, P.-J.; Tsuei, K.-D.; Hsieh, M.-T.; Wei, K.-H.; Liang, K. S. Dependence of the final-state effect on the coupling between a CdSe nanoparticle and its neighbors studied with photoemission spectroscopy. *Physical Review B* **2007**, *75*, 115402.
- (13) Jasieniak, J.; Califano, M.; Watkins, S. E. Size-Dependent Valence and Conduction Band-Edge Energies of Semiconductor Nanocrystals. *ACS Nano* **2011**, *5*, 5888-5902.
- (14) Shalom, M.; Rühle, S.; Hod, I.; Yahav, S.; Zaban, A. Energy Level Alignment in CdS Quantum Dot Sensitized Solar Cells Using Molecular Dipoles. *Journal of the American Chemical Society* **2009**, *131*, 9876-9877.
- (15) Axnanda, S.; Scheele, M.; Crumlin, E.; Mao, B.; Chang, R.; Rani, S.; Faiz, M.; Wang, S.; Alivisatos, A. P.; Liu, Z. Direct Work Function Measurement by Gas Phase Photoelectron Spectroscopy and Its Application on PbS Nanoparticles. *Nano Letters* **2013**, *13*, 6176-6182.
- (16) Crisp, R. W.; Kroupa, D. M.; Marshall, A. R.; Miller, E. M.; Zhang, J.; Beard, M. C.; Luther, J. M. Metal Halide Solid-State Surface Treatment for High Efficiency PbS and PbSe QD Solar Cells. *Scientific Reports* **2015**, *5*, 9945.
- (17) Soreni-Harari, M.; Yaacobi-Gross, N.; Steiner, D.; Aharoni, A.; Banin, U.; Millo, O.; Tessler, N. Tuning Energetic Levels in Nanocrystal Quantum Dots through Surface Manipulations. *Nano Letters* **2008**, *8*, 678-684.
- (18) Markus, T. Z.; Wu, M.; Wang, L.; Waldeck, D. H.; Oron, D.; Naaman, R. Electronic Structure of CdSe Nanoparticles Adsorbed on Au Electrodes by an Organic Linker: Fermi Level Pinning of the HOMO. *The Journal of Physical Chemistry C* **2009**, *113*, 14200-14206.
- (19) Markus, T. Z.; Itzhakov, S.; Alkotzer, Y. I.; Cahen, D.; Hodes, G.; Oron, D.; Naaman, R. Energetics of CdSe Quantum Dots Adsorbed on TiO₂. *The Journal of Physical Chemistry C* **2011**, *115*, 13236-13241.
- (20) Wang, Y.; Xie, Z.; Gotesman, G.; Wang, L.; Bloom, B. P.; Markus, T. Z.; Oron, D.; Naaman, R.; Waldeck, D. H. Determination of the Electronic Energetics of CdTe Nanoparticle Assemblies on Au Electrodes by Photoemission, Electrochemical, and Photocurrent Studies. *The Journal of Physical Chemistry C* **2012**, *116*, 17464-17472.
- (21) Brown, P. R.; Lunt, R. R.; Zhao, N.; Osedach, T. P.; Wanger, D. D.; Chang, L.-Y.; Bawendi, M. G.; Bulović, V. Improved Current Extraction from ZnO/PbS Quantum Dot Heterojunction Photovoltaics Using a MoO₃ Interfacial Layer. *Nano Letters* **2011**, *11*, 2955-2961.

- (22) Wadia, C.; Alivisatos, A. P.; Kammen, D. M. Materials Availability Expands the Opportunity for Large-Scale Photovoltaics Deployment. *Environmental Science & Technology* **2009**, *43*, 2072-2077.
- (23) Graetzel, M.; Janssen, R. A. J.; Mitzi, D. B.; Sargent, E. H. Materials interface engineering for solution-processed photovoltaics. *Nature* **2012**, *488*, 304-312.
- (24) Ellingson, R. J.; Beard, M. C.; Johnson, J. C.; Yu, P.; Micic, O. I.; Nozik, A. J.; Shabaev, A.; Efros, A. L. Highly Efficient Multiple Exciton Generation in Colloidal PbSe and PbS Quantum Dots. *Nano Letters* **2005**, *5*, 865-871.
- (25) Yang, Y.; Rodríguez-Córdoba, W.; Lian, T. Multiple Exciton Generation and Dissociation in PbS Quantum Dot-Electron Acceptor Complexes. *Nano Letters* **2012**, *12*, 4235-4241.
- (26) Liu, Y.; Gibbs, M.; Puthussery, J.; Gaik, S.; Ihly, R.; Hillhouse, H. W.; Law, M. Dependence of Carrier Mobility on Nanocrystal Size and Ligand Length in PbSe Nanocrystal Solids. *Nano Letters* **2010**, *10*, 1960-1969.
- (27) Wanger, D. D.; Correa, R. E.; Dauler, E. A.; Bawendi, M. G. The Dominant Role of Exciton Quenching in PbS Quantum-Dot-Based Photovoltaic Devices. *Nano Letters* **2013**, *13*, 5907-5912.
- (28) Zhitomirsky, D.; Voznyy, O.; Hoogland, S.; Sargent, E. H. Measuring Charge Carrier Diffusion in Coupled Colloidal Quantum Dot Solids. *ACS Nano* **2013**, *7*, 5282-5290.
- (29) Ip, A. H.; Thon, S. M.; Hoogland, S.; Voznyy, O.; Zhitomirsky, D.; Debnath, R.; Levina, L.; Rollny, L. R.; Carey, G. H.; Fischer, A.; Kemp, K. W.; Kramer, I. J.; Ning, Z.; Labelle, A. J.; Chou, K. W.; Amassian, A.; Sargent, E. H. Hybrid passivated colloidal quantum dot solids. *Nat Nano* **2012**, *7*, 577-582.
- (30) Colbert, A. E.; Wu, W.; Janke, E. M.; Ma, F.; Ginger, D. S. Effects of Ligands on Charge Generation and Recombination in Hybrid Polymer/Quantum Dot Solar Cells. *The Journal of Physical Chemistry C* **2015**, *119*, 24733-24739.
- (31) Lan, X.; Masala, S.; Sargent, E. H. Charge-extraction strategies for colloidal quantum dot photovoltaics. *Nat Mater* **2014**, *13*, 233-240.
- (32) Gao, J.; Perkins, C. L.; Luther, J. M.; Hanna, M. C.; Chen, H.-Y.; Semonin, O. E.; Nozik, A. J.; Ellingson, R. J.; Beard, M. C. n-Type Transition Metal Oxide as a Hole Extraction Layer in PbS Quantum Dot Solar Cells. *Nano Letters* **2011**, *11*, 3263-3266.
- (33) Luther, J. M.; Law, M.; Beard, M. C.; Song, Q.; Reese, M. O.; Ellingson, R. J.; Nozik, A. J. Schottky Solar Cells Based on Colloidal Nanocrystal Films. *Nano Letters* **2008**, *8*, 3488-3492.

- (34) Chuang, C.-H. M.; Maurano, A.; Brandt, R. E.; Hwang, G. W.; Jean, J.; Buonassisi, T.; Bulović, V.; Bawendi, M. G. Open-Circuit Voltage Deficit, Radiative Sub-Bandgap States, and Prospects in Quantum Dot Solar Cells. *Nano Letters* **2015**, *15*, 3286-3294.
- (35) Yoon, W.; Boercker, J. E.; Lumb, M. P.; Placencia, D.; Foos, E. E.; Tischler, J. G. Enhanced Open-Circuit Voltage of PbS Nanocrystal Quantum Dot Solar Cells. *Scientific Reports* **2013**, *3*, 2225.
- (36) Choi, M.-J.; Oh, J.; Yoo, J.-K.; Choi, J.; Sim, D. M.; Jung, Y. S. Tailoring of the PbS/metal interface in colloidal quantum dot solar cells for improvements of performance and air stability. *Energy & Environmental Science* **2014**, *7*, 3052-3060.
- (37) Speirs, M. J.; Balazs, D. M.; Fang, H. H.; Lai, L. H.; Protesescu, L.; Kovalenko, M. V.; Loi, M. A. Origin of the increased open circuit voltage in PbS-CdS core-shell quantum dot solar cells. *Journal of Materials Chemistry A* **2015**, *3*, 1450-1457.
- (38) Zhang, J.; Gao, J.; Miller, E. M.; Luther, J. M.; Beard, M. C. Diffusion-Controlled Synthesis of PbS and PbSe Quantum Dots with in Situ Halide Passivation for Quantum Dot Solar Cells. *ACS Nano* **2014**, *8*, 614-622.
- (39) Moreels, I.; Lambert, K.; Smeets, D.; De Muynck, D.; Nollet, T.; Martins, J. C.; Vanhaecke, F.; Vantomme, A.; Delerue, C.; Allan, G.; Hens, Z. Size-Dependent Optical Properties of Colloidal PbS Quantum Dots. *ACS Nano* **2009**, *3*, 3023-3030.
- (40) Peterson, J. J.; Krauss, T. D. Photobrightening and photodarkening in PbS quantum dots. *Physical Chemistry Chemical Physics* **2006**, *8*, 3851-3856.
- (41) Zhang, J.; Jiang, X. Confinement-Dependent Below-Gap State in PbS Quantum Dot Films Probed by Continuous-Wave Photoinduced Absorption. *The Journal of Physical Chemistry B* **2008**, *112*, 9557-9560.
- (42) Munro, A. M.; Zacher, B.; Graham, A.; Armstrong, N. R. Photoemission Spectroscopy of Tethered CdSe Nanocrystals: Shifts in Ionization Potential and Local Vacuum Level As a Function of Nanocrystal Capping Ligand. *ACS Applied Materials & Interfaces* **2010**, *2*, 863-869.
- (43) Xie, Z.; Markus, T. Z.; Gotesman, G.; Deutsch, Z.; Oron, D.; Naaman, R. How Isolated Are the Electronic States of the Core in Core/Shell Nanoparticles? *ACS Nano* **2011**, *5*, 863-869.
- (44) Carlson, B.; Leschkes, K.; Aydil, E. S.; Zhu, X. Y. Valence Band Alignment at Cadmium Selenide Quantum Dot and Zinc Oxide (10 $\bar{1}$ 0) Interfaces. *The Journal of Physical Chemistry C* **2008**, *112*, 8419-8423.
- (45) Timp, B. A.; Zhu, X. Y. Electronic energy alignment at the PbSe quantum dots/ZnO(10 $\bar{1}$ 0) interface. *Surface Science* **2010**, *604*, 1335-1341.

(46) Gao, J.; Luther, J. M.; Semonin, O. E.; Ellingson, R. J.; Nozik, A. J.; Beard, M. C. Quantum Dot Size Dependent J–V Characteristics in Heterojunction ZnO/PbS Quantum Dot Solar Cells. *Nano Letters* **2011**, *11*, 1002-1008.

6.0 CONCLUDING REMARKS

The study of light matter interaction in nanoscale architectures has revealed new properties and new strategies that can be used to manipulate light for the advancement of science and also for economic growth. This dissertation has dealt with furthering our understanding of these light matter interactions in nanoscale metallic and semiconductor structures with the aim of using them in sensing and photovoltaics applications.

The studies presented in Chapters 2 through 4 address surface plasmon effects that arise in metallic nanostructures when coupled with light, for refractive index sensing applications. In Chapter 2, a novel inplane nanofluidic nanoplasmonics platform was designed and studied for plasmonic sensing and fluid sample delivery concurrently. Preliminary studies through computational simulations and experiments show promise for an integration of plasmonic array structures with microfluidic channel for biodetection. The in-plane nanoslit structure described there will be compatible with emerging lab-on-chip biosensor application.

Chapter 3 shows that the coupling between one dimensional plasmonic nanoparticle chains leads to novel optical features and enhanced refractive index sensing. Studies presented in this Chapter shows experimentally that under longitudinal polarization and at short inter-particle distances the chains exhibited a delocalized surface plasmon mode (DSPR). For a given interparticle distance, it was observed that the wavelength position of the DSPR initially red shifts with increasing number of NPs in the chain and reaches an asymptotic value. The application of the plasmon ruler equation to the square NP dimer gave rise to a longer characteristic decay constant than is reported for spherical or disk shaped NPs. An analytical expression based on a tight binding model was used to obtain a coupling constant for the interparticle coupling strength

from the observed spectral shifts. The coupling constant displayed an $\sim d^{-0.42}$ distance dependence over the range of interparticle distances studied. The sensitivity of the DSPR wavelength for molecular absorbates was found to be larger than that previously reported for LSPR modes of individual NPs and NP dimers; thus the large redshifts in the peak wavelength position of NP chains is a promising sensing strategy that was not explored before our work.

Chapter 4 investigates the coupling of HIV capsid proteins to the plasma membrane using surface plasmon resonance. In this study successful preparation of a model lipid bilayer film was demonstrated and characterized with different methods. Lipid rafts were prepared by allowing sphingomyelin and cholesterol to be titrated into the model lipid bilayer. Specific binding of HIV capsid protein hexamer to the sphingomyelin and cholesterol modified lipid bilayer film was quantified using SPR. The full length capsid protein exhibited no interaction with the bilayer, indicating that the quaternary structure of the capsid proteins might play an important role during its interaction with the lipid rafts. The protein glycerol kinase was used as a negative control to verify any nonspecific interactions.

The studies in Chapter 5 investigate a strategy for enhancing the efficiency of QD based solar cells by eliminating Fermi level pinning in semiconductor quantum dots (QDs) on metal substrates. Fermi level pinning is known to limit the efficiency in Schottky junction solar cells causing the electronic levels of QDs to be 'pinned' with respect to the Fermi level of the metal contacts. Studies performed in this work demonstrate that Fermi level pinning persists in monolayer films of PbS QDs prepared on Au films. Introduction of a thin alumina layer between the PbS QDs and the Au substrate was shown to weaken Fermi level pinning enough that size- and ligand-dependent properties are manifest. These findings point to a procedure for using ligand

tuning of QD energetics to enhance charge injection and separation to overcome the open circuit voltage deficit reported for PbS QD based solar cells.

Altogether, the studies in this thesis provide insight into the controlling optical fields using metallic and semiconductor nanostructures. The presented concepts and insights holds a great promise to new approaches or inspire novel physics that that will eventually bridge the current gap between laboratory discovery and real world application of the metallic and semiconductor nanostructures in fields of sensing and photovoltaics.

APPENDIX A

Supporting Information for Chapter 2

1) Schematic of EBL Fabrication of Square Nanoparticle Chains

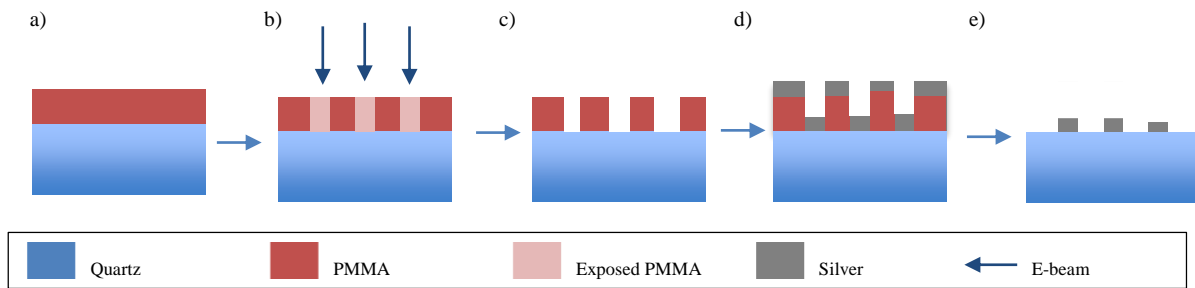


Figure A1. A Schematic representation of the steps used in the electron beam lithography (EBL) process to fabricate square nanoparticle arrays is shown. a) Electron sensitive positive tone polymer (PMMA) is spun onto the cleaned ITO substrate. b) Electron beam exposure of the desired pattern onto PMMA c) Exposed areas being dissolved by developing solvent d) Deposition of the metal thin film (Ag) e) Dissolving the remaining resist to expose the pattern

2) Comparison of the experimental and FDTD calculated transmission spectra Ag square nanoparticle array.

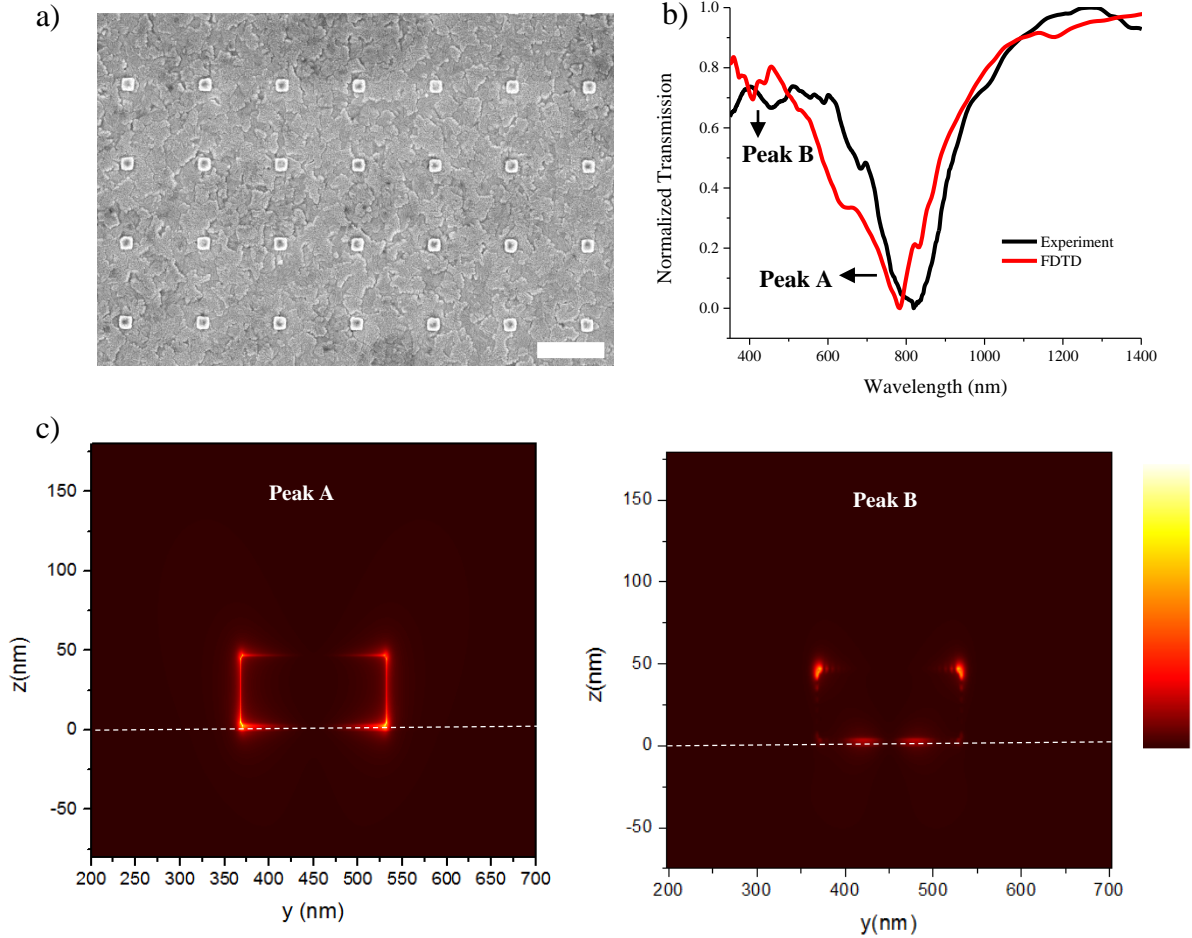


Figure A2. a) SEM image of an array of single square nanoparticles. b) A comparison of the FDTD calculated transmission spectrum of a single NP array with the experimental spectrum. The calculations were done in the manner described in the experimental section of the paper. The main peaks are labeled as peak A and peak B. c) The electric field intensity enhancement ($|E|^2/|E_0|^2$) profiles of the square NP at peak A and peak B wavelengths are shown here by the color coding. Slices given here are collected right yz surface of the nanoparticle whereas light is polarized along the y-direction. The white dashed line indicates the position of the substrate-NP interface. Scale bar ranges from 0-1000, with lighter colors representing higher electric field intensity enhancement.

3) Distance Dependence of the DSPR Evolution

In the following figures, panel (a) shows the evolution of the DSPR peak as the interparticle distance reduces for a square NP tetramer chain. All the spectra are corrected for nanoparticle density. DSPR peak is deconvoluted as described in the main text and the plotted against the energy scale in eV. Area under the DSPR peak is plotted against the interparticle distance in the panel (b).

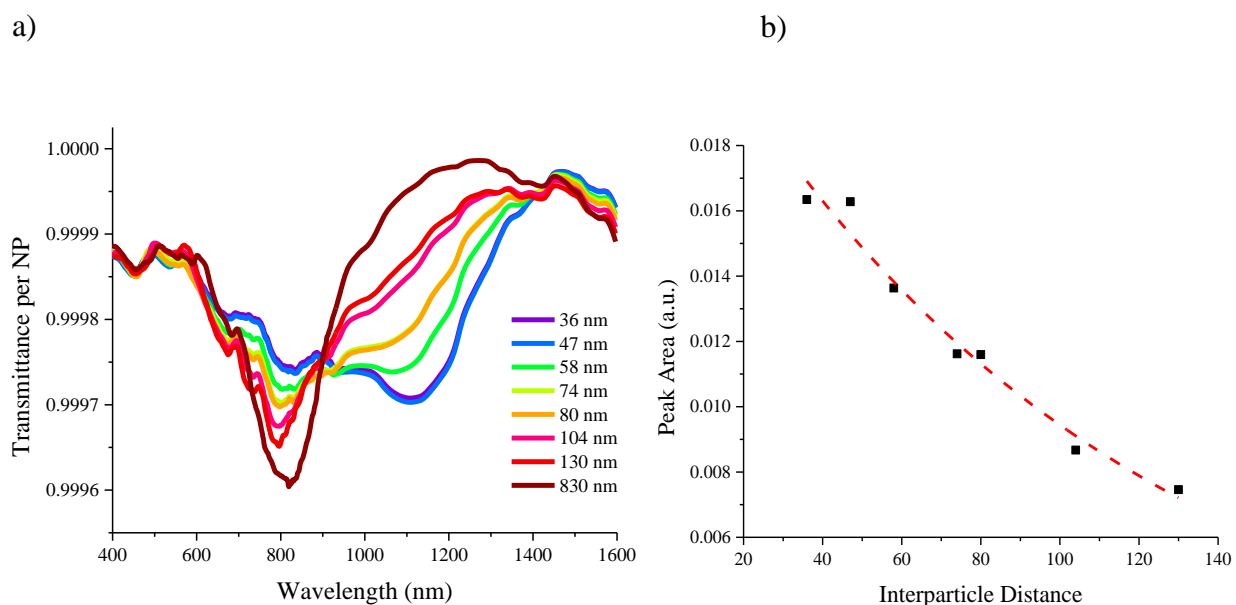


Figure A3. a) The transmission spectra of a square nanoparticle tetramer chain (normalized for NP density) as a function of interparticle separation. b) Change in area under the DSPR peak (normalized per NP) for tetramer chain when the inter-particle distance is reduced. The red dashed line is given as a guide to eye.

4) FDTD calculated electric field intensity enhancement around nanoparticles under transverse polarization.

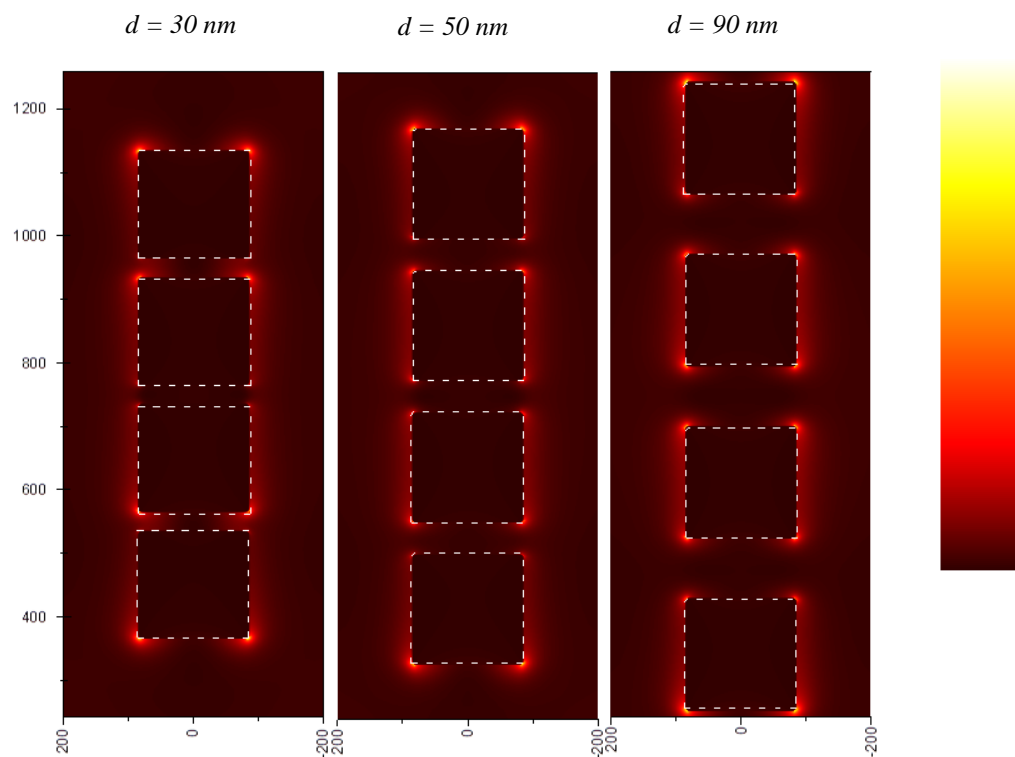


Figure A4. Electric field intensity enhancement profiles for a four NP chain with three different nanoparticle separations (d) when the direction of the light polarization is perpendicular to the major axis of the clusters (transverse polarization). It can be noted that there is no significant electric field intensity enhancement in the gap region when compared with the Figure 5(a), the case where light polarization is along the major axis of the NP chain (longitudinal polarization), indicating much less coupling between NPs under transverse polarization. Scale bar ranges from 0-100, with lighter colors representing higher electric field intensity enhancement.

5) Distance dependence of the coupling constant A of the FDTD calculated transmission spectra of square nanoparticle chains.

The FDTD calculations, as described in the experimental section of the text, were used to obtain transmission spectra of the NP chains under different interparticle distances. The transmission spectra were fitted by a *Breit-Wigner-Fano lineshape*⁷⁰ in order to deconvolute the DSPR peak and extract its wavelength position. Then Equation 1 (main text) was used to obtain the coupling constant A . From the fit in the Figure S5 panel (a), a $A \propto d^{-0.3}$ relationship can be deduced, closer to the power which is obtained from experimental data. The exponential fit in panel (b) again suggest a decay constant ~ 190 nm, closer to what the experimental data suggests.

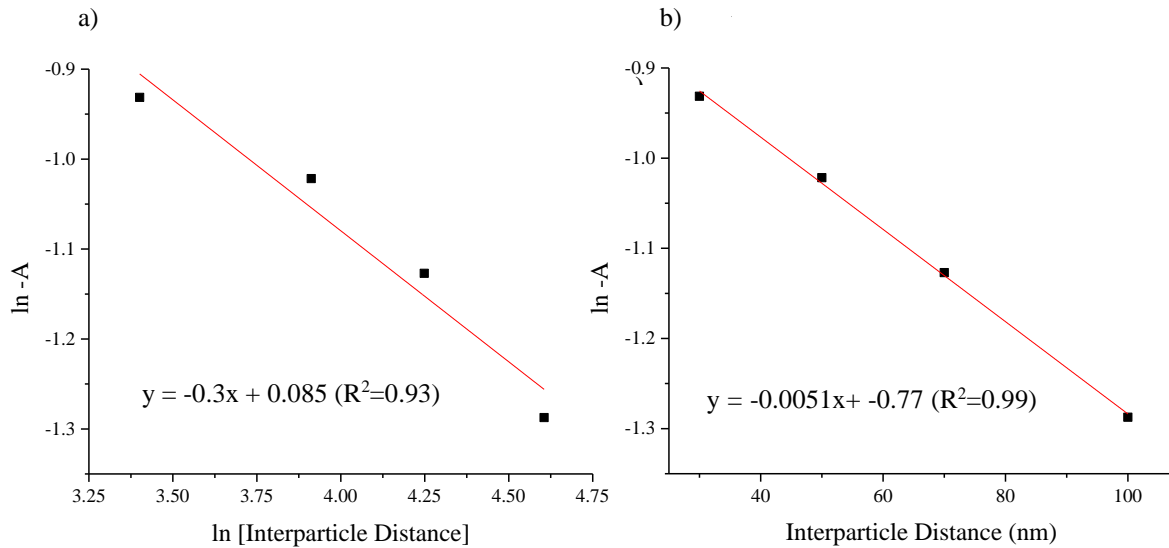


Figure A5. The natural logarithm of the coupling constant ($-A$) is plotted versus the natural logarithm of the interparticle distance, d , between NP in the chain is plotted in panel (a) whereas in panel (b) The exponential distance dependence of the coupling constant is evaluated. The solid red line indicates the best fits in both panels.

6) Ellipsometric thickness of alkanethiol self-assembled monolayers

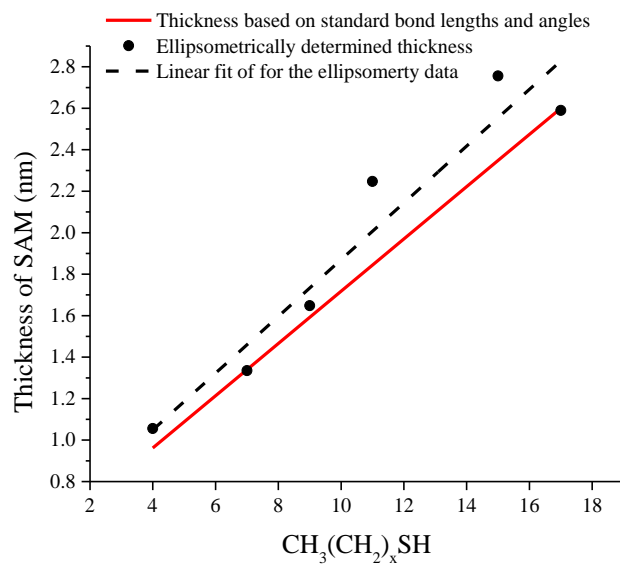


Figure A6. Ellipsometric thickness of self-assembled monolayers of alkanethiols plotted against the number of methylene groups (CH₂) in its alkane chain. Measurements were carried out on a 50 nm silver thin film supported on an ITO substrate. The black dashed line gives the best fit to the obtained data ($y = 0.13x + 0.50$, $R^2 = 0.91$) whereas the solid red line gives the theoretical thickness of each SAM based on standard bond lengths and angles extracted from reference A1.

APPENDIX B

Supporting Information for Chapter 5

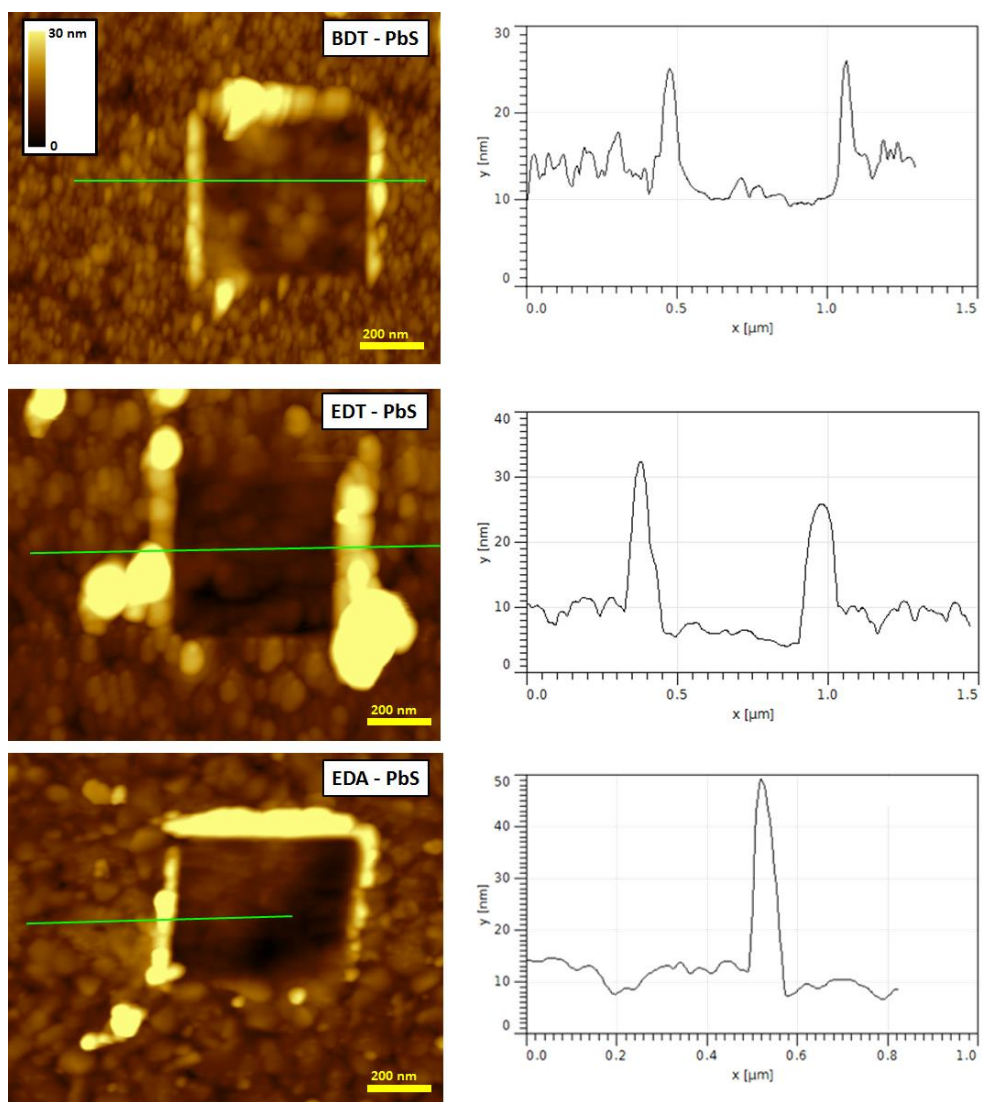


Figure B1. Shows representative AFM images of BDT, EDT, and EDA cross-linked 3.0 nm PbS and their respective thickness profiles. BDT, EDT and EDA had an average thickness of 4.0 nm, 3.9 nm, and 4.24 nm respectively.

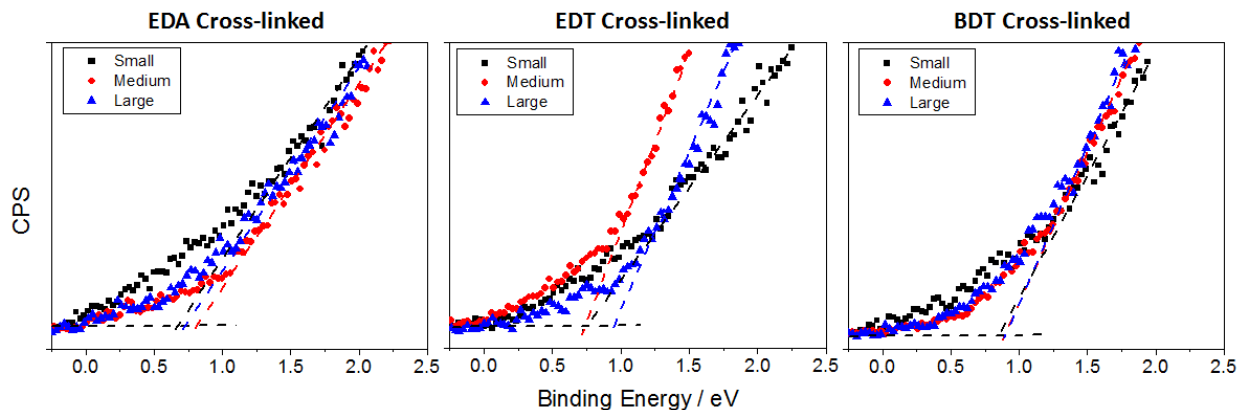


Figure B2. Shows representative UPS spectra for 2.5 nm (black), 3.0 nm (red), and 3.4 nm (blue) PbS QDs cross-linked with EDA (left), EDT (middle), and BDT ligands. The onset energy derived from these spectra, along with those determined from three additional sets of spectra for each ligand and size, were averaged to form the data points in Figure 5.1.

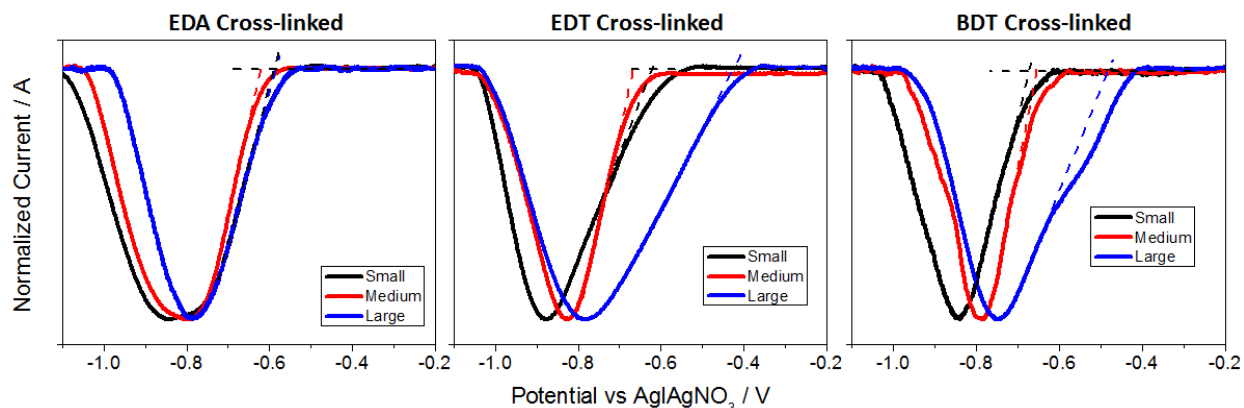


Figure B3. Shows representative background subtracted voltammograms for 2.5 nm (black), 3.0 nm (red), and 3.4 nm (blue) PbS QDs cross-linked with EDA (left), EDT (middle), and BDT ligands. The onset energy derived from these voltammograms, along with those determined from three additional sets of spectra for each ligand and size, were averaged to form the data points in Figure 3.

Table B1. Average electronic state energies in electron volts of the 2.5, 3.0, and 3.4 nm PbS QDs cross-linked with EDA, EDT, and BDT ligands. The CBMs were determined experimentally in the electrochemistry studies and the optical bandgap and exciton binding energy were used to calculate the VBMs. The VBMs were determined experimentally in the UPS studies and the optical band gap and exciton binding energy were used to calculate the CBMs. These values correspond to the data points in Figure 5.3.

Electronic States of PbS NPs of with Different Sizes and Ligands on Au						
Electrochemistry Data						
	EDA VBM	EDA CBM	EDT VBM	EDT CBM	BDT VBM	BDT CBM
2. 5 nm	5.5 1	3.9 5	5.4 5	3.8 9	5.5 1	3.9 7
3. 0 nm	5.2 3	3.9 2	5.3 1	4.0 0	5.2 8	3.9 7
3. 4 nm	5.3 0	4.0 9	5.3 7	4.1 6	5.3 5	4.1 4
Ultraviolet Photoelectron Spectroscopy Data						
	EDA VBM	EDA CBM	EDT VBM	EDT CBM	BDT VBM	BDT CBM
2. 5 nm	5.4 8	3.9 3	5.5 0	3.9 5	5.6 5	4.1 0
3. 0 nm	5.6 7	4.3 6	5.5 7	4.2 6	5.7 0	4.3 9
3. 4 nm	5.5 5	4.3 4	5.6 9	4.4 8	5.7 0	4.4 9

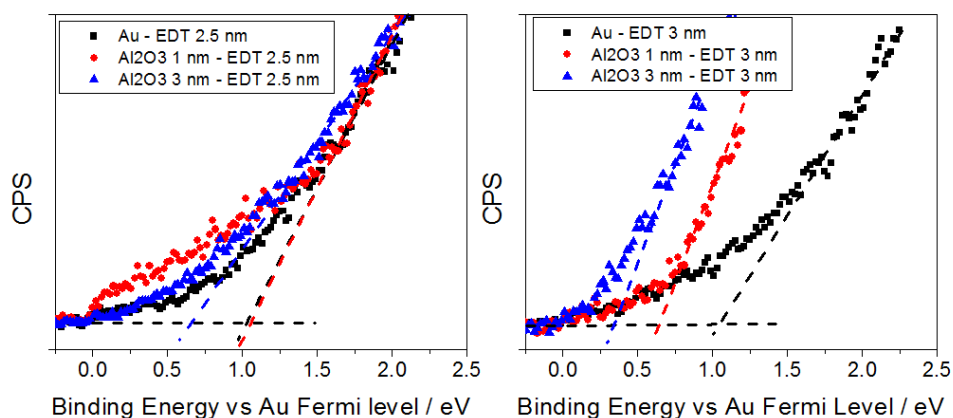


Figure B4. Shows the UPS spectra used for determining the VBM of EDT cross-linked 2.5 nm (left) and 3.0 nm (right) PbS QDs deposited on Au (black), 1.0 nm alumina (red), and 3.0 nm of alumina (blue). The shift in the onset energy as a function of alumina thickness is plotted in Figure 5.4.

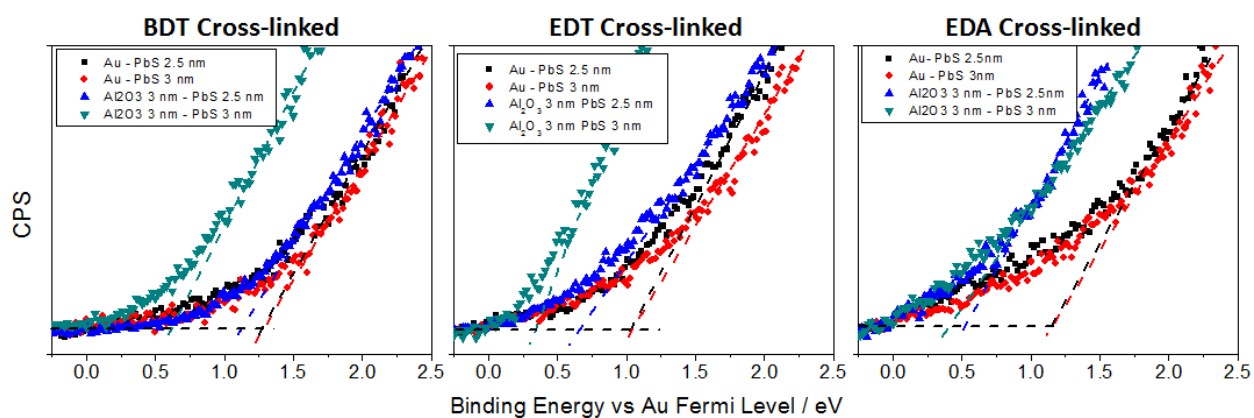


Figure B5. Shows UPS spectra of 2.5 nm (black) and 3.0 nm (red) PbS on Au substrates and 2.5 nm PbS (blue) and 3.0 nm PbS (teal) on 3.0 nm thick alumina substrates. The cross-linkers used in the experiments were BDT (left), EDT (middle), and EDA (right). These data correspond to the data points of Figure 5.5.

Table B2. Average electronic state energies in electron volts of 2.5 and 3.0 nm PbS QDs cross-linked with EDA, EDT, and BDT ligands reported against the Fermi edge of Au. The VBM were determined by UPS and the CBM was found by adding the optical band gap and exciton binding energy. These values correspond to the data points in Figure 5.5.

Comparison of Electronic States of PbS on Au and Alumina						
Measured on Gold						
	EDA VBM	EDA CBM	EDT VBM	EDT CBM	BDT VBM	BDT CBM
2.5 nm	1.21	- 0.46	1.01	- 0.657	1.21	- 0.43
3.0 nm	1.20	- 0.21	1.02	- 0.387	1.27	- 0.14
Measured on 3.0 nm of Alumina						
	EDA VBM	EDA CBM	EDT VBM	EDT CBM	BDT VBM	BDT CBM
2.5 nm	0.52	- 1.15	0.63	- 1.04	1.1	- 0.57
3.0 nm	0.42	- 0.99	0.32	- 1.09	0.55	- 0.86